Technical Report

EXPERIMENTAL AND ANALYTICAL MODELLING FOR PROPELLANT-EMBEDDED ANCHORS

By H.H. Einstein, A.J. Whittle, F. S Jeng and D.E. Legaspi Jr.

MITSG 90-22

MIT Sea Grant College Program

Massachusetts Institute
of Technology
Cambridge, Massachusetts
02139

EXPERIMENTAL AND ANALYTICAL MODELLING FOR PROPELLANT-EMBEDDED ANCHORS

By H.H. Einstein, A.J. Whittle, F. S Jeng and D.E. Legaspi Jr.

MITSG 90-22

Sea Grant College Program
Massachusetts Institute of Technology
Cambridge, Massachusetts 02139

Grant No: NA86AA-D-SG089
Project No: RO-33

EXPERIMENTAL AND ANALYTICAL MODELLING

FOR

PROPELLANT EMBEDDED ANCHORS

by

H. H. Einstein[1]
A. J. Whittle[2]
F. S. Jeng[3]
D. E. Legaspi, Jr.[4]

1 Professor of Civil Engineering, Massachusetts Institute of Technology
2 Assistant Professor of Civil Engineering, Massachusetts Institute of Technology
3 Research Assistant, Department of Civil Engineering, Massachusetts Institute of Technology
4 Research Assistant, Department of Civil Engineering, Massachusetts Institute of Technology

January 31, 1990

Table of Contents

CHAPTER 1
INTRODUCTION

1. Introduction

PEA (Propellant Embedded Anchor) research is aimed at understanding the fundamental behavior during penetration and pullout of a PEA into discontinuous brittle material. Based on this understanding, we intend to create a predictive model for penetration and pullout and to validate it with laboratory experiments thereby updating the model based on the experimental results. The model will then serve as a basis for prototype PEA design, in particular probing information in most primary shape and size. The fundamental character of the MIT PEA research makes it possible to not only provide the basis for PEA models but also for other problems where penetration and pullout have to be considered, notably tension piles in any type of ground and structural fasteners.

The principle of the MIT PEA research is the consideration of penetration and pullout in a unified manner. The penetration of a PEA into a discontinuous mass, as a matter of fact into any ground, changes stress field and material properties in the penetrated medium and at the medium-penetrator interface. The stress field and medium characteristics in turn affect the extraction process, i.e. pullout resistance.

The research conducted at MIT during the years 1987 to 1989 consisted of two smaller efforts in 1987 and 1988 supported solely by the U.S. Department of the Navy; the major effort in 1989 was supported by the MIT Sea Grant College Program with funding from the U.S. Department of the Navy.

1.2 Preceding work

In 1987 the literature on propellant embedded anchors and penetration in general was reviewed. This led to the conclusion that neither a suitable model nor even the basic understanding of penetration into jointed rock existed. The understanding of penetration into ductile material is better but many of the models are unsatisfactory. In 1988 we took a first step at remedying this situation by conducting a series of experiments on jointed rock

models (Propellant Embedded Anchors in Jointed Rock). This test series was continued and completed during the first 5 months of 1989. We achieved our goal and have now a firm understanding of what goes on in deep penetration into and pullout from jointed rock. A paper (Model Experiments for Propellant Embedded Rock Anchors) has been written on this subject and is, at present, being reviewed for publication in Rock Mechanics and Rock Engineering. The mechanisms identified in this research are built into the MIT jointed rock model which will be used for the penetration and pullout mechanism models.

1.3 Major PEA Research

On the basis of the preceding research, we started in 1989 the major research effort which, as stated before, involves model development and experimental validation.

As originally proposed, this effort should continue during 1990 and 1991.

On the basis of the 1987 review of penetration and pullout models, we decided that combining the strain path method with a suitable model of jointed rock will provide us with a sound and practically feasible approach. The strain path method, which was developed for deep penetration into incompressible ductile materials, allows one to determine the two-dimensional strain and stress field on the basis of ground parameters which can be determined by standard tests. This is in contrast to cavity expansion methods which are limited to one dimension on the one hand and advanced numerical methods for which the determination of parameters is very difficult. Nevertheless, it is necessary to expand the strain path method first to compressible ductile materials and to eventually combine it with a suitable model representing rock masses, i.e. brittle discontinua. During the second half of 1989 our main research efforts were directed toward such further development of the strain path method. The two major achievements were the simple penetration prediction model for incompressible, cohesive and frictional ductile materials and the complete stress-strain field

formulation for cohesive and frictional, incompressible ductile materials, as well as initial steps for the compressible formulation.

The simple penetration prediction model, which was validated by comparison with field results from the literature, is important for two reasons. First, it allows one to predict penetration depth into ductile materials based on standard soil properties. In other words, complex modelling and testing with the associated difficulties in prediction is avoided. Second, the fact that a strain path method based penetration prediction model produces satisfactory (i.e., validated) results, indicates that the strain path method provides a reliable approach to rapid penetration modelling!

The complete strain-stress formulation based on the strain path method for penetration into frictional incompressible ductile materials did not exist so far. As indicated above, the stress field is needed for pullout resistance prediction. In addition to being useful for penetration into frictional materials such as sand, the formulation also provides a bound for penetration models for jointed rock.

Both the penetration depth model and the complete strain-stress field model will be extended in the coming year. Most importantly, this will involve combination of the strain path method with the jointed rock model, but it will also include the consideration of other efforts such as the free surface, strain rate and possibly special interface mechanisms.

The initial series of experiments conducted in 1988 and in the first part of 1989 were entirely satisfactory in letting us gain insight into the fundamental mechanisms during penetration into brittle discontinua and thus providing the basis for the extended jointed rock models. They had the disadvantage, however, of having only limited instrumentation. For the proposed validation experiments, it will be necessary to have a very good idea on the stress field in the medium and eventually also at the penetrator-medium interface. Most importantly, it is necessary to know the acceleration-deceleration history of the penetrator. We, therefore, designed and built a new experimental setup for penetration into jointed rock models (and simultaneously for testing penetration into structural

materials). The new setup includes a Hilti fastener gun (donated by Hilti) which we equipped with a new piston and instrumented with an accelerometer. In addition, the medium models were reconfigured such that we can apply and measure confining stresses before and during the penetration-pullout experiments. Initial tests with this equipment were run and showed that it performed satisfactorily.

The 1989 PEA research has thus provided complete understanding of brittle discontinum behavior in penetration and pullout, led to the development of penetration prediction and complete stress field models for all ductile materials and included the development, construction and testing of the major experimental equipment. All this provides not only the basis for the penetration and pullout prediction model for brittle discontinua; since it is fundamental work, the 1989 research also can provide the basis for penetration and pullout in any geological or structural material.

1.4 Report Structure

Chapters 2 and 3 are devoted to experimentation. Chapter 2 contains a description of the final phase of the initial experimentation which we conducted in 1989 as well as the major results of the entire 88/89 experimental series. This is followed by a description of the design of the new test equipment and of the initial experiments conducted with it. Chapters 4 through 6 address modelling. In Chapter 4 we are going to expand on the comments above (Section 1.3) and describe our modelling concept in more detail. This is followed by a description of the major strain path model extension in Chapter 5 and, in Chapter 6, by a description of the penetration prediction model. Concluding comments and an outlook are given in Chapter 7.

CHAPTER 2
TEST SERIES SPRING 1989

2.1 Introduction

From the results of the preceding penetration and pullout tests presented in the report entitled "Propellant Embedded Anchors in Jointed Rock," (Einstein and Jeng, 1988), we concluded that the confining stress greatly influences penetration resistance, fracture phenomena and pullout resistance. In the preceding test series, the confining stress was applied by using aluminum shells and hose clamps which constrained the outward radial movement of the cylindrical specimen during penetration. Specifically, the confining stress was applied with shells and clamps which were installed before the penetration test; as the penetrator penetrated the specimen, the specimen tended to expand outward in the radial direction which produced additional confining stresses as the shell-clamp system resisted the radial expansion. The magnitude of the applied confining stress and the amount of radial expansion during the penetration process were, however, not measured. Given the apparent importance of the confining stress, this lack of exact knowledge was unsatisfactory, and it was decided to run additional tests in which the confining stress was measured.

Specifically, in the current test series, the stresses in the hose clamps were measured to record the confining stresses which existed during the penetration and pullout processes. In addition, we used this test series to study the effect of the composition of the resin mixture. Otherwise, gypsum and resin subjected to rapid and slow penetration were used as before.

Section 2.2 below describes the testing program of the Spring 89 test series, including the types of tests and the general testing schedule. In Sections 2.3 through 2.5, the testing procedures, test results and analyses are reported. Section 2.6 specifically addresses the confining stress issue. Measured circumferential strain (ε_θ) and calculated circumferential stress (σ_θ) are presented as are the estimated normal stresses (σ_n) acting on the shank of the penetrator. In Section 2.7 the results of the Spring 89 test series are compared to

those of the previous test series. General conclusions are drawn in Section 2.8

2.2 Testing Program

The main purpose of the Spring 1989 test series was to measure the confining stress. This was achieved by measuring the circumferential strain of the hose clamps and by calculating the corresponding hoop (circumferential) stress.

Most of the other characteristics of the Spring 89 test series were the same as those in test series 12, 13 and 15 (see Einstein and Jeng, 1988 and Table 2.1) such that the results of different test series can be compared.

The Spring 89 test series consisted of the four test series 17 to 20 (Table 2.1):

1. Test series 17: Slow penetration tests followed by pullout tests, using 5.1 x 10.2 cm cylindrical gypsum specimens (intact specimens only, replicating the conditions of test series 15).
2. Test series 18: Rapid penetration tests followed by pullout tests, using 5.1 x 10.2 cm cylindrical gypsum specimens with varying joint spacings (replicating the conditions of test series 12).
3. Test series 19: Rapid penetration tests followed by pullout tests, using 5.1 x 10.2 cm cylindrical resin specimens (with the ratio of curing agent:resin of 1/20 by weight) with varying joint spacings (replicating the conditions in test series 13).
4. Test series 20: Rapid penetration tests followed by pullout tests, using 5.1 x 10.2 cm cylindrical resin specimens (with the ratio of curing agent:resin of 1/10 by weight) with varying joint spacings (similar testing conditions as those in test series 19 except for the increased amount of curing agent).

The resin mixtures in test series 19 and 20 were different in order to study the effect of the mixture on fracture phenomena and mechanical properties. The curing agent was Ancamine K-61-B.

The testing conditions common to test series 17 through 20 were as follows:

1. Penetrator Type B (diameter 3.7 mm, sharp tip; see Fig. 2.1)
2. All the specimens were tested under confined conditions. The confinement was provided as in test series 12, 13 and 15 (see Fig. 2.2a). However, a strain gage was attached to each hose clamp to measure its deformation.
3. All the specimens were normal size (cylinders with a diameter of 5.1 cm and a height of 10.2 cm).
4. The orientation of jointing was 0 degree (horizontal joints) and the joints were plain (joint surfaces in direct contact with each other).
5. Number of specimens: 6 gypsum specimens and 3 resin specimens per series.

Some additional investigations on the basic properties of gypsum were also performed. By using a π-tape, the diameter of the cylinder specimen can be accurately measured. (The π-tape can measure the diameter at a precision of 0.01 mm.) The diameters of gypsum specimens after casting and after curing were measured (see Table 2.2). The data indicate that the diameter of the gypsum specimens did not change during curing, i.e., the specimens did not shrink.

The basic properties of the gypsum specimens are as follows:

diameter = 5.1 cm
height = 10.2 cm
weight before curing $\cong$ 360 g
weight after curing $\cong$ 300 g
density before curing = 1.74 g/cm^3
density after curing = 1.46 g/cm^3
void ratio (e) = 0.58

2.3 Slow Penetration Tests on Gypsum (Test Series 17)

2.3.1 Testing Procedure

The penetrator was placed on the top of the specimen vertically beneath the loading frame of a feedback-controlled loading machine which pressed it into the specimen at a penetration rate of 0.5 mm per minute. A penetration force vs. penetration depth curve was recorded for each specimen. The final penetration depth was 20 mm if the penetration force did not exceed the capacity of the loading machine (5 KN). If the penetration force reached the loading capacity of the machine, the slow penetration test was terminated immediately.

Following the slow penetration test, the loading frame was moved in the opposite direction to conduct the pullout test. A pullout force vs. pullout displacement curve was also recorded. The pullout test was terminated when the pullout force fell below 20 % of the peak value.

2.3.2 Test Results

The results of the slow penetration tests include:

1. Slow penetration force vs. penetration displacement curves.
2. The pullout force vs. pullout displacement curves.
3. A record of the fracture phenomena (i.e. the type of fracturing such as radial cracking, chipping and crushing), of crack depth, of penetration depth, and of other information (such as the circumferential strains at different stages, fractography and testing conditions).

The detailed data are kept at MIT.

A typical penetration force vs. penetration depth curve is shown in Fig. 2.3. The curve has the following characteristics: It starts with an almost linear section (OA) and breaks at point A. The force drops (section AB), but increases again as the penetration depth increases. The slope in section CD is practically constant but smaller than the slope in section OA. There are several small breaks within section CD. The slow penetration test is terminated at point D.

No radial cracks could be observed before the drop of the curve (marked by A in Fig. 2.3), but right after this sudden drop (usually accompanied by a breaking sound), several cracks appeared. This indicates that the radial cracks initiate at A. The penetration depth where the radial cracks initiate is 6.3 mm ± 1.3 mm. The penetration force at the first crack initiation is 3.05 ± 0.90 KN. The following small breaks within section CD of the curve may indicate that the cracks propagate further.

In Figure 2.3, the area enclosed by OABCDE represents the energy imparted to the system (specimen + clamps), which is:

Specimen #	Energy (Joule)
SG01	42.5
SG02	54.2
SG03	53.1
SG04	63.5
SG05	57.7
SG06	52.9

Mean Imparted Energy = 54.0 ± 6.9 Joule

Presumably, to achieve the same penetration depth, the energy imparted in rapid penetration tests should be equal or larger than that in slow penetration tests, i.e., the slow penetration tests represent a lower bound of the energy required in rapid penetration tests. The mean energy in slow penetration tests is 54.0 joules. We can thus calculate the minimum impact velocity required in rapid penetration tests:

1. Energy required in slow penetration: 54 joules
2. The mass of the penetrator is 5.1 grams and the mass of the piston is 207.4 grams.
3. To achieve the same penetration depth, the kinetic energy required in rapid penetration tests has to be ≥ 54 joules.
4. Assuming $E = 1/2\ mv^2$, and assuming that the mass, m, is the mass of penetrator only (5 grams), the minimum impact velocity is 145.5 m/s. If the piston is attached to the penetrator during the penetrator processes, its mass should be considered also. This

results in the minimum impact velocity of 22.5 m/s. We measured the initial velocity of the penetrator by shooting it across 5 electrical wires spaced at 3.2mm and recording the time intervals at which the wires were broken. The test results show that the initial velocity of the penetrator was greater or equal to 18 m/s. This result corresponds well to the lower bound obtained from the slow penetration tests.

The penetration force can be used to express penetration resistance by dividing it by the embedded area (see Fig. 2.4 for details on the calculation of the embedded area). A typical penetration resistance-displacement curve is shown in Fig. 2.5. It has the following characteristics: It starts with a steep slope, S_1, and breaks at point A, which corresponds to point A in Fig. 2.3 and to the first occurrence of radial cracks. The resistance drops (AC) and then increases again as the penetration depth increases. The curve has a flatter slope, S_2, after point D, with decreasing inclination as penetration increases.

In the slow penetration tests, two to four radial cracks were observed in all of the specimens. The number of radial cracks produced in these tests is smaller than the number (3 to 7) produced in rapid penetration tests as will be shown in Section 2.4. The mean crack depth is 8.9 cm, which is greater than the mean crack depth (7.4 cm) in the rapid penetration tests. A chipped zone and a crushed zone (see Fig. 3.6 of the 1988 PEA report by Einstein and Jeng) were observed in each specimen. The detailed fracture phenomena of each specimen are described in Table 2.3, which also includes the observations on crack depth and penetration depth.

The results of the pullout tests following slow penetration will be discussed in conjunction with the other pullout tests (Section 2.5).

2.4 Rapid Penetration Tests (Test Series 18, 19 and 20)

2.4.1 Testing Procedure

The specimens were confined as shown in Fig. 2.2a and the tests were conducted as in the preceding test series (see Einstein and

Jeng, 1988). After each penetration test, the specimen was fixed by a holding frame (see Fig. 2.6) and the pullout test was performed.

2.4.2 Test Results

The results of the rapid penetration tests are:

1. The pullout force vs. displacement curve for each specimen.
2. A record of the fracture phenomena (i.e. the type of fracturing such as radial cracking, chipping and crushing), of crack depth, of penetration depth, and of other information (such as the circumferential strains at different stages, fractography and testing conditions).

The fracture phenomena observed for all gypsum specimens are radial cracking, crushing and chipping. The number of radial cracks ranges from 3 to 7. The penetration depth ranges from 2.1 cm to 2.4 cm. The crack depths (mean value) are 7.4 cm, 4.0 cm, 2.0 cm, 2.8 cm and 2.9 cm for the intact specimen and for specimens with joint spacings of 4 cm, 2 cm, 1 cm and 0.5 cm, respectively. The intact specimen has thus the greatest crack depth and the crack depth decreases to about the magnitude of the penetration depth as the joint spacing decreases.

The resin specimens show a crushed zone (all specimens), radial cracks (20 out of 30) and a chipped zone (only 2 out of 30 specimens). Many resin specimens (10 out of 30) did thus not have radial cracks after penetration but only the hole produced by the penetrator. The mean penetration depth was 1.76 ± 0.29 cm for the cracked specimens and 1.26 ± 0.34 cm for non-cracked specimens. This indicates that the penetration depth is smaller if there are no radial cracks.

The detailed phenomena including crack depth and penetration depth observed in each specimen are listed in Table 2.3. The fracture phenomena in resin will be further discussed in Section 2.7 when comparing them to those in the previous test series.

The results of the pullout tests which follow the rapid penetration tests will be discussed in Section 2.5.

2.5 Pullout Tests (Test Series 17 to 20)

2.5.1 Testing Procedures

The test setup is shown in Fig. 2.6. The penetrator was extracted at a rate of 0.5 mm/sec and a pullout force versus displacement curve was recorded for each test. The detailed procedures are described in Einstein and Jeng (1988).

2.5.2 Test Results

A typical pullout force vs. pullout displacement curve for tests on gypsum specimens is shown in Fig. 2.7. It has the following characteristics:

1. The curve starts with a sharp approximately linear rise (OA) and reaches peak at point A.
2. The pullout force drops sharply after the peak (AB).
3. Following the drop is a stick-slip section (BCD).
4. A segment without stick-slip follows (DE).
5. The pullout test is terminated at point E.

For resin, the typical pullout force vs. displacement curve is like that shown in Fig. 2.8. There are no stick-slip phenomena nor is there any sharp drop of force right after the peak, i.e. the behavior is generally more ductile.

An interesting observation is that the pullout force practically disappears at displacements of 6 to 10 mm (for gypsum), although the penetration depth is about 20 mm.

The pullout force-displacement curve can be expressed as a pullout resistance-displacement curve such as that shown in Fig. 2.9 for gypsum by dividing the force by the embedded shank area, A_1 (see Fig. 2.4). The tip area A_2 is not considered in computing the resistance; however the area A_1 is reduced as a function of displacement. The curve has a peak at point A (which corresponds to the the point A in Fig. 2.7) followed by a sharp drop of resistance (segment AB). The pullout resistance decreases slowly in a nearly linear segment BC. The pullout resistance vanishes at a displacement of about 9 mm, in the case shown in Fig. 2.9.

The pullout resistance-displacement curve allows one to get an indication on the penetrator interface shearing resistance due to friction. One can reasonably assume that the drop AB represents breaking of cohesive (tensile) bonds at the tip (area A_2 in Fig. 2.4) and along the shank (area A_1 in Fig. 2.4). Segment BC represents thus frictional interface resistance only. This is supported by the fact that this segment is horizontal or nearly horizontal (recall that the reduction of area A_1, as the penetrator is pulled out, is considered in computing the pullout resistance). The pullout resistance represented by the "plateau" BC, which is approximately 8 MPa in Fig. 2.9, is thus the frictional interface resistance during pullout.

The maximum (peak) pullout resistances in test series 17 to 20 are listed in Table 2.4. It will be noted that the maximum pullout resistance in slow penetration tests is 50% lower than that in rapid penetration tests. The change of the maximum pullout resistance with joint spacing is shown in Fig. 2.10. For gypsum specimens, the maximum pullout resistance decreases slightly as the joint spacing decreases. Resin test series 20 shows a similar trend, while test series 19 does only do so for spacings of 2 cm and less.

2.6 Measurement of Circumferential Strain at the Boundary

2.6.1 Testing Procedures

Recall that six aluminum shells, cut from an aluminum pipe, were tightened by four hose clamps as shown in Fig. 2.2a to provide the confinement. Three clamps (clamp #1, 2 and 3) were installed around the upper part of the specimen and one clamp was installed at the bottom of the specimen. A strain gage, attached to each clamp was used to measure the circumferential strain (ε_θ). The configuration for reading the circumferential strain is shown in Fig. 2.11. The readout device consisted of a 1/2 Wheatstone bridge (with a dummy strain gage to compensate for temperature effects), a switch box, a power supply and a voltmeter.

The procedure for measuring circumferential strains (ε_θ) at the boundary was as follows:

1. The "shell-clamp" confinement device was installed.
2. Three readings were taken during the test at the following stages: before penetration, after penetration and after pullout of the penetrator.
3. The circumferential stress (σ_θ) applied at the boundary was obtained by assuming that a) the thickness of the clamp was very small and b) there is no yielding anywhere within the clamp such that the elastic relation $\sigma_\theta = E\,\varepsilon_\theta$ is applicable (where E is the Young's modulus of clamp). The clamp is made of stainless steel (AISI # 301) with an E value 28 x 10^6 psi (2 x 10^5 MPa). An example calculation is given in Appendix A. To check the validity of assumption (b), the limiting stress/strain to cause yielding in the clamp has been evaluated in Appendix B. The dimension of the stainless hose clamps used in these tests is also shown in Appendix B. The calculation indicates that yielding could occur at the narrow cross sectional area of the clamp if the circumferential strain is greater than 0.11% or if the circumferential stress is greater than 220 MPa. The observed strain does not exceed these limiting values and assumption (b) is thus applicable.

One has to be aware of the fact that the confining stress application and measurement may be subject to some, albeit small, errors. We assume that only axial stresses (pure tension) exists in the hose clamps (Fig. 2.2b) and that, therefore, a single strain gage at the outer surface provides sufficient information to determine the stresses in the clamp. The assumption of pure tension will be incorrect if bending occurs (Compensating for bending by placing strain gages on the interior surface of the hose clamp is not also possible, because the strain gages would produce an uneven contact between the clamp and the aluminum shells). Such bending occurs if the radius of the specimen is different from the radius of the hose clamp which is usually the case. However, the bending strain is relatively small compared to the axial strain.

2.6.2 Test Results (Test Series 17 to 20)

The ε_θ measured after the penetration test and the calculated σ_θ for each specimen are listed in Table 2.5. The changes (from the initial state) of the σ_θ values in test series 17 to 20 are summarized below:

Clamp #	After Penetration (MPa)	After Pullout (MPa)
1	100 to 200	50 to 100
2	50 to 150	50 to 80
3	-50 to +30	-50 to +30
4	-20 to +20	-10 to + 10

These results allow one to draw following conclusions:

1. The measured stresses decrease from the top clamp to the bottom clamp.
2. The negative sign indicates that the circumferential stress decreases (compared to the initial state) after the penetration test. The decrease in confining stress from the initial state implies that there is a confining stress when the clamps are installed.
3. After the pullout test the stress (strain) does not return to zero, which indicates that the stress at the outer boundary is not released. Some of the strains and stresses produced by the penetrator in the specimen remain thus locked in.

The measured circumferential stresses can also be used to obtain a rough idea about the normal stress acting on the shank of the penetrator. The following assumptions were made for this purpose:

1. All the radial cracks extend to the boundary, and they are planes perpendicular to the top surface of the specimen.
2. The stresses acting in the plane perpendicular to the penetrator axis are σ_θ at the boundary (applied by the clamp) and σ_n at the shank interface as shown in Fig. 2.12.

According to these simplified assumptions, the relationship between σ_n on the shank and the measured σ_θ at the boundary is solved from the equilibrium of forces acting on the specimen (see Fig. 2.12). This yields the following relation:

$$\sigma_n|_{shank} = 0.314\sigma_\theta|_{clamp}$$

As described in Section 2.5, the frictional shearing resistance τ on the shank can be estimated from the pullout resistance-displacement curve. The τ values for each gypsum specimen are listed in Table 2.5 (column τ). The measured ε_θ and calculated σ_θ and σ_n are also listed in Table 2.5.

The shearing resistance due to friction (τ) and the normal stress (σ_n) are plotted in Fig. 2.13, which should allow us to determine a friction coefficient for the penetrator interface from $\tau=\mu\sigma_n$. As shown in Fig. 2.13, the data points are so scattered that no single relationship for all the points can be obtained. Also, most of the data vary within the range of μ= 0.06 to μ= 0.3. These μ are low (the friction angle of gypsum is about 33°, i.e., μ is about 0.65). It will also be noted that for a given specimen configuration (intact or specific joint spacing), the shearing resistance τ is, in most cases, independent of the normal stress.

The resin specimens are not considered in this discussion because 1) during the rapid penetration test on resin specimens, the hose clamp was not strong enough to constrain the resin specimens and an additional C-clamp had to be added to increase the confinement; therefore, the stresses (measured with the strain gages in the clamps) do not represent the stresses during the penetration process 2) the analysis is only valid for specimens with radial cracks.

2.7 Comparison with Previous Test Results

2.7.1 Comparison of Fracture Phenomena

For gypsum, the fracture phenomena (which include radial cracking, crushing and chipping) of test series 12 and 18 are similar (see Fig. 2.14).

For resin, the fracture phenomena of test series 13, 19 and 20 differed. It was observed that (see Fig. 2.15):

1. 13 out of 15 resin specimens (with curing agent to resin ratio = 1/20) were fractured in test series 19.
2. 5 out of 10 resin specimens (with curing agent to resin ratio = 1/20) were fractured in test series 13.
3. 6 out of 15 resin specimens (with curing agent to resin ratio = 1/10) were fractured in test series 20.

The resin in test series 13 and 19 was the same mixture and was tested under the same testing conditions; however, as shown above and in Fig. 15, the fracture phenomena differed.

2.7.2 Comparison of Penetration Depth and Crack Depth

A summary of the penetration depths and crack depths in test series 18, 19 and 20 is given in Table 2.6 while a summary of the penetration depths and crack depths of the previous test series (series 12 and 13) is given in Table 2.7

Again, the penetration depth and crack depth for test series 12 and 18 (i.e. for gypsum) are similar. The respective depths for test series 13 and 19 (resin) also compare reasonably well while the different curing agent ratio in series 20 evidently causes cracks which are not as deep.

2.7.3 Comparison of Pullout Resistance

The pullout resistance is a function of material properties, fracture phenomena, joint spacing and the other factors. The gypsum specimens in test series 12 and 18 were tested under the same conditions and have similar fracture phenomena. This is consistent with the similar pullout resistances in these two test series (the pullout resistance of test series 18 is somewhat higher than that of test series 12). The pullout resistance, in most cases, decreases slightly as the joint spacing decreases. For resin, the pullout resistance differs from one test series to another, even for the two test series with the same resin mixture (test series 13 and 19).

2.8 Conclusions

From the results in the Spring 89 series, one can draw following conclusions:

1 Confining stress:
The change of confining stress can be measured. This provided us with useful information in estimating the normal stress acting on the shank during the penetration/pullout tests. Also, we found that stresses remain locked into the medium after the pullout test.

2 Fracture Phenomena:
a) The fracture phenomena of all gypsum specimens consist of radial cracking, crushing and chipping.
b) A crushed zone was observed in all resin specimens. Not all of the resin specimens have radial cracks. Those specimens with a lower curing agent ratio (test series 19) have a higher tendency to have radial cracks than the specimens with a higher curing ratio. Only 7% of resin specimens have a chipped zone.

3 Penetration resistance (slow penetration):
a) The penetration resistance drops when the radial cracks initiate.
b) The increment of penetration resistance (force divided by the embedded area) decreases as the penetration depth increases.

4 Pullout resistance:
The pullout resistance in slow penetration is 50% lower than that in rapid penetration. For gypsum, the pullout resistance decreases slightly as the joint spacing decreases. Resin test series 20 shows a similar trend, while test series 19 only does so for spacings of 2 cm or less.

5 Stresses acting on the shank of the penetrator:
The order of magnitude of the normal stresses acting on the shank of the penetrator is about 45 Mpa. The mean frictional shearing resistance of the shank during pullout is 6.7 MPa. The mean friction angle ϕ is thus about 8.5° which is low compared to the friction angle of gypsum (about 33°).

6. When comparing the Spring 89 tests to the corresponding previous test series one notes that the gypsum tests produce similar results in all respects (fracture penomena, crack depth, penetration depth and pullout resistance). For resin, there is some deviation even if the same resin mixtures are compared (notably concerning pullout resistance) while other results are similar. Lowering the curing agent ratio causes significant differences (greater number of cracked specimens and deeper penetration depth).

Test	Material	Specimen Shape	Size (cm)	Joint Spacing(cm)	Joint Orien-tation	Joint Condi-tion	Con-strain-ment	Pene-trator Shape**	Purpose
12 13	gypsum resin*	cylinder	5.1x10.2	0.5, 1,2,4 intact	0°	plain+	yes	B/C	To study pullout resistance as a function of joint spacing, type of material and specimen size (Rapid penetration and Pullout test)
14	gypsum		10.2x20.4	0.5, 1,2,4 intact	-	plain	yes	B	
15	gypsum/ resin*	cylinder	5.1x10.2	intact	-	-	yes	B	Slow penetration test to study effect of strain rate
17	gypsum	cylinder	5.1x10.2	intact	-	-	yes	B	Slow penetration test
18	gypsum	cylinder	5.1x10.2	0.5, 1,2,4 intact	0°	plain	yes	B	Rapid penetration and pullout test
19	resin*	cylinder	5.1x10.2	0.5, 1,2,4 intact	0°	plain	yes	B	Rapid penetration and pullout test
20	resin***	cylinder	5.1x10.2	0.5, 1,2,4 intact	0°	plain	yes	B	Rapid penetration and pullout test

* Resin with curing agent ratio = 1/20
\+ "plain" means that joint surfaces are in direct contact with each other.
** Definitions of penetrator shape are the same as those in Fig. 2.1
*** Resin with curing agent ratio = 1/10
Test Series 17, 18, 19 and 20 are current test series

Table 2.1 Testing Programs for Test Series 12, 13, 15, 17, 18, 19 and 20

Sample #	$(Diameter)_1$* (mm)	$(Mass)_1$* (g)	$(Diameter)_2$** (mm)	$(Mass)_2$** (g)	Δd (%)
1	51.45	362	51.45	302	0
2	51.35	358	51.33	302	-0.04
3	51.39	359	51.33	300	-0.12
4	51.22	357	51.23	298	0.02
5	51.30	360	51.30	301	0
6	51.23	357	51.23	301	0
7	51.30	357	51.30	301	0
8	51.26	356	51.27	301	0.02
9	51.43	358	51.40	302	-0.06
10	51.37	356	51.35	301	-0.04
11	51.30	360	51.30	301	0
12	51.25	360	51.25	301	0

Diameter=$(d_{top}+d_{bottom})/2$

*Stage 1 : before curing
**Stage 2 : after 88 hours curing
Mean Diameter= 51.31 ± 0.06 mm
Mean $(Mass)_1 \cong 360$ g
Mean $(Mass)_2 \cong 300$ g
$(Density)_1 = 1.74$ g/cm^3
$(Density)_2 = 1.46$ g/cm^3

Table 2.2 Basic Data of Gypsum Specimens

Specimen #	Material	Joint Spacing(cm)	Fastener Shape	Crack Number	Crack Depth (cm)	Penetration Depth (cm)	Crushing	Chipping	Test Series
SG01	gypsum	intact	B	3	8.3	1.4	yes	yes	
SG02	"	"	"	3	9.1	1.9	"	"	
SG03	"	"	"	3	9.6	2.0	"	"	
SG04	"	"	"	2 (or 4)	9.2	2.0	"	"	17
SG05	"	"	"	2	9.4	2.0	"	"	
SG06	"	"	"	2	8.0	2.0	"	"	
RG01	"	"	"	4	7.3	2.2	"	"	
RG02	"	"	"	4	9.1	2.3	"	"	
RG03	"	"	"	4	8.3	2.4	"	"	
RG04	"	"	"	4	6.6	2.1	"	"	
RG05	"	"	"	3	6.3	2.1	"	"	
RG06	"	"	"	4 (or5)	6.8	2.2	"	"	
RG41	"	4.0	"	4	4.0	2.2	"	"	
RG42	"	"	"	5	4.0	2.2	"	"	
RG43	"	"	"	4 or more	4.0	2.1	"	"	
RG44	"	"	"	4	4.0	2.2	"	"	
RG45	"	"	"	5	4.0	2.2	"	"	
RG45	"	"	"	6	4.0	2.2	"	"	
RG21	"	2.0	"	5 or more	2.0	2.2	"	"	
RG22	"	"	"	4 or more	2.0	2.2	"	"	
RG23	"	"	"	4	2.0	2.1	"	"	18
RG24	"	"	"	4	2.0	2.2	"	"	
RG25	"	"	"	4	2.0	2.2	"	"	
RG26	"	"	"	4	2.0	2.2	"	"	
RG11	"	1.0	"	3	3.0	2.2	"	"	
RG12	"	"	"	3	3.0	2.2	"	"	
RG13	"	"	"	4	3.0	2.2	"	"	
RG14	"	"	"	4	3.0	2.2	"	"	
RG15	"	"	"	4	2.0	2.2	"	"	
RG16	"	"	"	5	3.0	2.2	"	"	
RG51	"	0.5	"	5	2.8	2.2	"	"	
RG52	"	"	"	4	2.3	2.2	"	"	
RG53	"	"	"	6	4.0	2.2	"	"	
RG54	"	"	"	6	2.8	2.2	"	"	
RG55	"	"	"	7	2.8	2.2	"	"	
RG56	"	"	"	5	2.8	2.2	"	"	
RRL01	resin(L)*	intact	"	2	6.7	2.2	"	"	
RRL02	"	"	"	2	4.8	2.1	"	"	
RRL03	"	"	"	3	4.8	2.2	"	"	
RRL41	"	4.0	"	2	4.0	2.0	"	no	
RRL42	"	"	"	2	4.0	1.9	"	yes	
RRL43	"	"	"	2	4.0	2.0	"	no	
RRL21	"	2.0	"	2	2.0	2.0	"	yes	
RRL22	"	"	"	no	-	1.2	"	no	19
RRL23	"	"	"	3	2.0	1.9	"	"	
RRL11	"	1.0	"	2	1.0	1.7	"	"	
RRL12	"	"	"	3 or more	1.0	1.3	"	"	
RRL13	"	"	"	3	1.0	1.7	"	"	
RRL51	"	0.5	"	2	1.0	1.6	"	"	
RRL52	"	"	"	2	1.0	1.6	"	"	
RRL53	"	"	"	no	-	0.5	"	"	
RRH01	resin (H)**	intact	"	"	-	1.3	"	"	
RRH02	"	"	"	"	-	1.3	"	"	
RRH03	"	"	"	"	-	1.2	"	"	
RRH41	"	4.0	"	"	-	1.9	"	"	
RRH42	"	"	"	"	-	1.3	"	"	
RRH43	"	"	"	2	4.0	1.2	"	"	
RRH21	"	2	"	no	-	1.2	"	"	20
RRH22	"	"	"	"	-	1.2	"	"	
RRH23	"	"	"	2	2.0	2.0	"	"	
RRH11	"	1.0	"	no	-	1.5	"	"	
RRH12	"	"	"	5	1.0	1.5	"	"	
RRH13	"	"	"	6	1.0	1.5	"	"	
RRH51	"	0.5	"	2	0.5	1.6	"	"	
RRH52	"	"	"	1	0.5	1.6	"	"	
RRH53	"	"	"	5	0.5	1.6	"	"	

*L indicates ratio curing agent/resin = 1/20
**H indicates ratio curing agent/resin = 1/10

Note: The definitions of "crushing" and "chipping" are given in Einstein and Jeng, 1988

Table 2.3 Summary of Fracture Phenomena, Test Series 17 to 20

Specimen No.	Peak Pullout Force (KN)	Mean Pullout Force (KN)	Penetration Depth (cm)	Peak Pullout Resistance (MPa)	MeanPullout Resistance (MPa)	Test Series
SG01	0.918		1.4	-*		
SG02	1.081		1.9	7.15		
SG03	1.136	1.065±0.076	2.0	6.98	6.82±0.24	17
SG04	1.093	(7.1%)	2.0	6.72	(3.5%)	
SG05	1.064		2.0	6.54		
SG06	1.095		2.0	6.73		
RG01	1.653		2.2	8.89		
RG02	2.472		2.3	12.51		
RG03	2.262	2.154±0.673	2.1	12.97	12.52±2.78	
RG04	2.957	(31.2%)	2.1	16.96	(22.2%)	
RG05	1.806		2.1	10.36		
RG06	2.495		2.2	13.42		
RG41	2.113		2.2	11.36		
RG42	2.201		2.2	11.83		
RG43	2.701	2.173±0.298	2.1	15.49	11.85±1.96	
RG44	2.238	(13.7%)	2.2	12.03	(16.5%)	
RG45	1.910		2.2	10.27		
RG46	1.877		2.2	10.09		
RG21	2.187		2.2	11.76		
RG22	2.435		2.2	13.09		
RG23	2.251	2.399±0.197	2.1	12.91	13.04±0.98	18
RG24	2.291	(8.2%)	2.2	12.32	(7.5%)	
RG25	2.518		2.2	13.54		
RG26	2.714		2.2	14.59		
RG11	2.129		2.2	11.45		
RG12	1.545		2.2	8.31		
RG13	1.440	1.083±0.298	2.2	7.74	9.70±1.60	
RG14	2.036	(27.5%)	2.2	10.95	(16.5%)	
RG15	2.038		2.2	10.96		
RG16	1.630		2.2	8.76		
RG51	1.542		2.2	8.29		
RG52	1.741		2.2	9.36		
RG53	1.834	1.663±0.166	2.2	9.86	8.94±0.90	
RG54	1.395	(10.0%)	2.2	7.50	(10.1%)	
RG55	1.671		2.2	8.99		
RG56	1.793		2.2	9.64		
RRL01	1.449		2.2	6.02		
RRL02	0.467	1.147±0.590	2.1	2.68	5.63±2.78	19
RRL03	1.525	(5.1%)	2.2	8.20	(49.4%)	
RRH01	2.401		1.3	29.51		
RRH02	2.538	2.512±0.100	1.3	31.19	32.64±4.05	20
RRH03	2.596	(4.0%)	1.2	37.22	(12.4%)	
RRL41	2.528	3.005±0.811	2.0	15.53	18.87±4.68	19
RRL42	2.546	(27.0%)	1.9	16.85	(24.8%)	
RRL43	3.942		2.0	24.22		
RRH41	2.991	2.653±0.348	1.9	17.79	27.85±8.72	20
RRH42	2.674	(13.1%)	1.3	32.86	(31.3%)	
RRH43	2.295		1.2	32.91		
RRL21	3.494	3.372±0.326	2.0	21.47	29.50±11.81	19
RRL22	3.003	(9.7%)	1.2	43.06	(40.0%)	
RRL23	3.620		1.9	23.96		
RRH21	2.270	2.913±1.006	1.2	32.55	30.64±4.95	20
RRH22	2.396	(34.5%)	1.2	34.35	(16.2%)	
RRH23	4.072		2.0	25.02		
RRL11	2.972	2.666±0.488	1.7	23.24	23.98±1.63	19
RRL12	2.103	(18.3%)	1.3	25.85	(6.8%)	
RRL13	2.923		1.7	22.86		
RRH11	2.031	2.165±0.124	1.5	19.41	20.69±1.19	20
RRH12	2.189	(5.7%)	1.5	20.92	(5.8%)	
RRH13	2.275		1.5	21.75		
RRL51	2.146	1.264±0.846	1.6	18.46	15.16±4.68	19
RRL52	1.187	(66.9%)	1.6	10.21	(30.0%)	
RRL53	0.460		0.5	18.15		
RRH51	2.726	2.513±0.410	1.6	23.45	21.62±3.53	20
RRH52	2.040	(16.3%)	1.6	17.55	(16.3%)	
RRH53	2.772		1.6	23.85		

* Error made in operating equipment

Table 2.4 Summary of Pullout Resistance, Test Series 17 to 20

	Voltage (mV)	ε_θ (10^{-6})	σ_θ (MPa)	σ_n (MPa)	τ (MPa)	Friction Coefficient μ
SG01	0.35	350	70	22.0	2.4	0.109
SG02	0.67	670	134	42.0	2.8	0.067
SG03	0.52	520	104	32.6	3.2	0.098
SG04	0.30	300	60	18.8	3.8	0.202
SG05	0.18	180	36	11.2	3.8	0.339
SG06	0.07	70	14	4.4	3.2	0.727
RG01	-0.04	-40	-8		7.6	
RG02	0.78	780	156	49.0	9.6	0.196
RG03	0.67	670	134	42.0	8.8	0.210
RG04	0.67	670	134	42.0	8.0	0.190
RG05	0.22	220	44	13.8	8.4	0.609
RG06	0.56	560	112	35.2	9.6	0.273
RG41	0.70	700	140	44.0		
RG42	0.65	650	130	40.8	8.0	0.196
RG43	0.93	930	186	58.4	11.0	0.188
RG44	0.59	590	118	37.0	9.0	0.243
RG45	0.53	530	106	33.2	7.5	0.226
RG46	0.63	630	126	39.6	7.2	0.182
RG21	0.48	480	96	30.2	7.7	0.255
RG22	0.47	470	94	29.4	8.5	0.289
RG23	-0.73	-730	-146		8.3	
RG24	0.75	750	150	47.0	7.9	0.168
RG25	1.21	1210	242	75.8	7.0	0.923
RG26	0.58	580	116	36.4	10.4	0.286
RG11	1.26	1260	252	79.0	6.9	0.087
RG12	0.59	590	118	37.0	4.9	0.132
RG13	0.74	740	148	46.4	5.3	0.114
RG14	0.81	810	162	50.8	5.6	0.110
RG15	1.08	1080	216		5.8	
RG16	1.20	1200	240	75.2	5.6	0.074
RG51	0.68	680	136	42.6	6.5	0.153
RG52	1.12	1120	224	70.2	4.5	0.064
RG53	0.49	490	98	30.8		
RG54	1.05	1050	210	65.8	6.0	0.091
RG55	0.74	740	148	46.4		
RG56	0.13	130	26	8.2		

Table 2.5 ε_θ, σ_θ, σ_n and τ after the Penetration Test, Test Series 17 to 20

Material	Shape of Fastener	Intact (s= 10 cm)	S = 4 cm	S=2 cm	S = 1 cm	S = 0.5 cm	Test Series
Gypsum Normal Specimen Size*	Sharp Type B	DP≅2.2 cm DC≅7.4 cm	DP≅2.2 cm DC≅4.0cm	DP≅2.2 cm DC≅2.0cm	DP≅2.2 cm DC≅3.0 cm	DP≅2.2 cm DC≅2.9 cm	18
Resin Normal Specimen Size*	Sharp Type B	DP≅2.2 cm DC≅5.4 cm	DP≅2.0 cm DC≅4.0 cm	DP≅1.7 cm DC= 0~2.0 cm	DP≅1.6 cm DC≅1.0 cm	DP≅1.2 cm DC≅ 0~1.0 cm	19
	Sharp Type B	DP≅1.2 cm DC= 0 cm	DP≅1.5 cm DC≅ 0~4.0 cm	DP≅1.5cm DC≅ 0~2.0 cm	DP≅1.6 cm DC≅ 0~1.0cm	DP≅ 1.6 cm DC≅ 0.5 cm	20

Definitions:

DP = Penetration Depth
DC = Crack Depth
* The normal specimen is cylindrical, 5.1cm in diameter and 10.2 cm high

Table 2.6 Summary of Penetration Depth and Crack Depth, Test Series 18 to 20

Material	Shape of Fastener	Intact (S = 10 cm)	S=4 cm	S=2 cm	S=1 cm	S=0.5 cm	Test Series
Gypsum (Normal Speciman Size#)	Sharp Base Type B	DP≅ 2.2 cm DC≅ 6.0 cm	DP≅ 2.0 cm DC≅ 4.0 cm	DP≅ 2.1 cm DC≅ 2.0 cm	DP≅ 2.3 cm DC≅ 2.0~3.0 cm	DP≅ 2.3 cm DC≅ 2.5 cm	12
	Type A	DP≅ 2.1 cm DC≅ 5.5~9.0 cm	DP≅ 2.2 cm DC≅ 4.0 cm	DP≅ 2.0 cm DC≅ 2.0~4.0 cm	DP≅ 2.0 cm DC≅ 1.9~4.5 cm	DP≅ 2.0 cm DC≅ 2.5 cm	7,8,9
	Blunt Type C	DP≅ 1.7 cm DC≅ 4.0 cm	DP≅ 2.0 cm DC≅ 4.0 cm	DP≅ 2.1 cm DC≅ 2.0~4.0 cm	DP≅ 2.3 cm DC≅ 2.0 cm**	DP≅ 2.3 cm DC≅ 2.5 ~ 3 cm	12
Gypsum (Large Specimen Size##)	Sharp Base Type B	DP≅ 2.2 cm DC*≅ 0~4.0 cm	DP≅ 2.1 cm DC≅ 4.0 cm	DP≅ 1.6~2.4 cm DC≅ 2.0 cm	DP≅ 2.4 cm DC≅ 3.0 cm	DP≅ 2.4 cm DC≅ 2.5 cm	14
Resin (Normal Specimen Size#)	Sharp Base Type B	DP≅ 1.7 cm DC≅ 5.4 cm	DP≅ 1.4 cm DC= 0 cm	DP≅ 1.8 cm DC≅ 2.0 cm	DP≅ 1.9 cm DC= 0 cm	DP≅ 1.5 cm DC≅ 0.5 cm	13
	Type A	DP≅ 2.0 cm DC≅ 6.3 cm	DP≅ 1.8 cm DC≅ 4.0 cm	DP≅ 1.7 cm DC≅ 2.0 cm	DP≅ 1.5 cm DC≅ 1.0 cm	DP≅ 1.5 cm DC≅ 1.0~1.5 cm	7, 8, 9
	Blunt Type C	DP≅ 1.8 cm DC≅ 3.3 cm	DP≅ 2.0 cm DC≅ 4.0 cm	DP≅ 1.7 cm DC≅ 2.0 cm	DP≅ 1.5 cm DC≅ 1.0 cm	DP≅ 1.2 cm DC≅ 0~0.5 cm	13

All specimens were tested under confined conditions.

DP = Penetration depth
DC = Crack Depth

* Visible crack depth
** Depth of radial cracks only; there are some cracks in the lower layers which are induced by bending of the layers.
# Normal size specimen is cylindrical, 5.1cm in diameter and 10.2 cm high.
Large size specimen is cylindrical, 10.2 cm in diameter and 20.4 high.

Table 2.7 Summary of Penetration Depth and Crack Depth, Test Series 7 to 14 (after Einstein and Jeng, 1988)

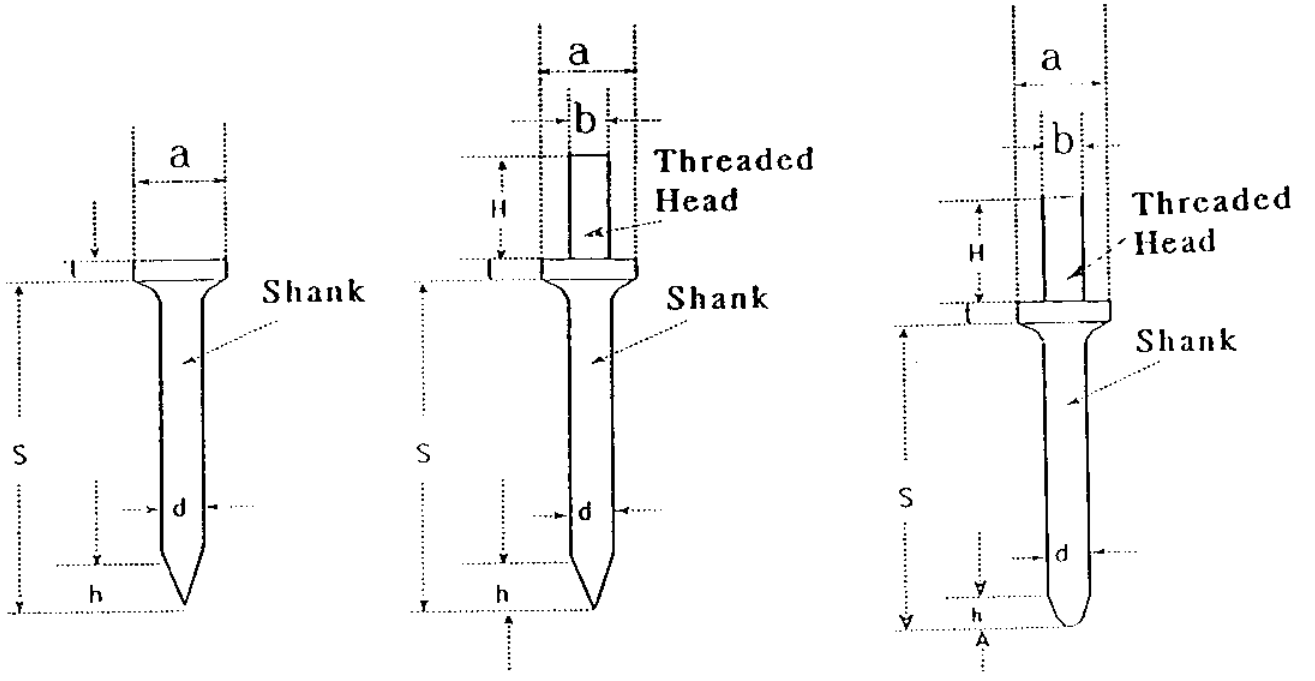

S = 20 mm
h = 6 mm
t = 2.3 mm
d = 3.4 mm
a = 7.9 mm

Type A

S = 25.4 mm
H = 15.2 mm
h = 6 mm
t = 1.5 mm
d = 3.7 mm
a = 8.0 mm
b = 6.2 mm

Type B

S = 23 mm
H = 15.2 mm
h = 4 mm
t = 1.5 mm
d = 3.7 mm
a = 8.0 mm
b = 6.2 mm

Type C

Figure 2.1 Geometry of Penetrators

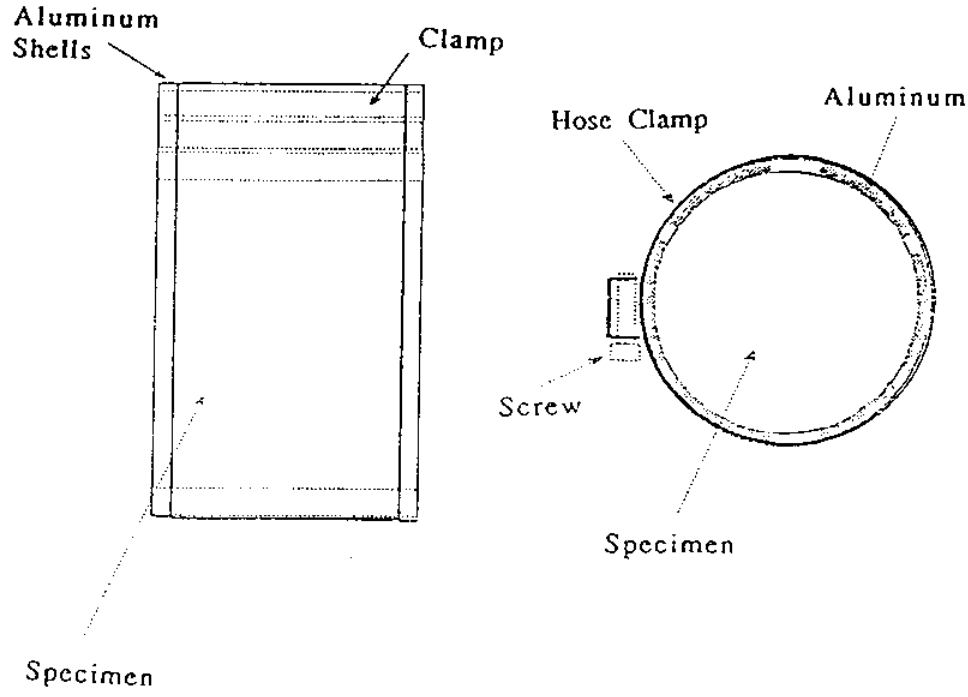

(a)

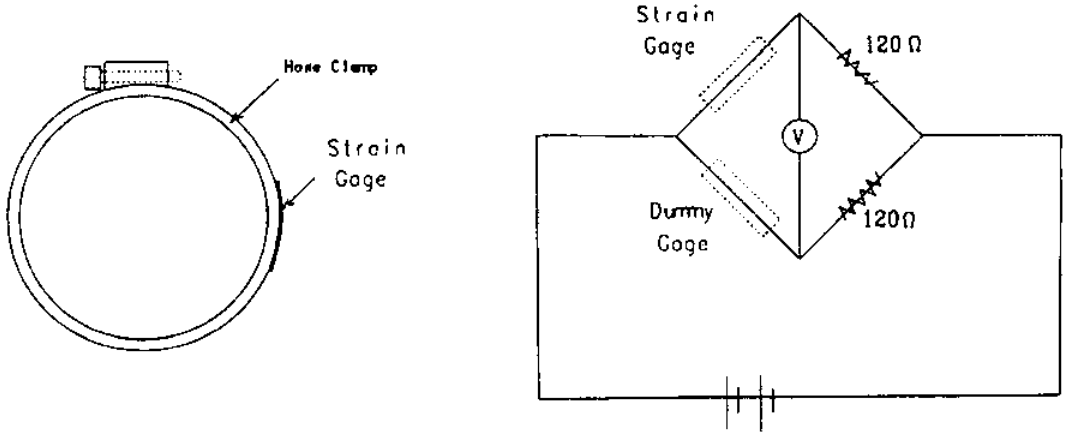

1/2 Wheatstone Bridge

(b)

Figure 2.2 (a) Confinement with Aluminum Shells and Clamps
(b) Strain Gage Configuration

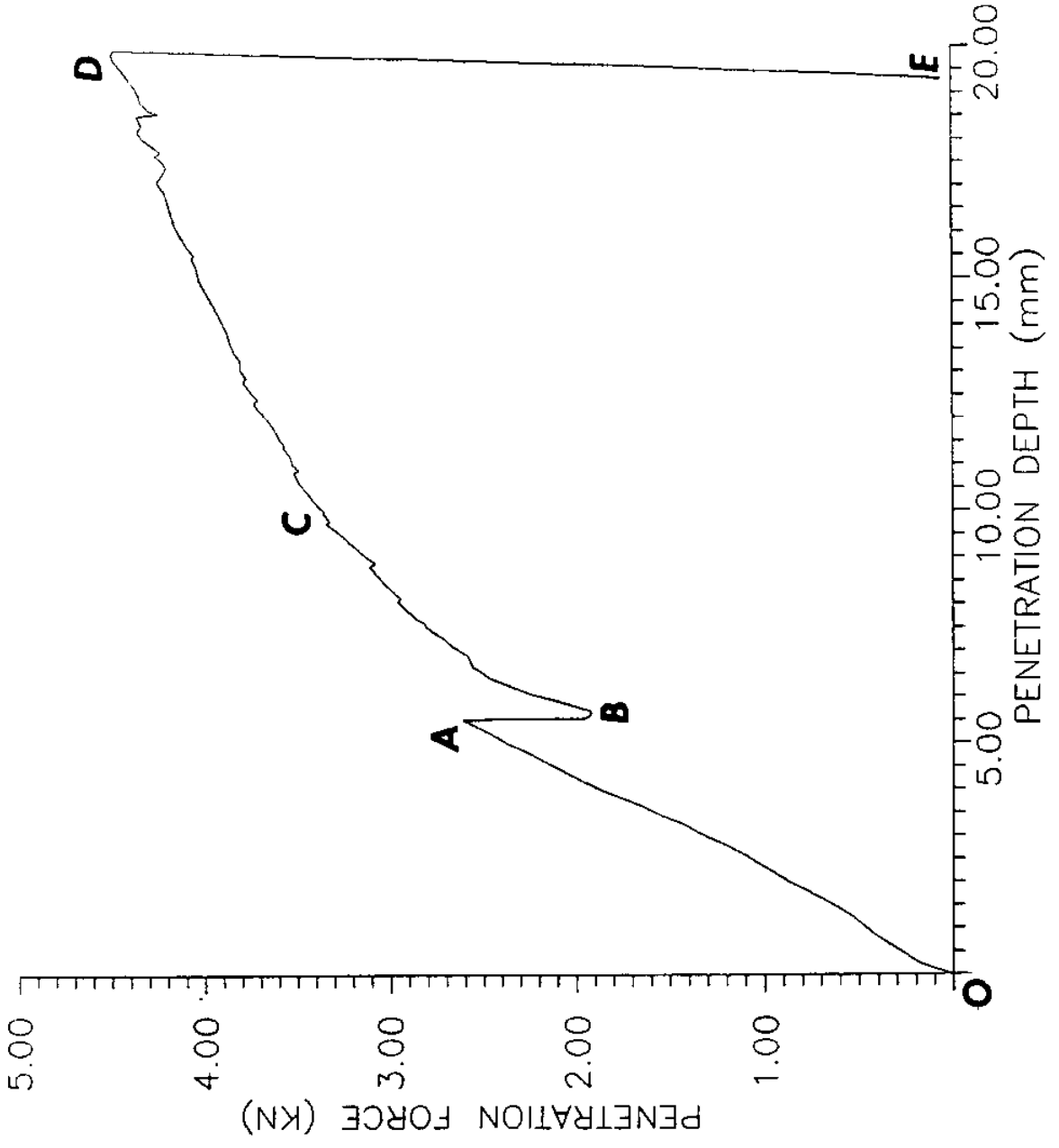

Figure 2.3 Typical Slow Penetration Force vs. Penetration Depth Curve (for Gypsum)

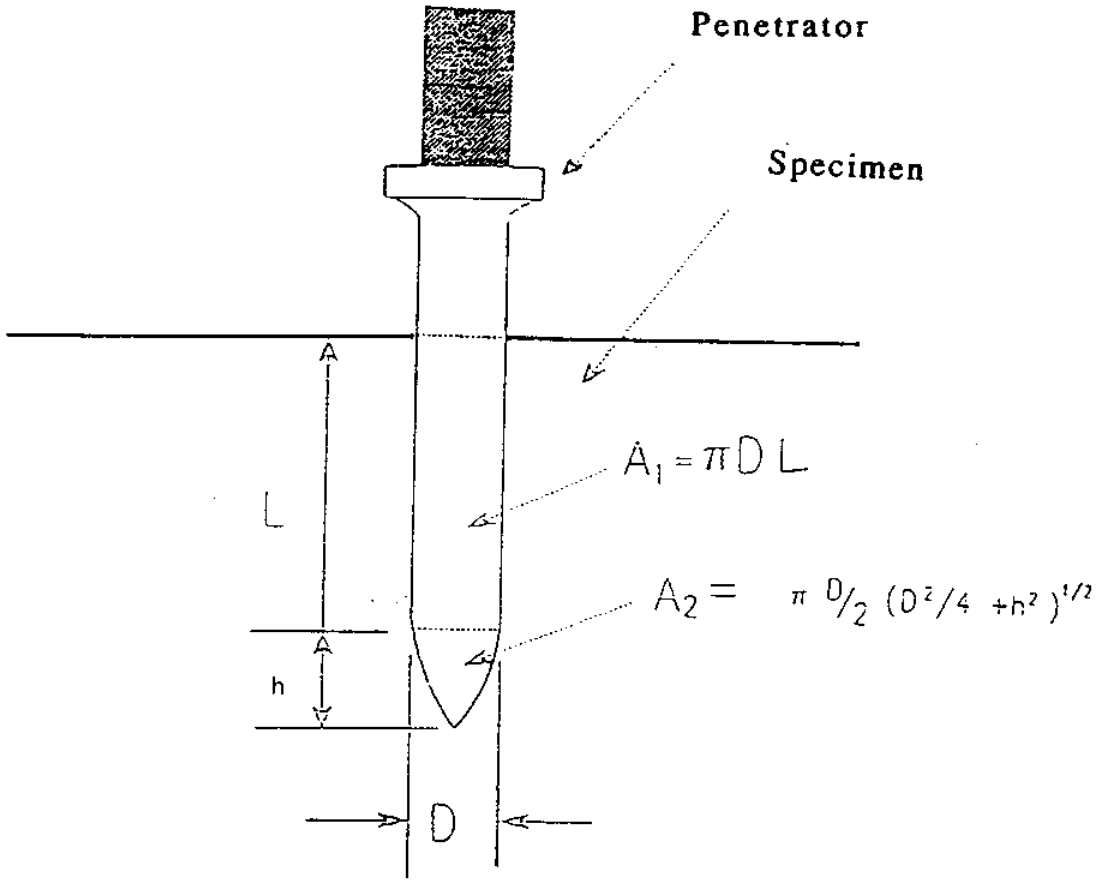

Embedded Area = $A_1 + A_2$

Figure 2.4 Definition and Calculation of Embedded Area

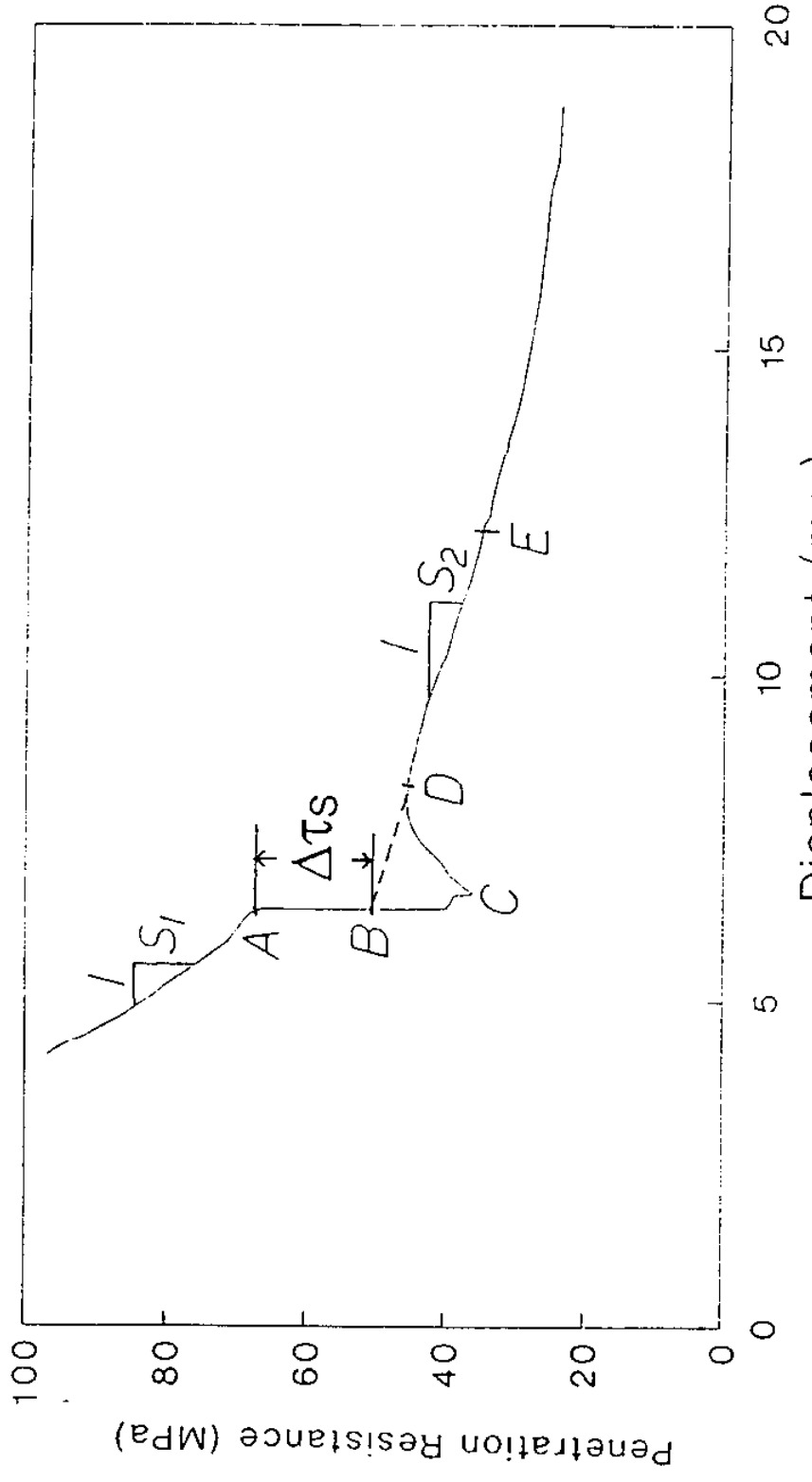

Figure 2.5 Typical Slow Penetration Resistance vs. Displacement Curve

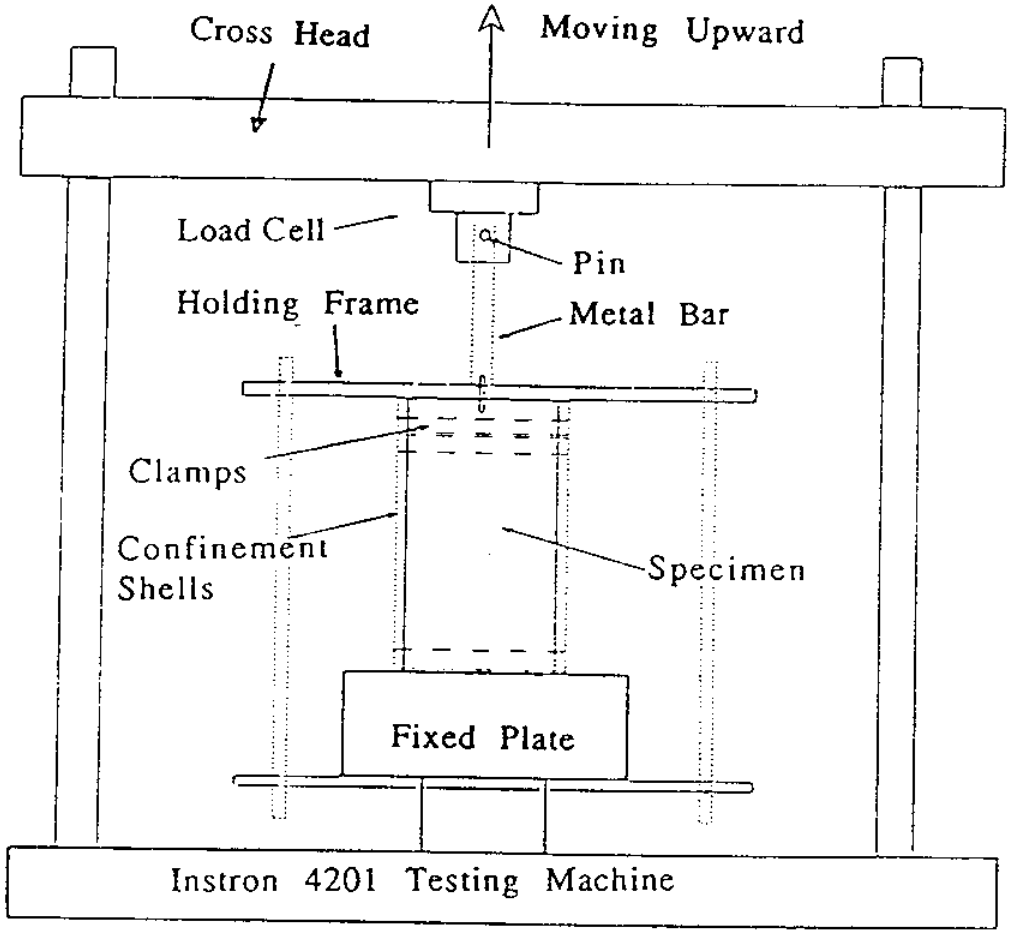

Figure 2.6 Setup for Pullout Test

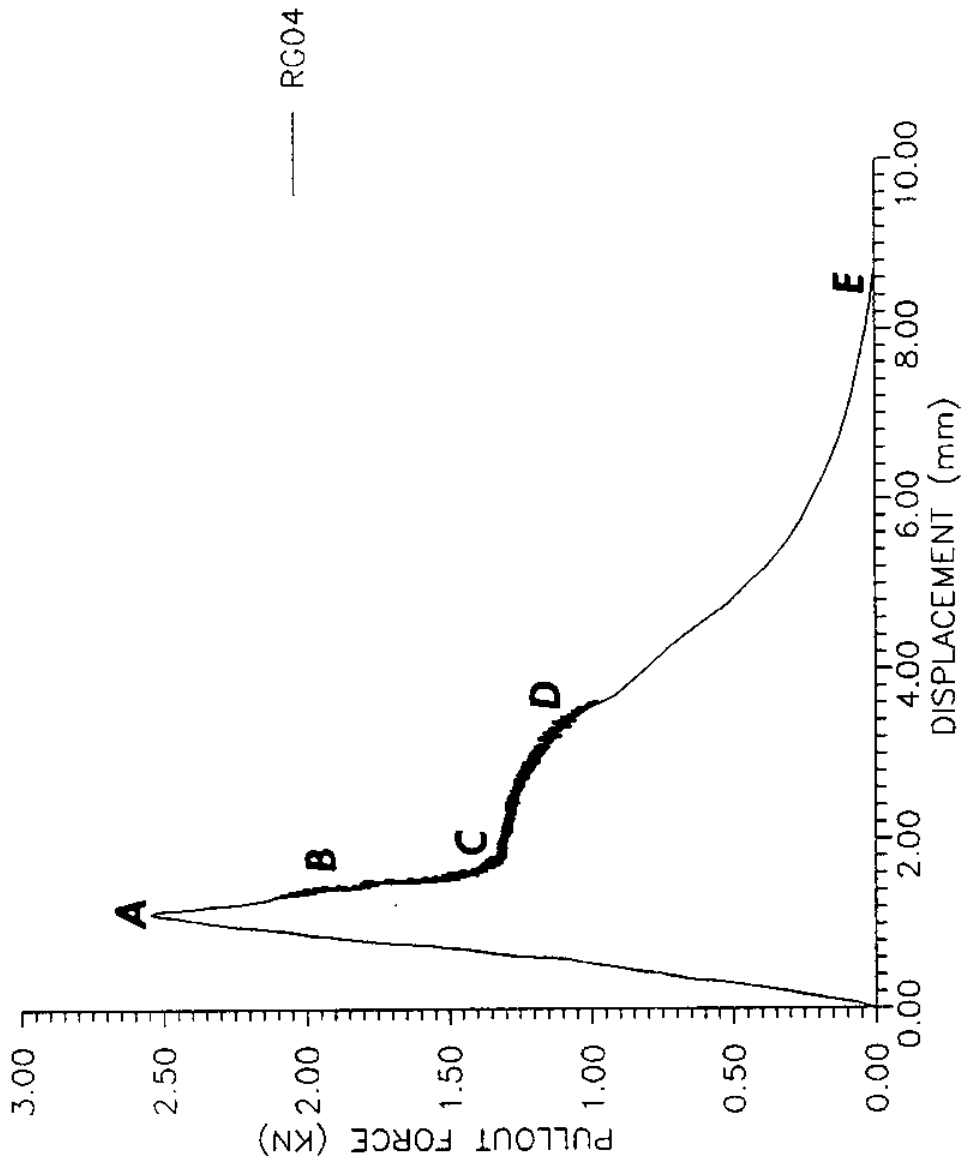

Figure 2.7 Typical Pullout Force versus Displacement Curve for Gypsum Specimens

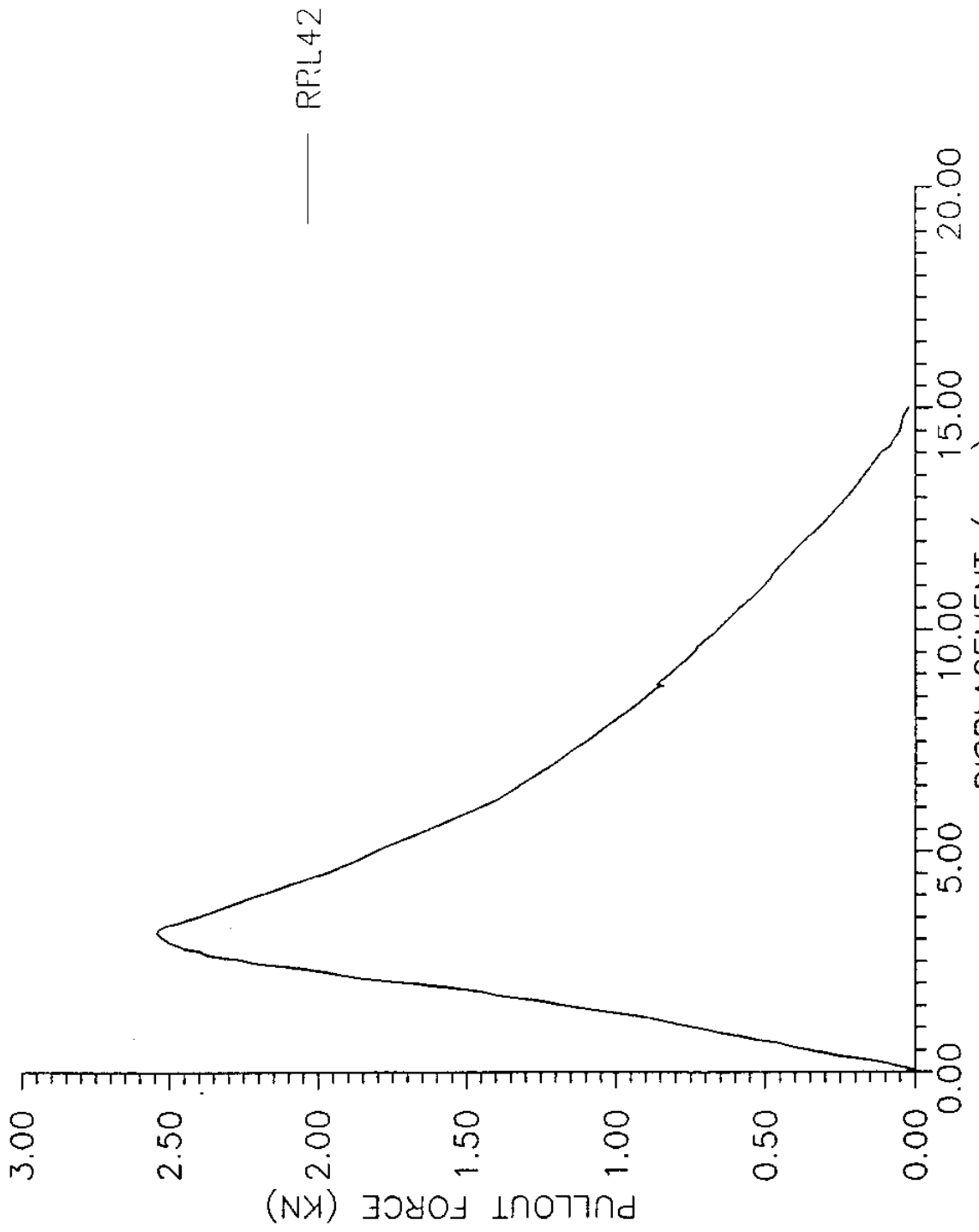

Figure 2.8 Typical Pullout Force vs. Displacement Curve for Resin Specimens

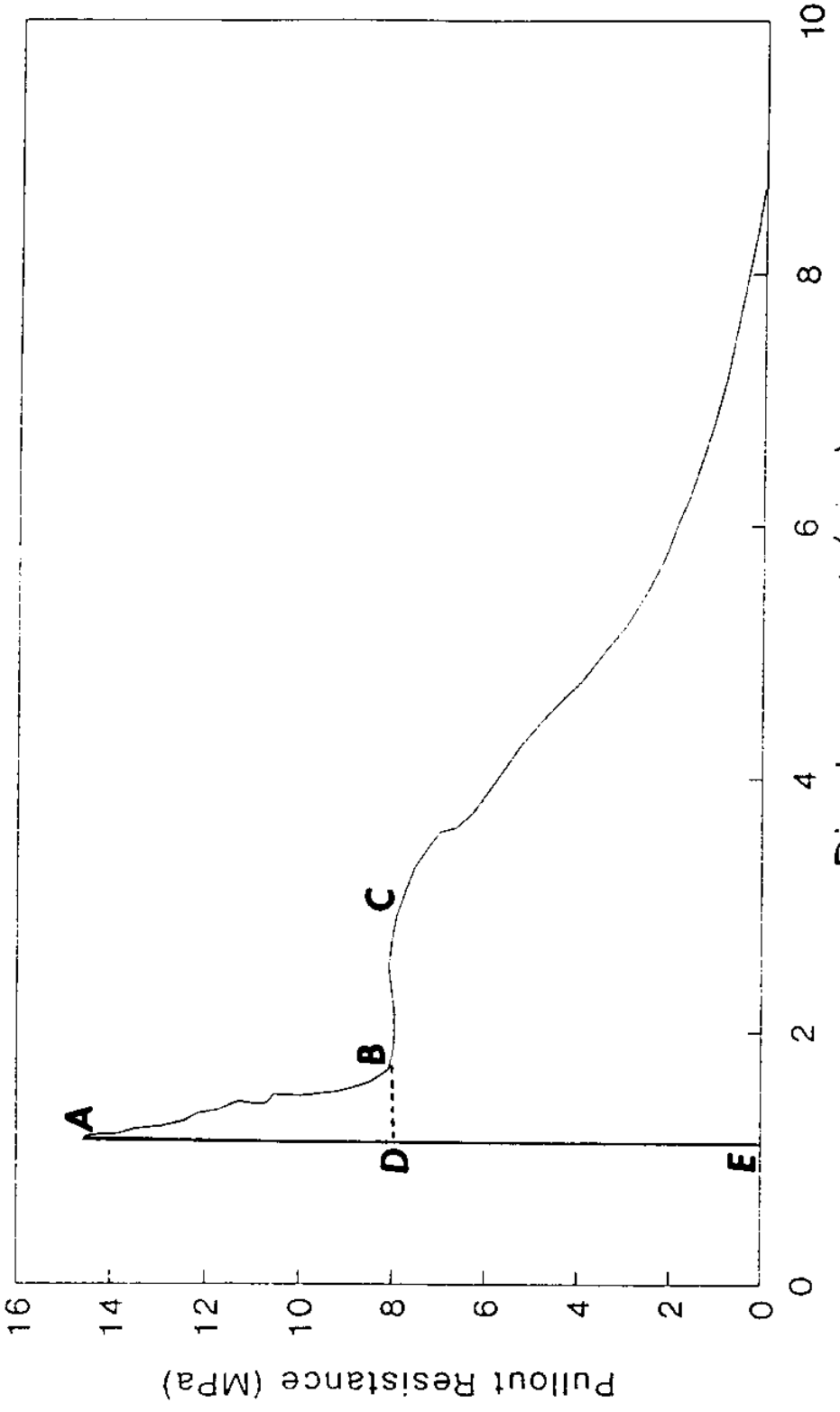

Figure 2.9 Typical Pullout Resistance vs. Displacement Curve for Gypsum Specimens

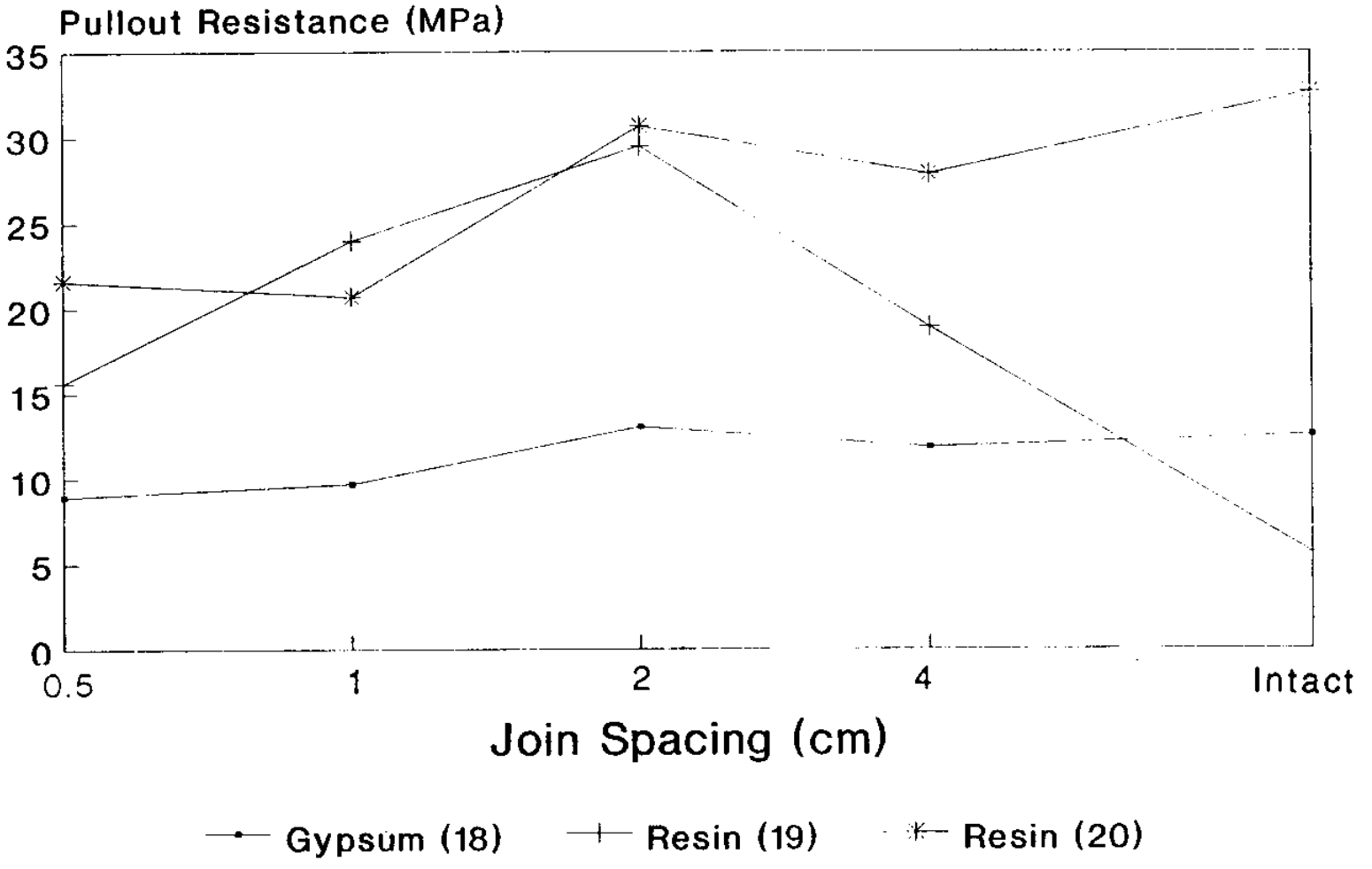

Figure 2.10 Pullout Resistance vs. Joint Spacing Curve for Test Series 18, 19 and 20

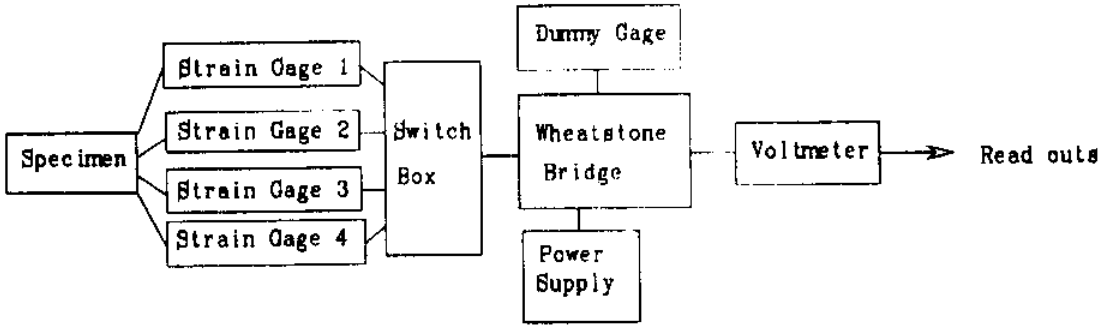

(a) Setup of Strain Measuring Devices

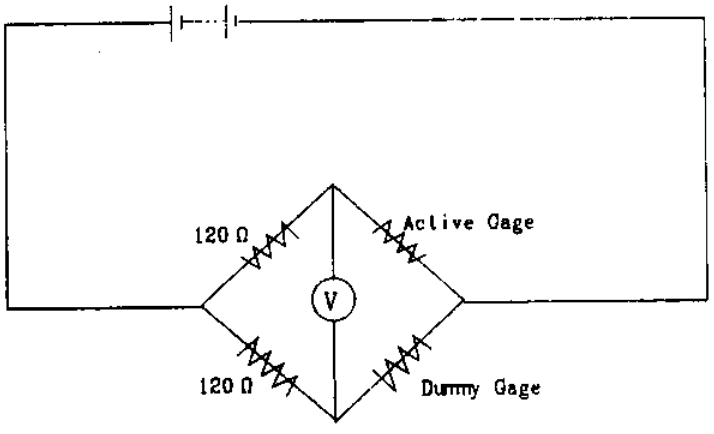

(b) 1/2 Wheatstone Bridge

Figure 2.11 Measurement of Circumferential Strains

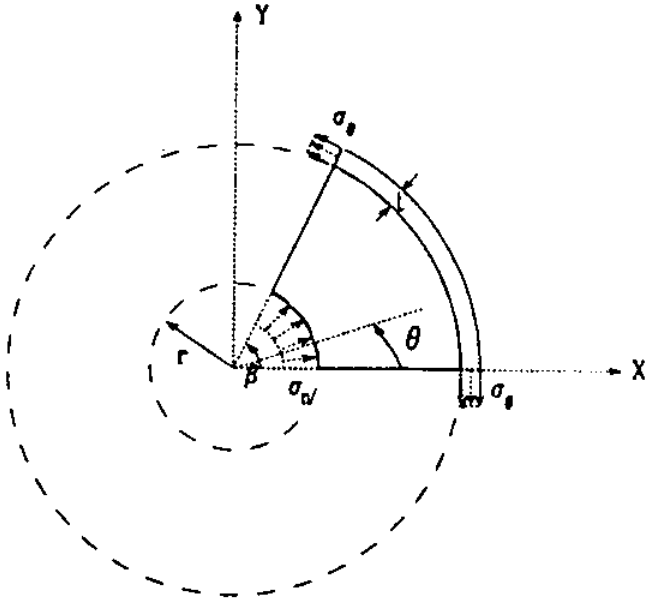

Assume 2–dimensional analysis is applicable : σ_z, σ_{rz}, $\sigma_{\epsilon z} = 0$

Consider the balance of forces in the X direction :

$$\int_0^{\beta} \sigma_n \, r \cos\theta \, d\theta = (\sigma_\theta \, t) \sin\beta \qquad (1)$$

The integration of eqn. (1) gives

$$\sigma_n \, r \sin\beta = \sigma_\theta \, t \sin\beta \qquad (2)$$

Hence, from eqn. (2), σ_n can be obtained from σ_θ :

$$\sigma_n \big|_{shank} = \frac{t}{r} \sigma_\theta \big|_{boundary} \qquad (3)$$

The dimensions of t and r are :

t = 0.58 mm and r = 1.85 mm

Finally,

$$\sigma_n \big|_{shank} = 0.314 \, \sigma_\theta \big|_{boundary} \qquad (4)$$

Figure 2.12 Relationship between Confining Stresses σ_θ and Normal Stresses Acting on the Shank of the Penetrator σ_n

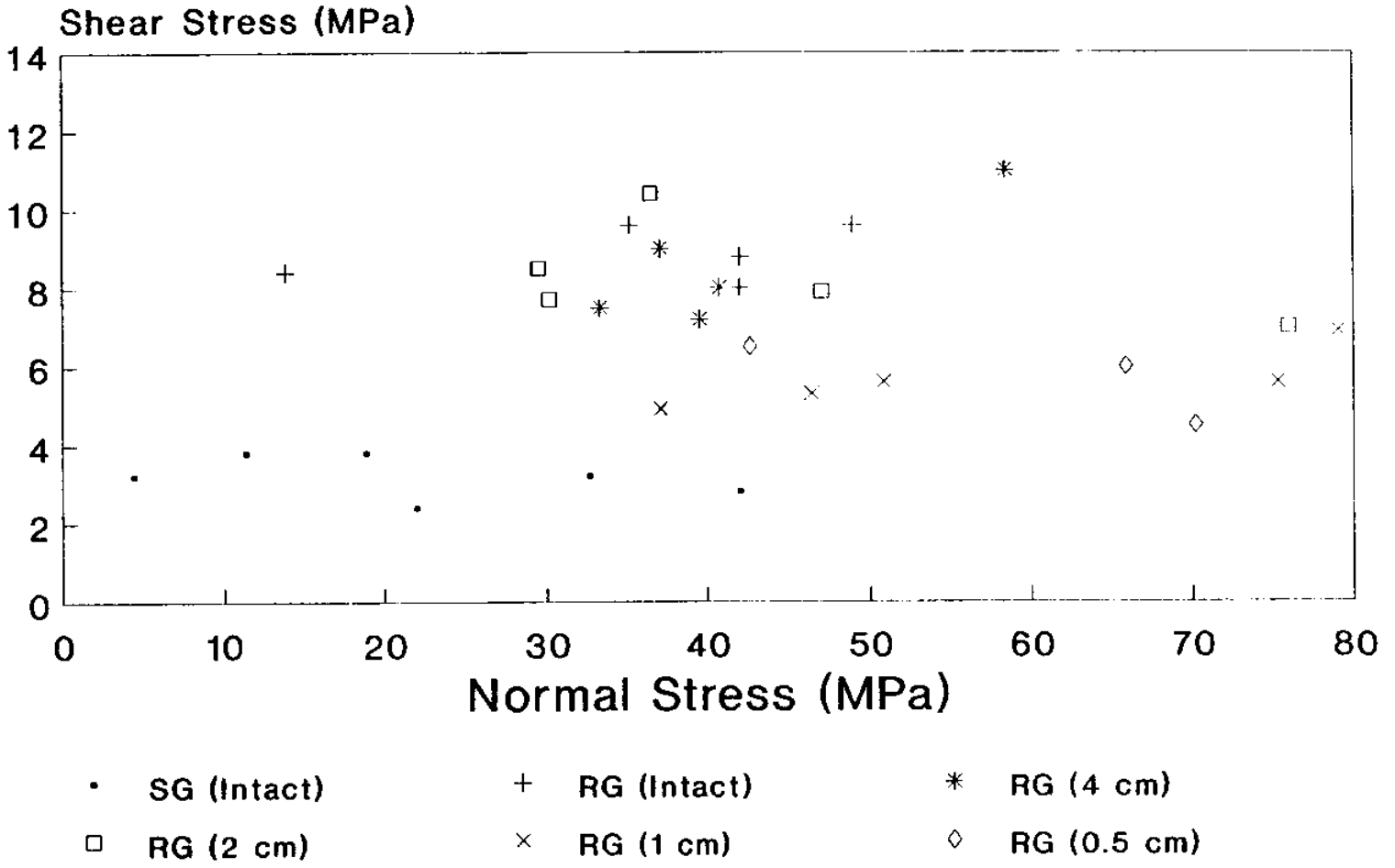

Figure 2.13 Normal Stresses and Shear Stresses Acting on the Penetrator Shank

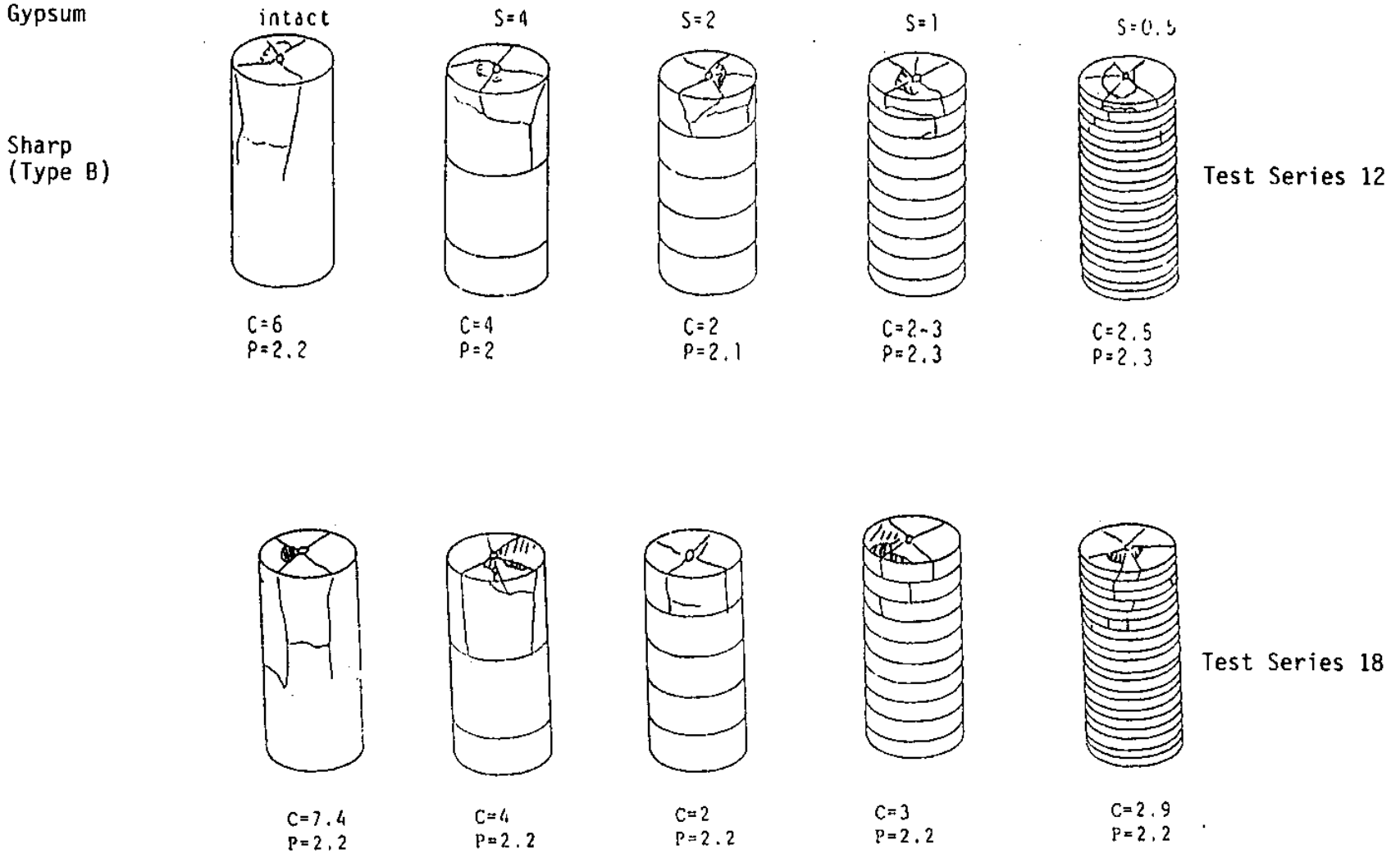

Figure 2.14 Comparison of Fracture Phenomena, Test Series 12 with 18

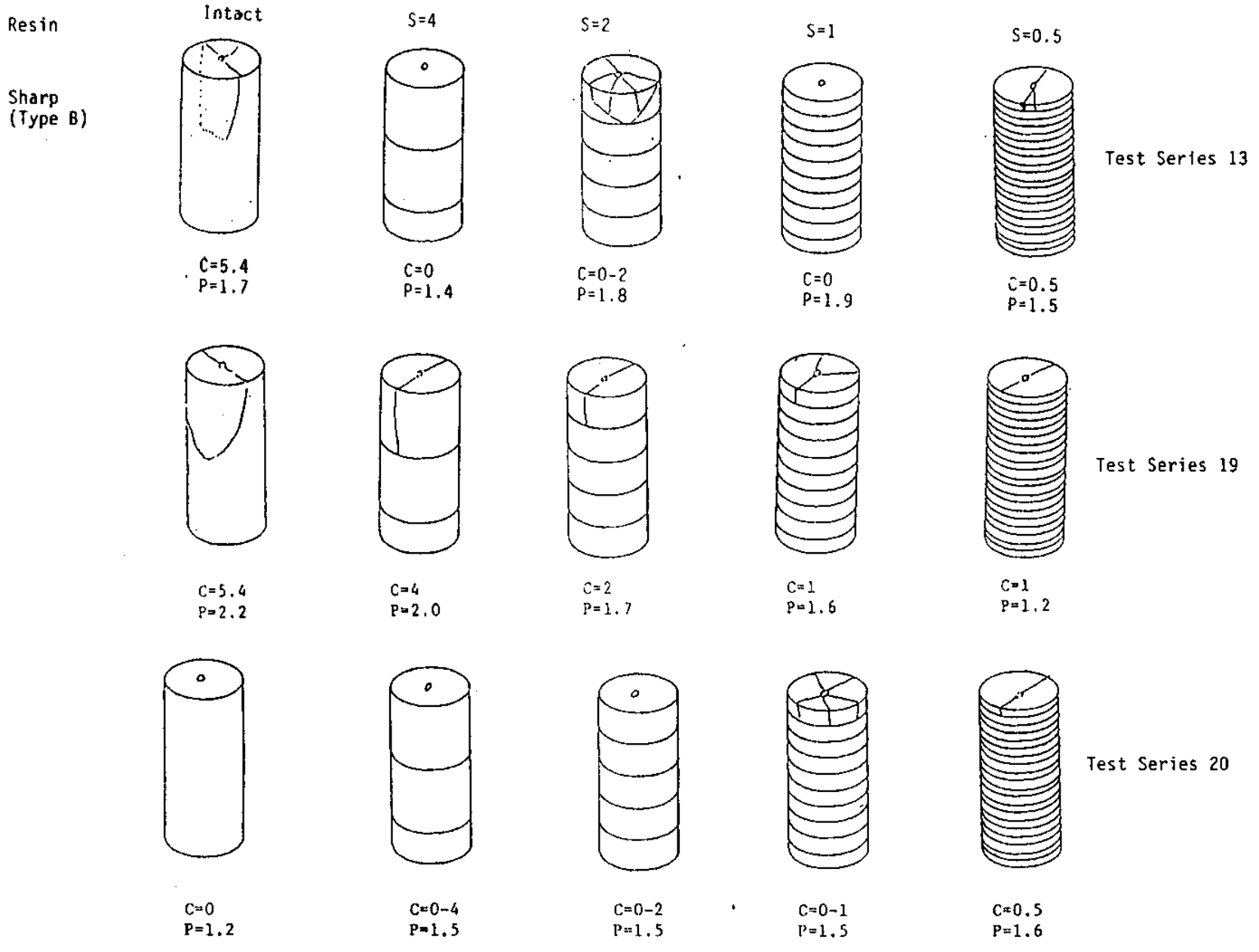

Figure 2.15 Comparison of Fracture Phenomena, Test Series 13, 19 and 20

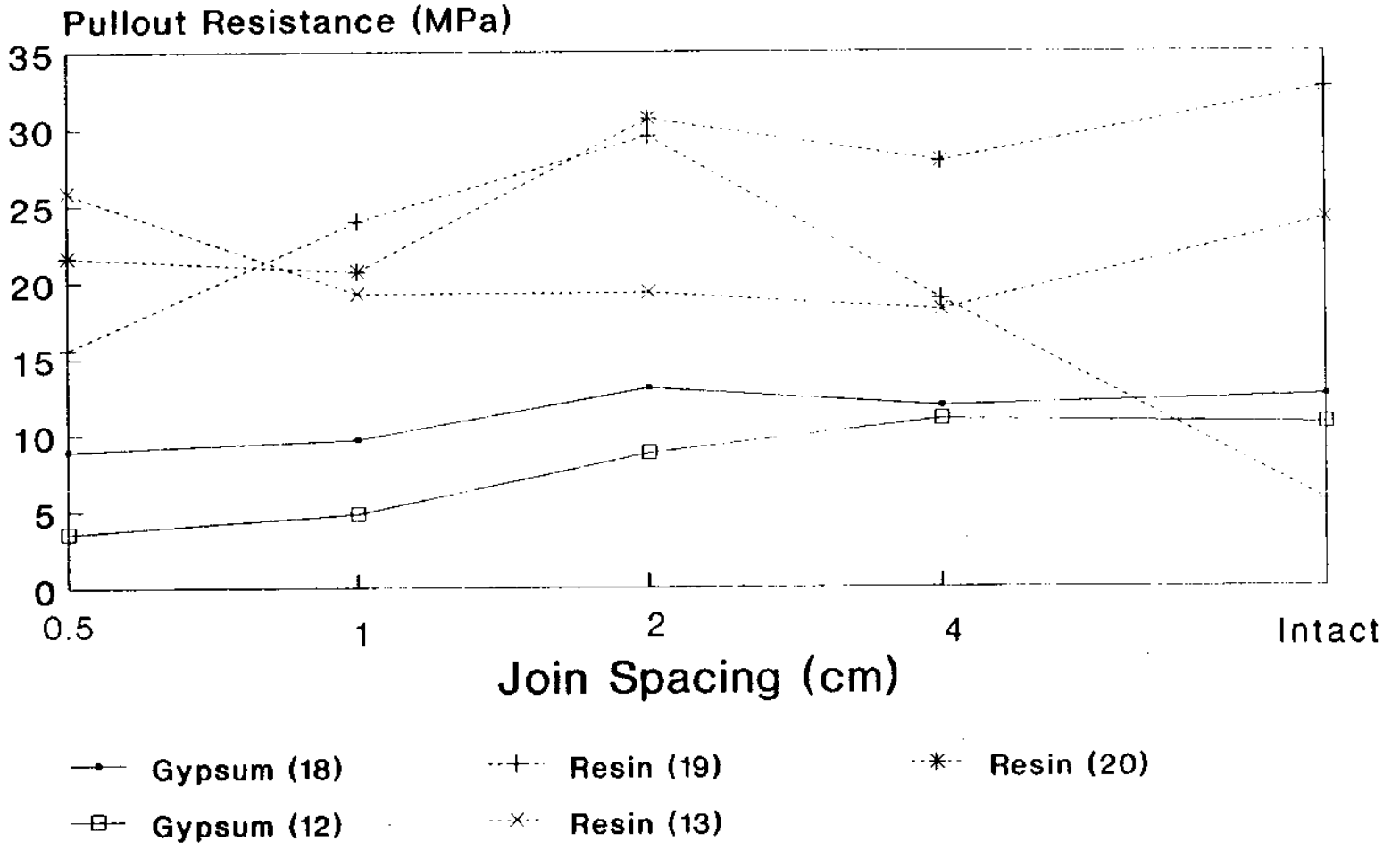

Figure 2.16 Pullout Resistance vs. Joint Spacing, Comparison of Test Series 12, 13, 18, 19 and 20

CHAPTER 3
PREPARATION OF MAJOR TEST SERIES

3.1 Introduction

Validation testing of the penetration-pullout models requires measurement of the penetration force-displacement and pullout force-displacement history as well as knowledge of the stress state in the medium and, if possible, at the penetrator/medium interface. These measurements will be supplemented by observations of the crack pattern and fractography. Based on the preceding test series using a nail (fastener) gun and gypsum and resin models (see Einstein et al., 1987; Einstein and Jeng, 1988) we decided to use a similar setup but with the appropriate instrumentation added. The instrumentation has to include an accelerometer on the penetrator and devices for accurate measurement of stresses acting on the model (confining stresses and eventually also interface stresses). The size of the penetrator and of the model was doubled compared to the previous tests to make use of commercially available accelerometers and particularly to make it possible to install sleeves on the penetrator for measuring the interface stresses. As discussed in Einstein and Jeng (1988), two of the three scale effects, the intact size effect and the joint spacing effect can be adequately considered with equipment and models of the chosen size. The third scale effect, affecting joint shearing, is of minor importance in the penetration problem. Nevertheless, it is possible to double the size of the penetrator and the model, the only limitation being the propellant energy provided by the fastener gun. The model materials, in particular, the gypsum, will remain the same as before, since it will allow us to easily relate the results to those of the preceding tests and to the many other tests on this material conducted by the MIT rock mechanics group.

The design of the system required a substantial effort, in particular, the selection of the dimensions as well as the fabrication of the gun piston and of the penetrator/sleeve. The "accelerometer-signal conditioner-data acquisition" system was configured, and to some extent built by us; we also wrote the data acquisition program

to optimize between collecting a large number of data and storing the relevant data.

The system was successfully calibrated and tested. Details of the design and of the calibration and shake down tests are given below.

3.2 Description of the Experimental Setup

The experimental setup consists of the penetrator, model specimen, nail gun, accelerometer for the penetrator, signal conditioner, data acquisition system and computer. The setup is shown schematically in Fig. 3.1. When the trigger of the gun is pulled, setting the penetrator in motion, the data acquisition system is activated to read signals from the accelerometer attached to the penetrator. Voltage signals from the accelerometer are amplified by the signal conditioner to levels that can be read by the data acquisition system. After the test, the readings stored in the data acquisition system are transferred to the computer for reduction and analysis.

3.2.1 Penetrator and Piston

The penetrator is attached to the piston of the gun and is instrumented with an accelerometer. The details are shown in Fig. 3.2. The total mass is 293 grams. The penetrator is cone-tipped (angle=16.4°) of diameter 0.236" and made of high-carbon steel with its tip heat-treated. Other shapes and sizes can be fabricated and easily attached to the piston. It is planned to eventually add a sleeve and cross strain gages (see Fig. 3.3) to the shaft of the penetrator to measure axial and radial strains with which the stresses on the penetrator can be determined.

3.2.2 Model Specimen

The model specimen is cylindrical, 4" in diameter and 4" high. It is confined by a series of circular stainless steel clamps throughout its height. Three strain gages are attached to each clamp to measure circumferential strains, before and during the penetration test as well as during the pullout test.

3.2.3 Nail Gun

A Hilti DX-600N powder actuated nail gun is used to propel the penetrator. The muzzle of the gun was removed such that the newly designed piston-penetrator assembly can be inserted into the gun.

3.2.4 Accelerometer

The accelerometer used to determine the acceleration history of the penetrator has the following specifications:

Endevco model 7225-01
Minimum range: 50,000g
Frequency response: 10 Hz to 10 kHz
Sensitivity: 0.10 mV/g

It is located in a ring connecting the penetrator and the piston of the gun (see Fig. 3.2).

3.2.5 Signal Conditioner

An Endevco model 2775A signal conditioner was used to amplify signals coming from the accelerator in millivolts to volts.

3.2.6 Data Acquisition System

The signals from the accelerometer as amplified by the signal conditioner are read and recorded by a Hewlett-Packard 4882 high-speed data acquisition system. The system can process 10^5 readings per second and store up to 64,000 readings in its memory.

3.2.7 Computer

A HP personal computer is used to control the test. Also, it is used to transfer the readings stored in the data acquisition system to an IBM personal computer for reduction and analysis.

3.3 Efforts in Setting-up the Test Equipment and Shake Down Tests

To make the test equipment work, several technical problems had to be overcome. The major effort was aimed at obtaining a sufficient number of high quality data during the penetration process.

A series of preceding tests were conducted to get an idea on the penetration duration, which was found to be in the range of milliseconds (between 1 and 9 milliseconds). Hence, to get the necessary resolution, a HP-4882 high speed data acquisition system was chosen. The HP system is programmed and controlled by a HP computer. At first, a program was developed to control the HP system, to retrieve the data from the Random Access Memory (RAM) of the HP system and to reduce the data. The HP system can take up to 100,000 readings per second. However, to utilize the full capacity of the HP system, it is necessary that it is not interrupted during the data collection process (e.g., by communication of the computer with data acquisition system). To meet such a requirement, all the data need to be stored in the HP RAM, which can store up to 64,000 readings. This reduces the available measuring period to only 0.64 seconds. A trigger was then designed to start the HP system right before the gun booster is activated to contain the penetration period within the measuring window. After a series of trials and calibration, we are able to place the penetration period in the first 0.15 seconds.

Another technical problem encountered is that the noise level is too high to get a clear acceleration history. Through detailed checking and understanding the data acquisition system and the signal conditioner, we were able to solve this problem by jumping the ground connections of the data acquisition system and the signal conditioner.

After these efforts, the entire equipment was used to run three shake down tests.

The Hilti 600N nail gun is designed to use caliber 0.27 boosters with four power levels which are marked by green (the lightest), yellow, red and purple (the heaviest) colors. In the first test, the yellow booster (medium power) was used and the penetrator was shot into a piece of wood. The reason for choosing wood for the first test is that it is weaker and softer than gypsum, and thus a lower deceleration is expected; this reduces the possibility of damaging the accelerometer. The acceleration/deceleration history was recorded during the entire penetration process, which includes propelling the penetrator and the impact and arrest stages. An acceleration vs. time

(a-t) curve is obtained. The integration of the a-t curve provides a velocity vs. time (v-t) curve. A displacement vs. time (d-t) curve, in turn, is obtained by integrating the v-t curve. These curves (a-t, v-t and d-t) are shown in Figs. 3.4a, b, and c.

As shown in Fig. 3.4a, the duration of the entire penetration process is about 6 milliseconds. The a-t curve shows the expected acceleration/deceleration history with an acceleration caused by the booster explosion, a deceleration upon impact and a final stop. The irregularities (secondary waves) are caused by the vibration of the penetrator-target system, which behaves like a mass-spring system subjected to force pertubation during the penetration.

The total area enclosed by the a-t curve is not exactly equal to zero which leads to a final velocity which is not exactly zero (at rest), as shown in Fig. 3.4b. This deviation is relatively small but has to be corrected through more work: 1) calibration and 2) the use of better numerical methods to integrate the a-t and the v-t curve. The d-t curve is shown in Fig. 3.4c. The last segment (AB) should be horizontal, if the final velocity is zero.

In the first test, the maximum acceleration is about 5,000g and the maximum deceleration is about 1,300 g, which are much lower than the capacity of the accelerometer (50,000g in all directions). The maximum acceleration/deceleration here is the value at the mid-amplitude of the secondary waves in the a-t diagram.

In the second test, the yellow booster and Hydrocal White gypsum were chosen. The test results (a-t, v-t and d-t curves) are shown in Figs. 3.5a, b and c. As shown in Fig. 3.5 the maximum acceleration is about 5,000g and the maximum deceleration is about 2,000g. Since the yellow boosters were used in both tests 1 and 2, the same maximum accelerations were recorded. The maximum deceleration in the second test is higher than that in the first test, which agrees with the higher resistance of the gypsum as compared to wood.

In the third test, the purple (the heaviest) booster and Hydrocal B-11 (which has higher strength than Hydrocal White) were used. The test results are shown in Figs. 3.6a, b and c. The maximum acceleration is about 8,000g and the maximum deceleration is about

4,000g, the increase of these values relative to the other tests being caused by the heavier booster and stronger material, respectively.

As one could imply from a cursory inspection of the v-t curves (Figs. 3.4b, 3.5b and 3.6b), the impact velocity in all tests is about 25 m/sec. However, as mentioned above, the final velocity is supposed to be zero when the penetrator is arrested. If the final velocity is set to zero (by shifting the v-t curve upward), the impact velocities are approximately about 30, 30 and 40 m/sec respectively, which reflects the effect that the stronger booster also produces the higher impact velocity.

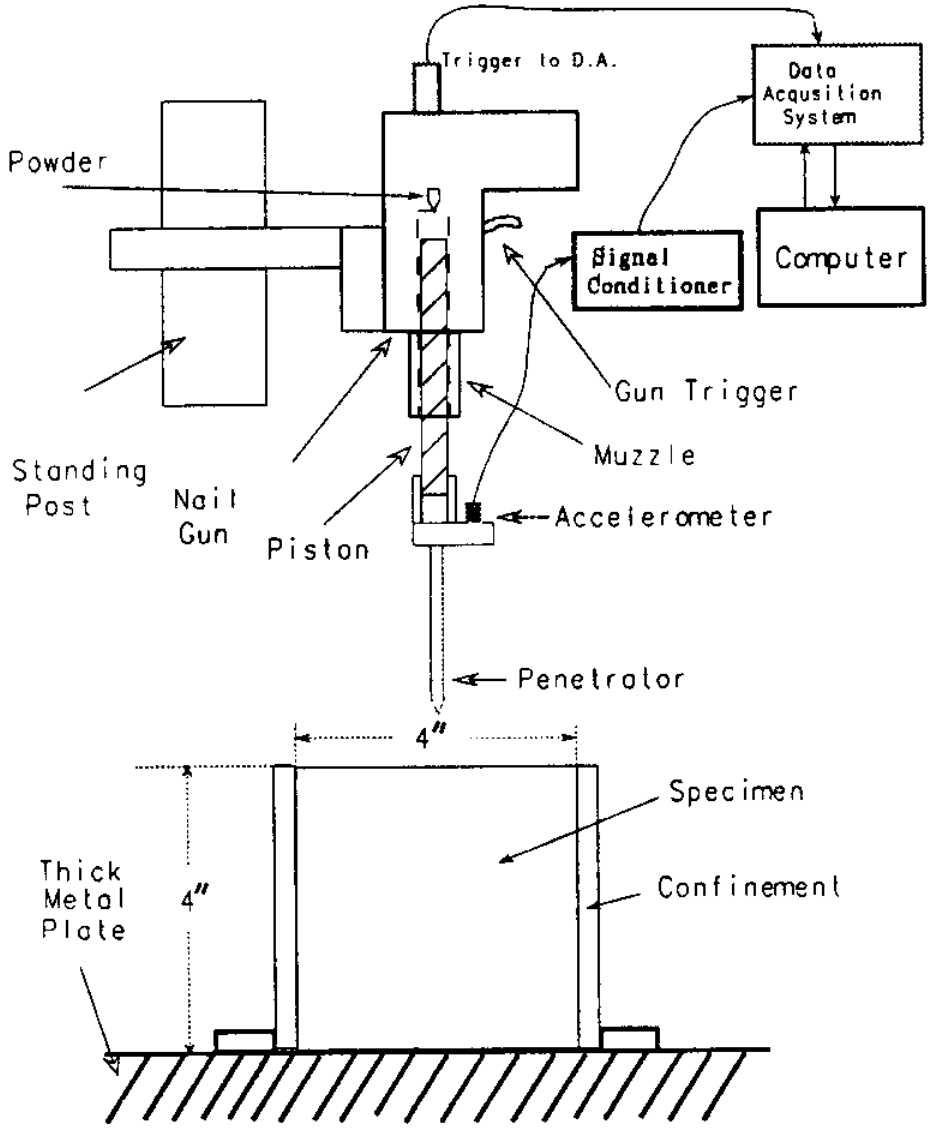

Fig. 3.1 Schematic Diagram of the Penetration Test Equipment

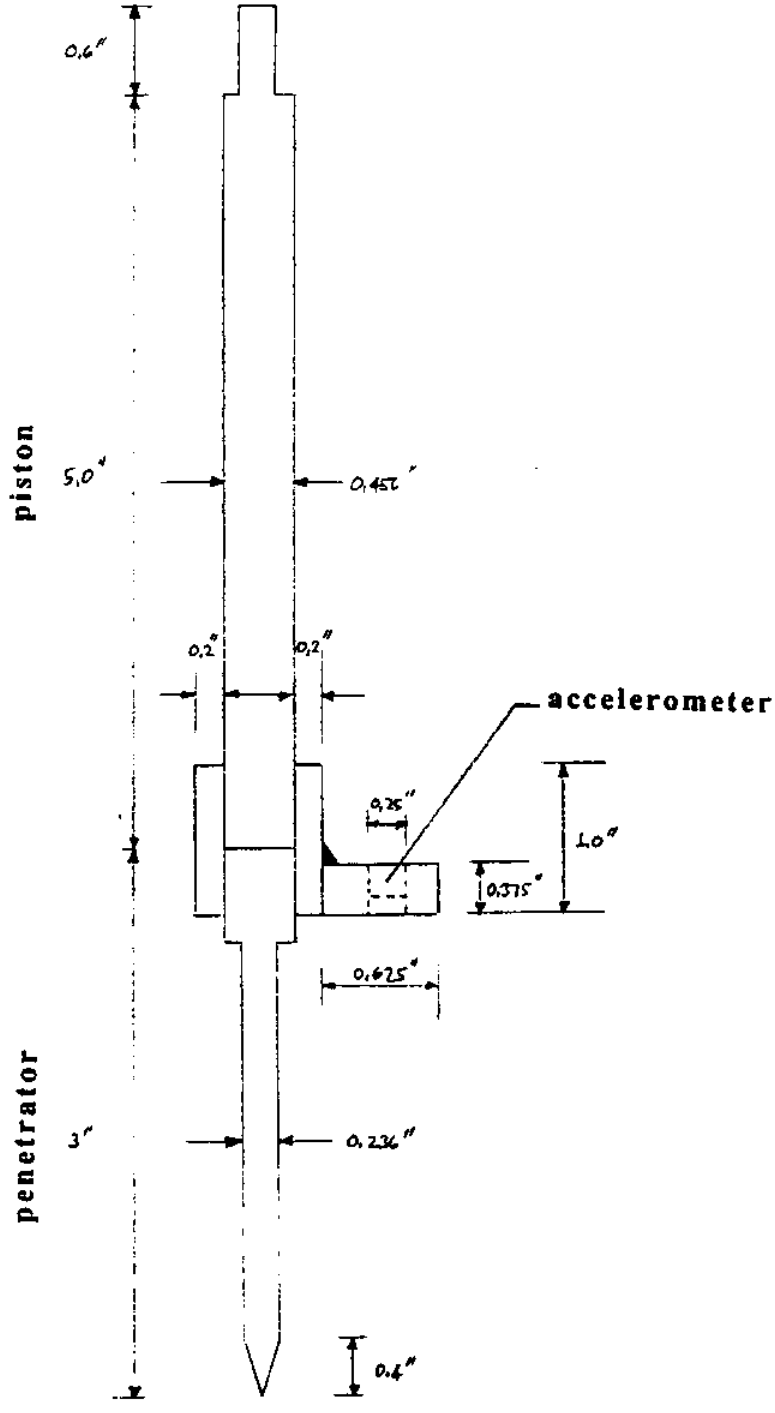

Fig. 3.2 Detail of Penetrator and Piston

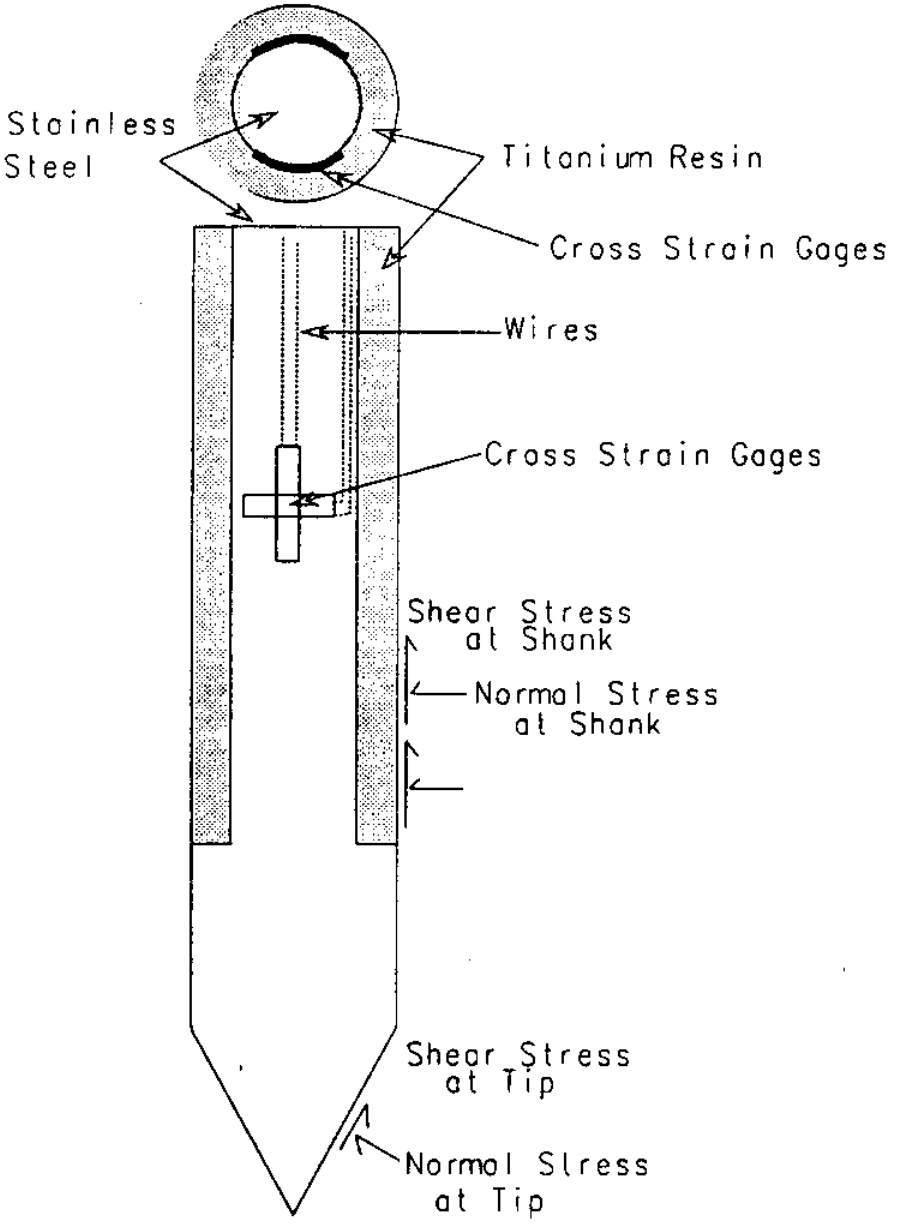

Fig. 3.3 Detail of Penetrator Sleeve and Strain Gages

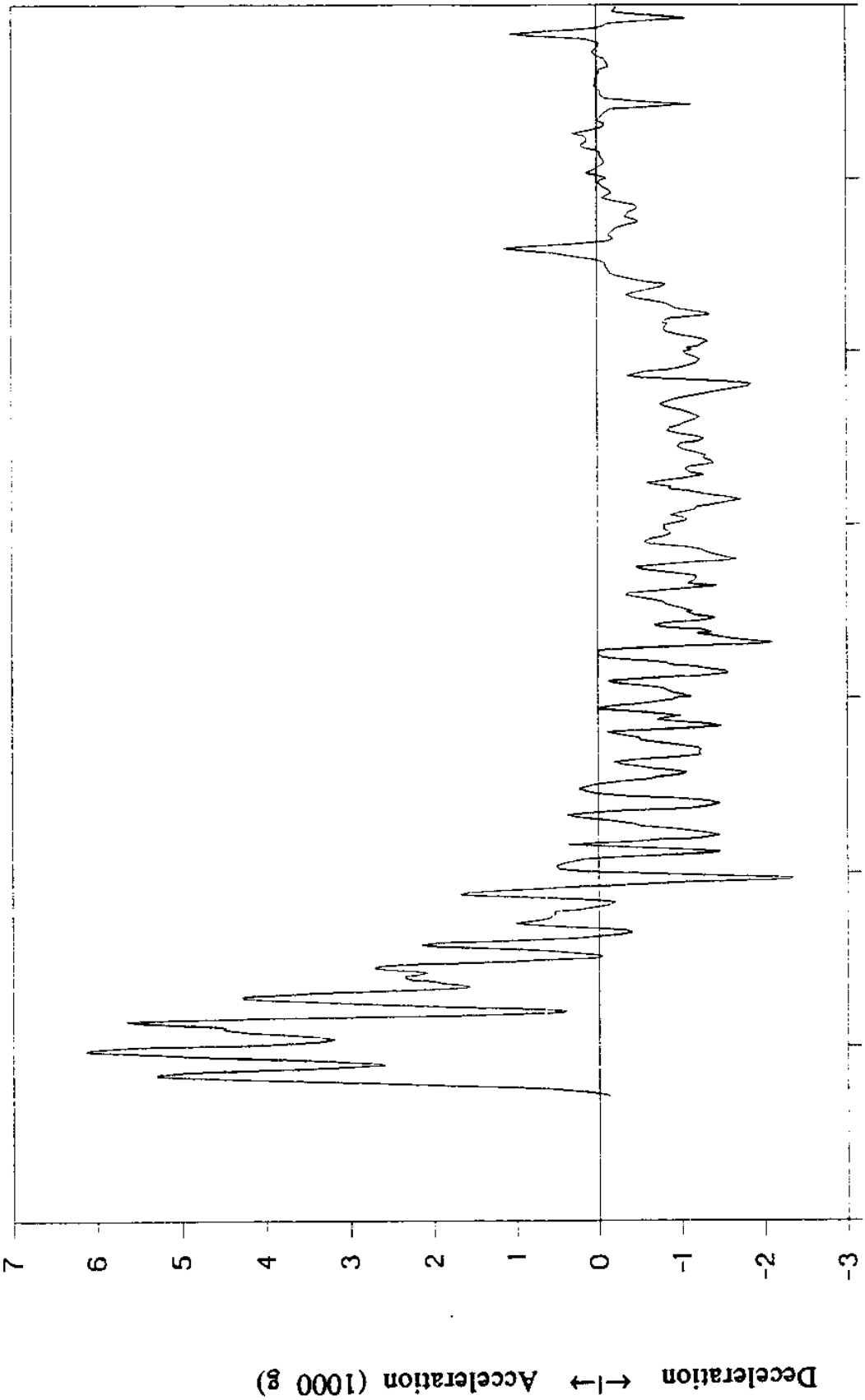

Figure 3.4a. Acceleration vs. Time Curve of the First Test

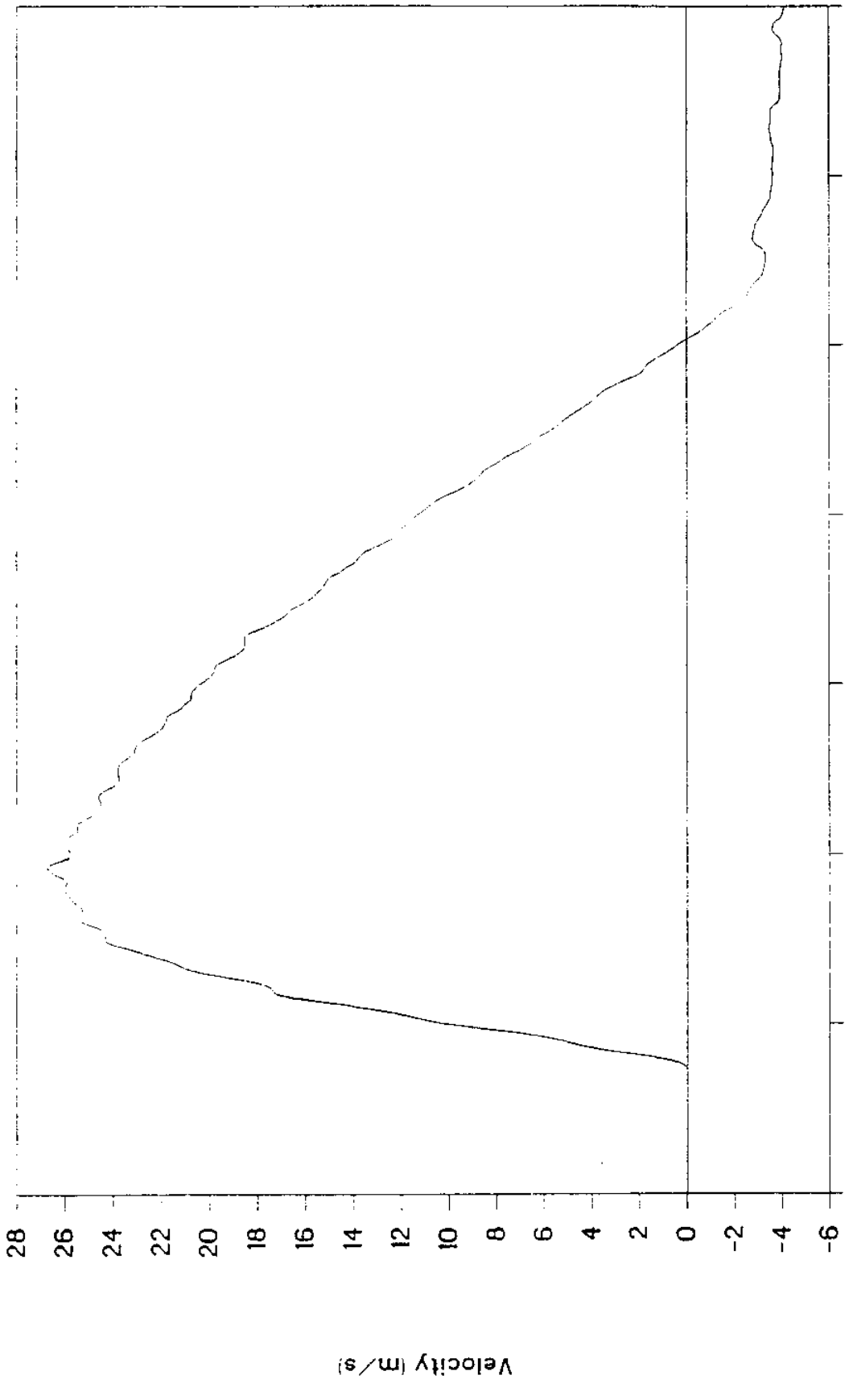

Figure 3.4b. Velocity vs. Time Curve of the First Test

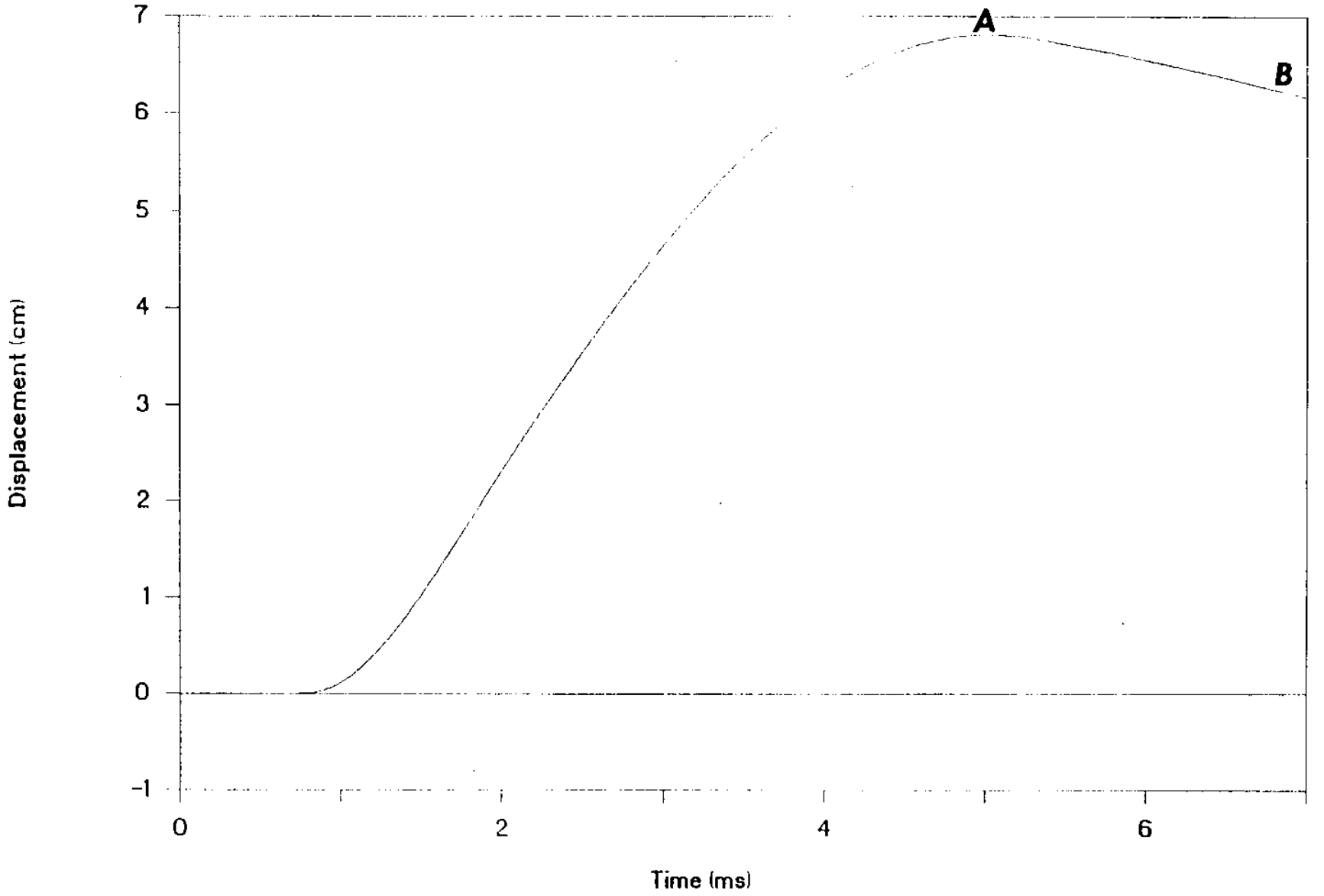

Figure 3.4c. Displacement vs. Time Curve of the First Test

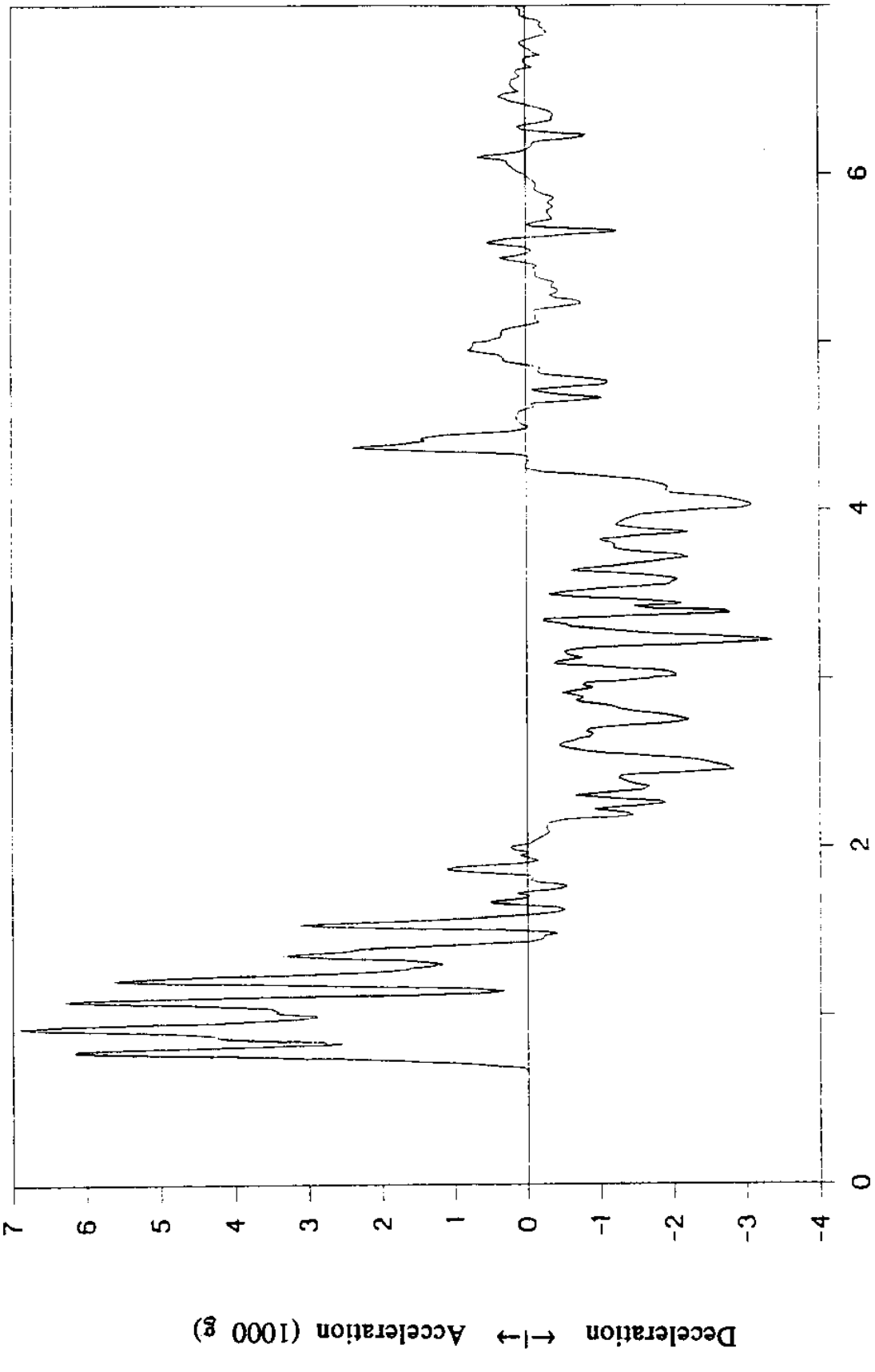

Figure 3.5a. Acceleration vs. Time Curve of the Second Test

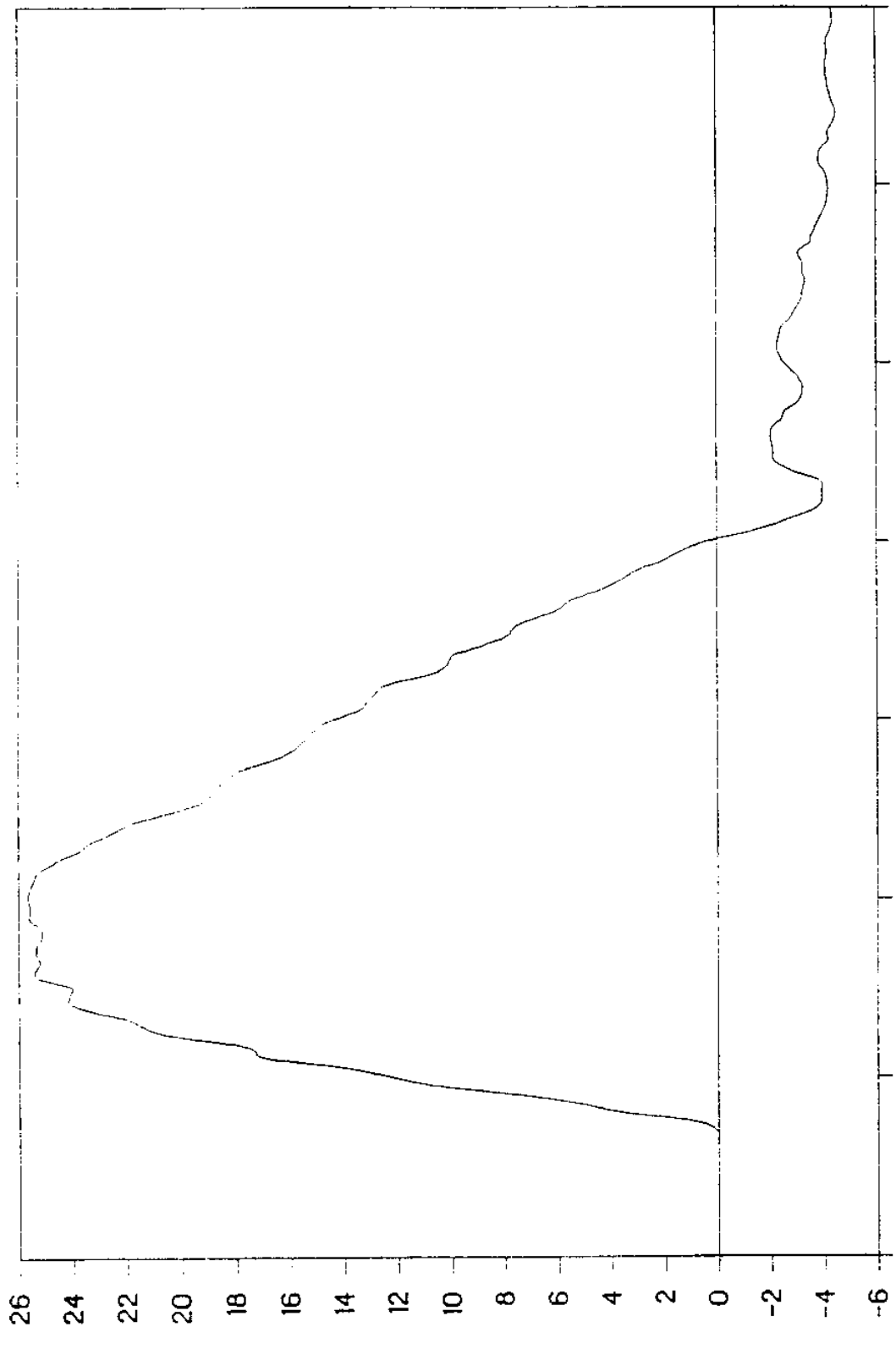

Figure 3.5b. Velocity vs. Time Curve of the Second Test

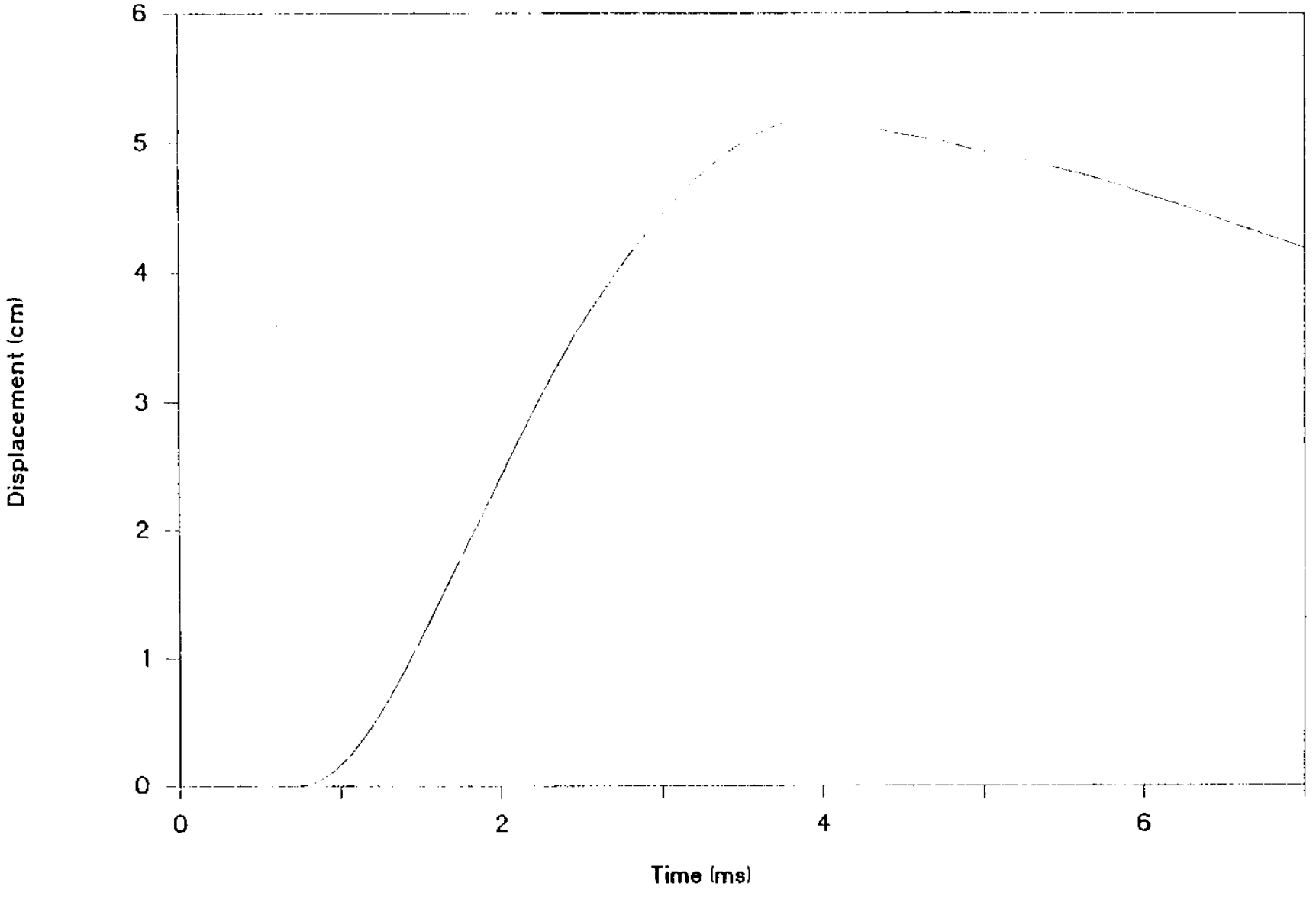

Figure 3.5c. Displacement vs. Time Curve of the Second Test

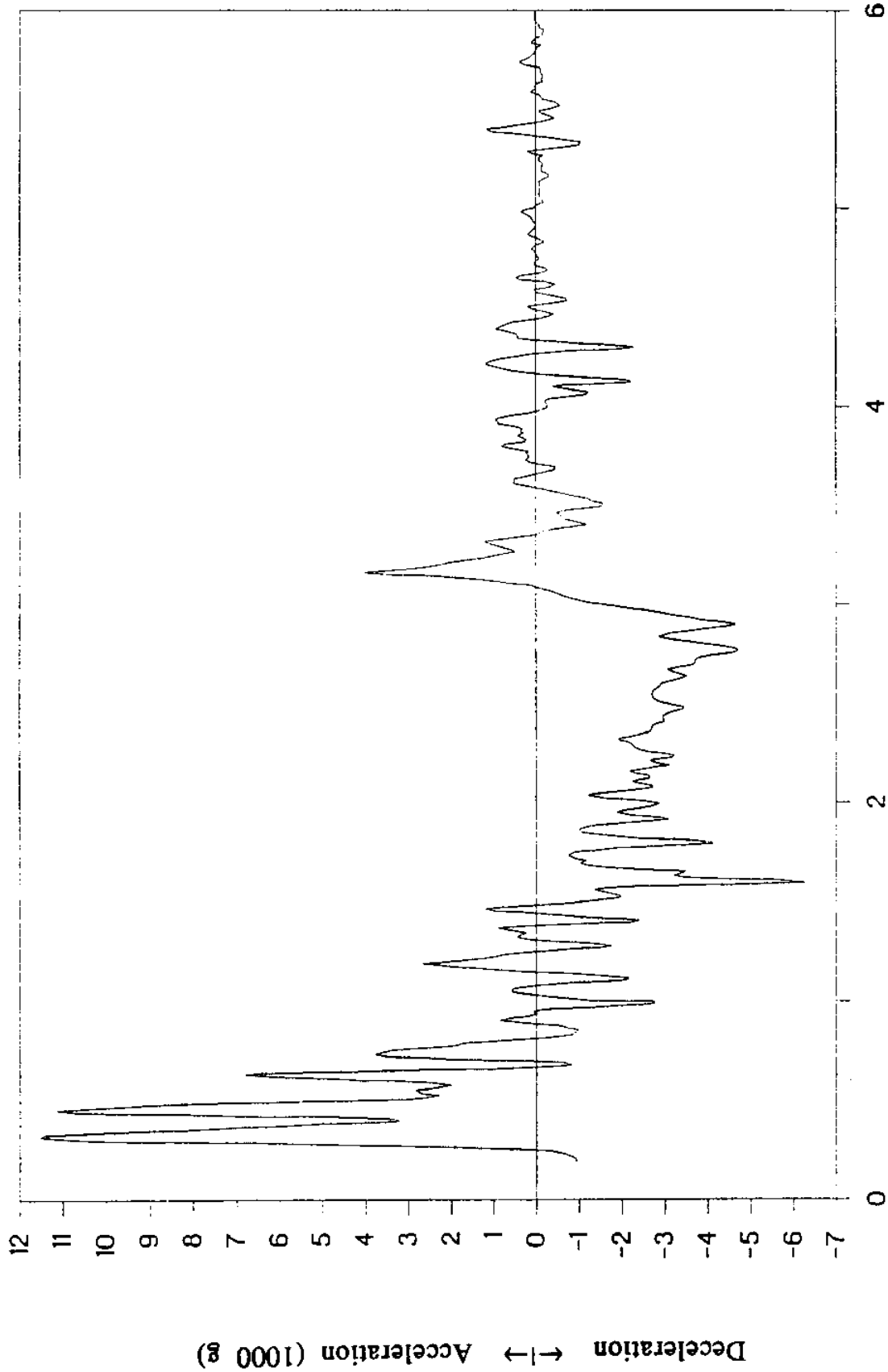

Figure 3.6a. Acceleration vs. Time Curve of the Third Test

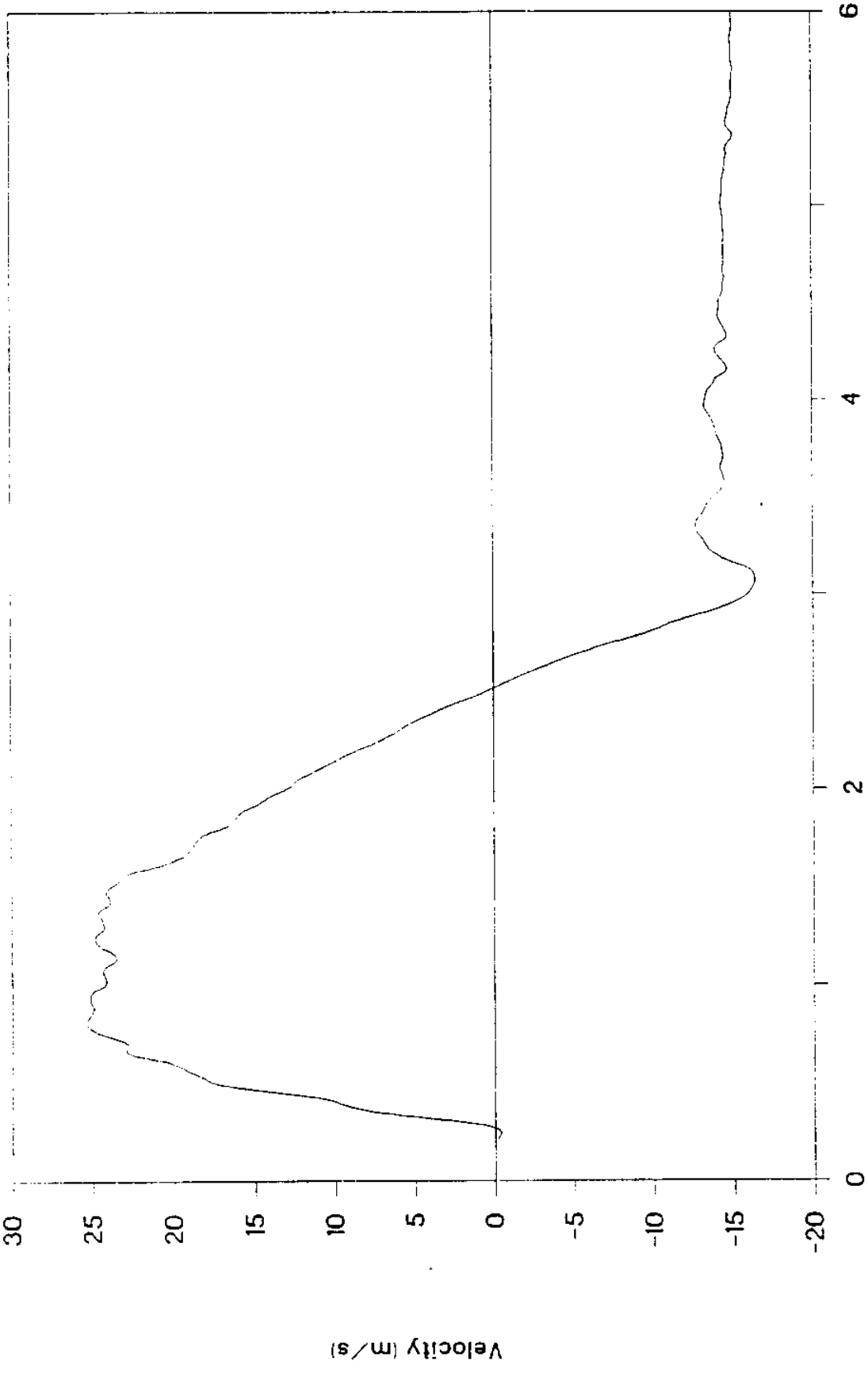

Figure 3.6b. Velocity vs. Time Curve of the Third Test

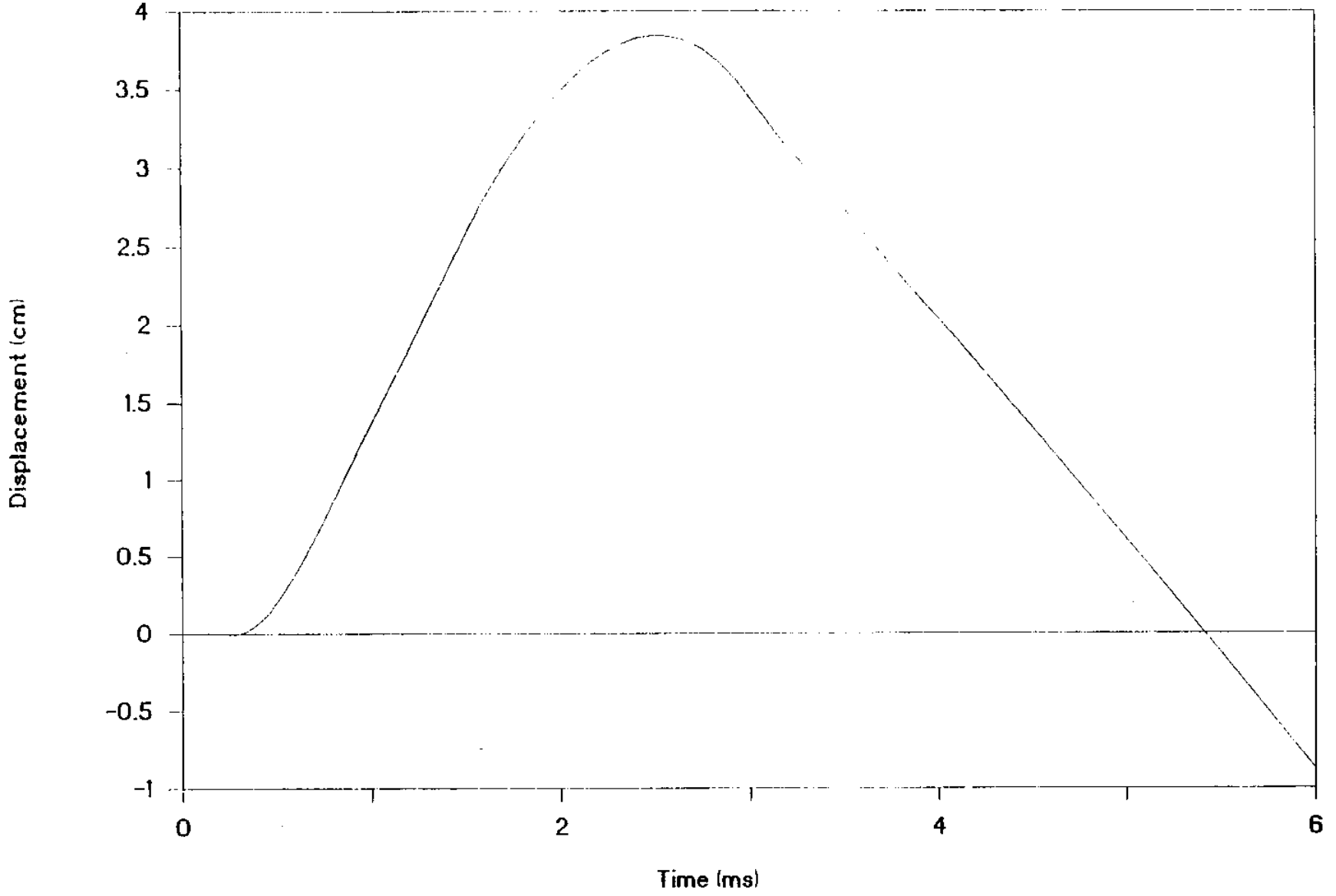

Figure 3.6c. Displacement vs. Time Curve of the Third Test

CHAPTER 4
MODELLING OF PENETRATION INTO BRITTLE DISCONTINUA

During the first phase of the MIT work on PEA (Einstein et al., 1987) we showed that no penetration or pullout models existed for brittle discontinua. Shallow penetration into brittle continua is satisfactorily modelled, but for deep penetration into brittle continua, only approximations existed. For ductile media there are a number of comprehensive numerical solutions which suffer, however, from the fact that many parameters cannot be determined in standard tests and that the sophistication is pushed too far compared to the variability of ground conditions. Simpler models such as the cavity expansion method cannot predict the entire stress field which is needed for estimation of effects ahead of the penetrator tip and for pullout resistance modelling. Also, a number of empirical approaches for deep penetration into earthen or other materials exist, they are based on "soil constants" or similar empirical factors which are not easily relatable to standard material characteristics. The strain path method, inspite of its simplification, seemed to be a promising tool for penetration and pullout prediction because of its capability to predict the entire stess field. At the time of the 1987 report, only solutions for incompressible frictionless materials but no solution for frictional and compressible materials existed, a situation that has been changed in the meantime. At the conclusion of the 1987 work (see Einstein et al. 1987), we decided to proceed as follows:

- Further develop the strain path method such that it can predict the entire stress field in ductile non-frictional and frictional, incompressible and compressible materials.
- Gain an understanding of what goes on when a PEA penetrates a brittle discontinuum and is pulled out from it.
- Combine the MIT jointed rock model with the strain path method, using the understanding of PEA penetration into brittle discontinuum, and construct a penetration-pullout prediction model for brittle discontinua.

The physical understanding of PEA penetration into brittle discontinua was gained in the initial test series (see Einstein and Jeng, 1988 and Chapter 2 of this report). Modelling, using the strain path method, was started in 1989 and is reported in the following chapters 5 and 6.

As stated above, the first step in developing strain path based models is to complete the models for ductile materials. The original model is for incompressible frictionless materials (clays) and was developed by Baligh (1985 a,b). This model allows one to determine the entire strain and stress field for deep penetration. In research parallel to the PEA work, a strain path based model for incompressible and compressible frictional materials was developed by Elghaib (1989). This model is, however, restricted to stress prediction for the centerline ahead of a penetrator in deep penetration. Both the original and the newer version of the strain path models do not consider any effects of the free surface.

Our approach in completing the ductile (strain path based) penetration prediction models is thus to first develop solutions for the entire stress field in frictional incompressible and compressible materials. This will be followed by consideration of free surface effects and, possibly, strain rate and inertia effects. Chapter 5 presents the work done so far on the predictions of the entire stress field for frictional incompressible materials.

It seemed useful to pursue, in parallel to the work reported in Chapter 5, direct depth prediction for rapid penetration using the strain path method. Clearly the stress field work will eventually result in prediction methods for penetration depth, also. The direct modelling is simpler and can, therefore, be more quickly completed. This allows us to compare penetration depth predictions based on the strain path method with observed results. If the comparison is satisfactory, it will indicate that the strain path method provides a good basis for rapid penetration problems for which it was so far not used. Naturally, the penetration depth prediction method is also useful by itself. In Chapter 6 we report on work in this area which has resulted in penetration depth prediction methods for

incompressible non-frictional (clay) and incompressible frictional (sand) materials.

CHAPTER 5
MODELING THE STRESS FIELD

5.1 Introduction

Knowledge of the stress field induced in the target material due to penetration provides the following useful information:

1) It can be used to determine the elastic and plastic zones.

2) Stress contours map the stress distribution, which helps us to understand the stress history of a given point in the medium during the penetration process.

3) It provides the magnitude of the stresses acting on the shank of the penetrator, which is needed in calculating the penetration and pullout resistances.

4) Combined with the deformation field, the stress field can be used to calculate the amount of energy transferred into the target material at any given penetration depth. Thus, with the stress field, penetration depth can be predicted for any given impact velocity (or energy).

Stress field modeling is presented here in sequence from the simple to the complex. We start with the one-dimensional stress distributions in the region far behind the tip of the penetrator and along the centerline beyond the penetrator tip. This is followed by the model for the two-dimensional strain field induced by the so-called "simple pile" which in turn is the basis for the two-dimensional stress distribution model. The 1-D and 2-D stress distributions will be developed for different types of materials (e.g., von Mises, extended von Mises and Mohr-Coulomb). What is presented below is, however, subject to simplifications such as absence of free surface and incompressibility of the medium. Removal of these simplifications will be the subject of subsequent research.

5.2 One-Dimensional Stress Fields

The stress distribution in the plane which is perpendicular to the penetrator axis and far above the tip of the penetrator approaches a one-dimensional distribution in the radial direction

(The coordinate system is defined in Fig. 5.1.). Similarly, under the tip of the penetrator, along the centerline of penetration, stresses are one-dimensionally distributed along the axial direction. Essentially, these one-dimensional stress distributions in the radial and axial directions represent two special cases of the two dimensional stress distribution. The results from the one-dimensional closed-form analysis can be used to check the adequacy of the two-dimensional stress distribution computed by the Strain Path Method.

5.2.1 Stress Distribution Far Behind the Tip of the Penetrator

A. Strains

The strains in an incompressible isotropic medium induced by an expanding cylindrical cavity can be expressed as (Baligh 1975)

$$\begin{aligned} \varepsilon_r &= -\frac{1}{2}\ln\left(1-\frac{R^2}{r^2}\right) \\ \varepsilon_\theta &= \frac{1}{2}\ln\left(1-\frac{R^2}{r^2}\right) \\ \varepsilon_z &= \varepsilon_{rz} = 0 \end{aligned} \qquad (5.1)$$

where R is the radius of the cylindrical cavity and r is the radial distance from the axis of the cavity.

If the point in the medium is far from the cavity, the strains can be approximated by

$$\begin{aligned} \varepsilon_r &= \frac{1}{2}\frac{R^2}{r^2} \\ \varepsilon_\theta &= -\frac{1}{2}\frac{R^2}{r^2} \\ \varepsilon_z &= \varepsilon_{rz} = 0 \end{aligned} \qquad (5.2)$$

B. Stress in the Elastic Zone

The stresses at a point in the medium in the elastic zone, where Eq. 5.2 is applicable, can be expressed by using the linear elastic constitutive law:

$$\sigma_r = \sigma_0 + G(\frac{R}{r})^2$$
$$\sigma_\theta = \sigma_0 - G(\frac{R}{r})^2 \qquad (5.3)$$
$$\sigma_z = \sigma_0$$

where: σ_0: initial stress
G: shear modulus

C. Equilibrium

The equilibrium equation for the one-dimensional case (in the radial direction) is:

$$\frac{d\sigma_r}{dr} + \frac{\sigma_r - \sigma_\theta}{r} = 0 \qquad (5.4)$$

The equilibrium equation is satisfied by the stresses in Eq. 5.3. Note that these stresses have been determined using the approximate strains of Eq. 5.2. If the exact stresses (based on the exact strains, Eq. 5.1, are used) have been used, the equilibrium condition would not be satisfied. This indicates that in the elastic zone, the strains generated from the deformation field of a fluid satisfy the kinematic constraints but not the equilibrium equation. However, the magnitude of strains in the elastic zone are small and so is the difference between the exact strains and approximate strains. Hence, the error is not significant.

D. Stresses in the Plastic Zone

In the plastic zone, the stresses are determined through the use of the appropriate failure criterion for the material and additional constraints as will be shown below:

D-1 Von Mises Material

The von Mises failure criterion is

$$S^2 = k^2 \qquad (5.5)$$

where: S: second invariant of the deviatoric stresses
k: material constant

To satisfy the equilibrium equation which includes two independent variables (σ_r, σ_θ), in addition to Eq. 5.5, one more constraint is required. Drucker and Prager (1952) assumed that

$$\sigma_z = \frac{1}{2}(\sigma_r + \sigma_\theta) \tag{5.6}$$

within the plastic zone for an incompressible material.
Substituting Eq. 5.5 and 5.6 into Eq. 5.4, the equilibrium equation can be solved and results in:

$$\frac{d\sigma_r}{dr} = \frac{-2k}{r} \tag{5.4b}$$

Integrating Eq. 5.4b, the stresses are:

$$\begin{aligned} \sigma_r &= \sigma_0 + k[1 + 2\ln(\frac{r_p}{r})] \\ \sigma_\theta &= \sigma_0 + k[-1 + 2\ln(\frac{r_p}{r})] \\ \sigma_z &= \sigma_0 + 2\ln(\frac{r_p}{r}) \end{aligned} \tag{5.7}$$

where r_p is the radius of the elastic-plastic boundary.

Rather than using Eq. 5.6 to obtain the stress distribution, another approach is possible. For example, if the associated flow rule is assumed, the increment of deviatoric stress tensor, dS_{ij}, can be expressed as

$$dS_{ij} = C_{ijkl}^{ep}\, de_{kl}$$

where: de_{kl} is the increment of the deviatoric strain tensor and C_{ijkl}^{ep} is the compliance tensor obtained from the flow rule

As will be shown later, dS_{ij} can be directly substituted into the equilibrium equation to solve for the stress field.

D-2 Frictional Material (Extended Von Mises with Cohesion Intercept)

The failure criterion of an extended von Mises material with a cohesion intercept is

$$S^2 = \bar{k}^2(\sigma + c\cot\phi)^2 \tag{5.8}$$

where σ is the octahedral stress, $\bar{k}$ is a material constant, c is the cohesion and ϕ is the frictional angle of the material.

To determine the stress distribution in the plastic zone, the approach of Section D-1 can be applied. Substituting Eq. 5.8 and 5.6 into Eq. 5.4, the equilibrium equation is given by:

$$\frac{d\sigma_r}{dr} = \frac{1}{r}\left(\frac{-2\bar{k}}{1+\bar{k}}\right)(\sigma_r + c\cot\phi) \tag{5.9}$$

Integrating Eq. 5.9, the stresses are solved:

$$\begin{aligned}
\sigma_r &= (\sigma_p + c\cot\phi)\left(\frac{r_p}{r}\right)^{\chi} - c\cot\phi \\
\sigma_\theta &= \left(\frac{1-\bar{k}}{1+\bar{k}}\right)(\sigma_p + c\cot\phi)\left(\frac{r_p}{r}\right)^{\chi} - c\cot\phi \\
\sigma_z &= \left(\frac{1}{1+\bar{k}}\right)(\sigma_p + c\cot\phi)\left(\frac{r_p}{r}\right)^{\chi} - c\cot\phi
\end{aligned} \tag{5.10}$$

where: $\sigma_p = (1+\bar{k})\sigma_0 + \bar{k}c\cot\phi$ is the radial stress at the elastic-plastic boundary and

$\chi = \dfrac{2\bar{k}}{1+\bar{k}}$ is a material-dependent constant.

D-3 Frictional Material (Mohr-Coulomb Criterion)

The failure criterion of a Mohr-Coulomb material is:

$$\sigma_1 = \frac{2c\cos\phi}{1-\sin\phi} + \frac{1+\sin\phi}{1-\sin\phi}\sigma_3 \qquad (5.11)$$

where σ_1 is the maximum principal stress (compressive stresses are positive) and σ_3 is the minimum principal stress.

The stress distribution in the elastic zone is characterized by the following relationships:

$$\sigma_1 = \sigma_r$$
$$\sigma_3 = \sigma_\theta$$

Substituting Eq. 5.6 and 5.11 into Eq. 5.4, the equilibrium equation becomes:

$$\frac{d\sigma_r}{dr} = \frac{1}{r}\left[\frac{-2\sin\phi}{1+\sin\phi}\sigma_r - \frac{2c\cos\phi}{1+\sin\phi}\right] \qquad (5.12)$$

Integrating equation 5.12 results in the stress distributions in the plastic zone of a Mohr-Coulomb material:

$$\sigma_r = (\sigma_p + c\cot\phi)\left(\frac{r_p}{r}\right)^A - c\cot\phi$$
$$\sigma_\theta = \frac{1-\sin\phi}{1+\sin\phi}(\sigma_p + c\cot\phi)\left(\frac{r_p}{r}\right)^A - c\cot\phi \qquad (5.13)$$
$$\sigma_z = \frac{1}{1+\sin\phi}(\sigma_p + c\cot\phi)\left(\frac{r_p}{r}\right)^A - c\cot\phi$$

where σ_p is the radial stress at elastic-plastic boundary and

$$\sigma_p = (1+\sin\phi)\sigma_0 + c\cos\phi$$
$$A = \left(\frac{2\sin\phi}{1+\sin\phi}\right)$$

The radial stresses, σ_r, for the different types of materials considered are listed in Table 5.1. The normalized radial stress vs. radial distance is shown in Fig. 5.2. As shown in Fig. 5.2, the radial

stress increases significantly close to the shank of penetrator and reaches a finite value along the shank of the penetrator.

5.2.2 Stress Distribution Along the Centerline beyond the Penetrator Tip

A. Strains

Along the center line, the material beyond the penetrator tip is subjected to triaxial compression; the strain components are

$$\begin{aligned} \varepsilon_r &= \frac{1}{2}\ln\left(1-\frac{R^2}{4z^2}\right) \\ \varepsilon_\theta &= \frac{1}{2}\ln\left(1-\frac{R^2}{4z^2}\right) \\ \varepsilon_z &= -\ln\left(1-\frac{R^2}{4z^2}\right) \end{aligned} \qquad (5.14a)$$

or, according to the definitions by Baligh (1985a), they can be expressed as:

$$\begin{aligned} E_1 &= \varepsilon_z = -\ln\left(1-\frac{R^2}{4z^2}\right) \\ E_2 &= \frac{1}{\sqrt{3}}(\varepsilon_r - \varepsilon_\theta) = 0 \\ E_3 &= \frac{2}{\sqrt{3}}\varepsilon_{rz} = 0 \end{aligned} \qquad (5.14b)$$

The E's are parameters used in soil mechanics to indicate the shearing modes under various types of loading conditions (specifically, E_1 for the conventional triaxial test, E_2 for the pressuremeter test and E_3 for the simple shear test; see also Appendix C.1.2).

B. Stresses in the Elastic Zone

The stress field in the elastic zone can be obtained following the same procedure as described in Section 5.2.1.

C. Equilibrium

Along the centerline, beyond the tip of the penetrator, the equilibrium equation reduces to (in terms of the deviatoric stresses, S_{ij} and the octahedral stress, σ):

$$\frac{d\sigma}{dz} = -\frac{\partial S_z}{\partial z} - \frac{S_{rz}}{r} - \frac{\partial S_{rz}}{\partial r} \qquad (5.15a)$$

Eq. 5.15a can be further reduced to

$$\frac{d\sigma}{dz} = -\frac{2}{\sqrt{3}}\left(\frac{1}{\sqrt{3}}\frac{dS_1}{dz} + \frac{S_3}{r}\right) \qquad (5.15b)$$

where

$$\begin{aligned} S_1 &= \sigma_z - \frac{1}{2}(\sigma_r + \sigma_\theta) \\ S_2 &= \frac{\sqrt{3}}{2}(\sigma_r - \sigma_\theta) \\ S_3 &= \sqrt{3}\sigma_{rz} \end{aligned} \qquad (5.15c)$$

according to the definitions by Baligh (1985a). The S's indicate the shearing modes for various types of loading conditions corresponding to the E's defined in Sec. 5.2.2.A.

D. Stresses in the Plastic Zone

D-1 Von Mises Material

In the plastic zone, the term S_3/r can be approximated by (Elghaib, 1989):

$$\frac{S_3}{r} = \frac{3k}{z}\left(\frac{2}{2 + \left(\frac{z}{z_p}\right)^2}\right) \qquad (5.16)$$

where z_p is the distance to the elastic-plastic boundary along the centerline.

In the plastic zone, S_1 is related to the strength parameter k

$$S_1 = \sqrt{3}k \qquad (5.17)$$

Since S_1 is not a function of z but a constant, the gradient dS_1/dz in Eq. 5.15b equals zero along the center line.
Using Eq. 5.16 and 5.17, Eq. 5.15b reduces to:

$$\frac{d\sigma}{dz} = -\frac{4\sqrt{3}}{2+\left(\frac{z}{z_p}\right)^2}\frac{k}{z} \tag{5.18}$$

The integration of Eq. 5.18 yields the octahedral stress distribution along the axial direction:

$$\sigma = \sigma_p + \sqrt{3}\ln\left[\frac{1}{3}+\frac{2}{3}\left(\frac{z_p}{z}\right)^2\right] \tag{5.19}$$

where σ_p is the octahedral stress at the elastic-plastic boundary.

D-2 Frictional Material (Extended Von Mises Material)

The failure criterion for the extended von Mises material is:

$$S = \bar{k}\sigma \tag{5.20}$$

where $\bar{k}$ is a material constant.
$\bar{k}$ can be determined in terms of friction angle, ϕ, measured in triaxial compression, by equating the von Mises criterion with the Mohr-Coulomb failure criterion. This leads to the following relationship:

$$\bar{k} = 2\sqrt{3}\frac{\sin\phi}{3-\sin\phi} \tag{5.21}$$

The von Mises criterion (which defines the shear strength of the material) is based on a constant, k, which does not depend on the octahedral stress. However, as shown in Eq. 5.20, for the extended von Mises material, the strength is proportional to the octahedral stress. If the constant k in the von Mises criterion (Eq. 5.5) is

replaced by $\bar{k}\sigma$, the von Mises criterion becomes the extended von Mises criterion. In other words, the extended von Mises criterion has a "shear strength", k, which depends on the octahedral stress state. Therefore, the stress distribution for the extended von Mises material can be solved by replacing the shear strength, k, in Eq. 5.18 by $\bar{k}\sigma$ and combining Eq. 5.21 with Eq. 5.18. This results in the equilibrium equation for the extended von Mises material:

$$\frac{d\sigma}{dz} = \frac{-4\sin\phi}{3(1+\sin\phi)} \frac{6}{\left(2+\left(\frac{z}{z_p}\right)^2\right)z}\sigma \qquad (5.22)$$

Integration of Eq. 5.22 yields the distribution of σ in the plastic zone:

$$\sigma = \sigma_0\left[\frac{1}{3}+\frac{2}{3}\left(\frac{z_p}{z}\right)^2\right]^{\chi} \qquad (5.23)$$

where:

$$\chi = \frac{2\sin\phi}{1+\sin\phi}$$

Figure 5.3 shows the octahedral stress distribution along the center line for the extended von Mises material. As can be seen in Fig. 5.3, the octahedral stress reaches a finite value at the tip of the simple pile.

5.3 The Two-Dimensional Stress Field

The Strain Path Method (Baligh, 1985a) is used to obtain the two-dimensional stress field. This is done because according to Baligh (1985a):

1) No realistic and rational methods are available to study the problems associated with deep penetration.

2) The SPM is an approximate analytic technique, which provides a comprehensive approach to penetration problems in a realistic, systematic and rational manner.

5.3.1 The Strain Path Method Approach

In the Strain Path Method, the deformation field induced in the target material by the penetrator is simulated by the deformation field induced in a fluid induced by a two-dimensional penetrator-shaped cavity. For example, a single source in a uniform flow field produces a penetrator-shaped cavity called the "simple pile" within the uniform flow field as shown in Fig. 5.1. The SPM is based on the assumption that, due to the severe kinematic constraints related to the deep penetration problem, deformations and strains are independent of the shearing resistance of the material. This assumption is based on the observations of ground deformations caused by deep penetration of rough objects (Baligh, 1975). Deep penetration problems are therefore considered to be a strain-controlled problem.

Using the Strain Path Method, the stress field is found as follows:

1) Obtain the strain field.
2) Determine the stress field in the elastic zone (by using a linear elastic, isotropic constitutive law).
3) Determine the deviatoric stress field in the plastic zone (by assuming a failure criterion and a flow rule).
4) Determine the octahedral stress field in the plastic zone on the basis of equilibrium.
5) Generate the stress field within the plastic zone by using the results of steps 3 and 4. Combined with the results of step 2, the entire stress field is obtained.

5.3.2 The Two-Dimensional Strain Field and Equilibrium Equations

A. Strains

The shape of the penetrator considered here is a cylindrical penetrator with a blunt tip, the so-called "simple pile" (see Appendix C.1). A single (point) source in a uniform flow field (in an incompressible, non-viscous fluid) produces a penetrator-shaped cavity in the flow field as shown in Fig. 5.1. The closed form solutions for the strain field induced by a simple pile are found to be (Teh 1987):

$$\varepsilon_r = F_1(\phi) + (1 - \frac{3}{2}B^2)F_2(\phi)$$
$$\varepsilon_z = -F_1(\phi) - (1 - \frac{3}{2}B^2)F_2(\phi)$$
$$\varepsilon_\theta = -\frac{1}{2}F_2(\phi)$$
$$\varepsilon_{rz} = -\frac{1}{2}\left\{(2B^2 - 1)\frac{\pi - \phi}{2} + B\sin\phi - \frac{1}{4}\sin 2\phi - 2B(B^2 - 1)\tan^{-1}\left[\left(\frac{B+1}{B-1}\right)^{0.5}\cot\frac{\phi}{2}\right]\right\}$$

(5.24)

where

$$F_1(\phi) = 3(1 + \cos\phi)\left[\left(\frac{r_0}{R}\right)^2 + \frac{3}{4} - \frac{\cos\phi}{4}\right]$$
$$F_2(\phi) = \ln\left[1 + \frac{1}{2}\left(\frac{R}{r_0}\right)^2(1 + \cos\phi)\right]$$
$$B = 2\left(\frac{r_0}{R}\right)^2 + 1$$

Equation 5.24 describes the strains in a streamline with an initial distance r_0 from the centerline as a function of ϕ. The geometries of the simple pile and the streamline are defined in Fig. 5.1. As shown in Eq. 5.24 the volumetric strain is always zero in the entire field due to the constraint that the material is incompressible. Hence, the strain components shown in Eq. 5.24 are also the deviatoric strain components (e_r, e_z, e_θ, e_{rz}). The strains approach infinity at the tip and shank of the penetrator.

For a point which is far from the simple pile, the two-dimensional strain field can be approximated by (Baligh, 1985a):

$$\varepsilon_r = \left(\frac{R}{2r}\right)^2(1 + \cos\phi + \cos\phi\sin^2\phi)$$
$$\varepsilon_z = \left(\frac{R}{2r}\right)^2(-\cos\phi\sin^2\phi)$$
$$\varepsilon_\theta = \left(\frac{R}{2r}\right)^2(-1 - \cos\phi)$$
$$\varepsilon_{rz} = \left(\frac{R}{2r}\right)^2(-\sin^3\phi)$$

(5.25)

where R: radius of simple pile

r: radial distance of a point from the center line.

B. Equilibrium

The equilibrium equation in the axisymmetric case can be expressed in terms of the octahedral stress (σ) and the deviatoric stresses (S_r, S_z, S_θ and S_{rz}), which is convenient for the subsequent steps in the analysis.

$$\frac{\partial \sigma}{\partial r} = -\frac{\partial S_r}{\partial r} - \frac{\partial S_{rz}}{\partial z} - \frac{S_r - S_\theta}{r}$$
$$\frac{\partial \sigma}{\partial z} = -\frac{\partial S_{rz}}{\partial r} - \frac{\partial S_{rz}}{\partial z} - \frac{S_{rz}}{r} \qquad (5.26)$$

5.3.3 Determination of the Stress Field

A. Stresses in the Elastic Zone

In the elastic zone, the stress at any point can be determined from the strains and the elastic constitutive relation. For example, for a linear elastic, isotropic material, the stresses can be expressed as:

$$\sigma_{ij} = \lambda \varepsilon_{kk} \delta_{ij} + 2\mu \varepsilon_{ij} \qquad (5.27a)$$

where:

σ_{ij}: stress tensor (i, j= 1, 2 and 3)
ε_{ij}, ε_{kk}: strain tensor, volumetric strain
λ, μ: Lame's constants.

In the axisymmetric case, the stresses can be expressed in the following form:

$$\begin{bmatrix} \sigma_r \\ \sigma_z \\ \sigma_\theta \\ \sigma_{rz} \end{bmatrix} = \frac{E}{(1+\nu)(1-2\nu)} \begin{bmatrix} 1-\nu & \nu & \nu & 0 \\ \nu & 1-\nu & \nu & 0 \\ \nu & \nu & 1-\nu & 0 \\ 0 & 0 & 0 & 1-2\nu \end{bmatrix} \begin{bmatrix} \varepsilon_r \\ \varepsilon_z \\ \varepsilon_\theta \\ \varepsilon_{rz} \end{bmatrix} \qquad (5.27b)$$

where E is the Young's modulus and v is the Poisson's ratio.

B. Stresses in the Plastic Zone

B-1 Von Mises Material

The failure criterion for the von Mises material is

$$S^2=k^2 \qquad (5.5)$$

where S^2: second invariant of the deviatoric stress.
To solve the equilibrium equation (5.26) which has four independent variables (S_r, S_z, S_θ, S_{rz}), three more constraints or assumptions in addition to Eq. 5.5 are required. A simpler approach to obtain the two-dimensional stress field is to use the plastic flow rule. For instance, the incremental stress-strain relationship derived by assuming an associated flow rule for a von Mises material is given by (Desai and Siriwardane, 1984):

$$d\sigma_{ij} = (2Gde_{ij} + KdI_1 de_{ij}) - G\frac{S_{mn}de_{mn}}{k^2}S_{ij} \qquad (5.28a)$$

where:
- G: shear modulus
- K: bulk modulus
- de_{ij}: increments of the deviatoric strain tensor
- S_{ij}: the deviatoric stress tensor
- k: material constant of the von Mises material
- dI_1: increment of volumetric strain

Equation 5.28a describes the increments of stresses as a function of a given set of strain increments. Since the volumetric strain equals zero anywhere within the deformed field, as mentioned in Section 5.3.2.A, Eq. 5.28a can be solved as

$$\begin{Bmatrix} dS_r \\ dS_\theta \\ dS_z \\ dS_{rz} \end{Bmatrix} = G\left\{\begin{bmatrix} 2 & 0 & 0 & 0 \\ 0 & 2 & 0 & 0 \\ 0 & 0 & 2 & 0 \\ 0 & 0 & 0 & 2 \end{bmatrix} - \frac{1}{k^2}\begin{bmatrix} S_rS_r & S_rS_\theta & S_rS_z & 2S_rS_{rz} \\ S_\theta S_r & S_\theta S_\theta & S_\theta S_z & 2S_\theta S_{rz} \\ S_zS_r & S_zS_\theta & S_zS_z & 2S_zS_{rz} \\ S_{rz}S_r & S_{rz}S_\theta & S_{rz}S_z & 2S_{rz}S_{rz} \end{bmatrix}\right\}\begin{Bmatrix} de_r \\ de_\theta \\ de_z \\ de_{rz} \end{Bmatrix} \qquad (5.28b)$$

The above equation yields the increments of the deviatoric stresses when the deviatoric strains are given by Eq. 5.24. The deviatoric stress field is obtained by integrating Eq. 5.28b; this is followed by the determination of the deviatoric stress gradients. They, in turn, are substituted into Eq. 5.26 to solve for the gradients of the octahedral stress. Using Eq. 5.26, the increments of the octahedral stress, $d\sigma$, can be expressed in terms of the gradients of the deviatoric stresses:

$$\begin{aligned} d\sigma &= \frac{\partial \sigma}{\partial r}dr + \frac{\partial \sigma}{\partial z}dz \\ &= -\left(\frac{\partial S_r}{\partial r} + \frac{\partial S_{rz}}{\partial z} + \frac{S_r - S_\theta}{r}\right)dr - \left(\frac{\partial S_{rz}}{\partial r} + \frac{\partial S_z}{\partial z} + \frac{S_{rz}}{r}\right)dz \end{aligned} \tag{5.29a}$$

As shown in Eq. 5.29a, the octahedral stress is determined by the gradients of the deviatoric stresses. The deviatoric stresses according to Eq. 5.28b are determined by the increments of strains corresponding to the strain history (or strain path along a streamline). It is therefore necessary to integrate the deviatoric stresses along the streamline.

Once the deviatoric stress field is obtained, the octahedral stress can be determined from Eq. 5.29a. For example, the increments of the octahedral stress along a streamline can be expressed as follows by using Eq. 5.28b and 5.29a :

$$\begin{aligned} d\sigma = &\left(\frac{G}{k^2}S_r A - 2G de_r\right) + \left(\frac{G}{k^2}S_{rz}A - 2G de_{rz}\right)\frac{dr}{dz} - \left(\frac{S_r - S_\theta}{r}\right)\left(\frac{dr}{d\phi}\right)d\phi \\ &+ \left(\frac{G}{k^2}S_{rz}A - 2G de_{rz}\right)\frac{dz}{dr} + \left(\frac{G}{k^2}S_z A - 2G de_z\right) - \frac{S_{rz}}{r}\left(\frac{dz}{d\phi}\right)d\phi \end{aligned} \tag{5.29b}$$

where:

$$A = S_r de_r + S_\theta de_\theta + S_z de_z + 2S_{rz} de_{rz},$$

$$\frac{dr}{dz} = \left(\frac{dz}{dr}\right)^{-1} = \frac{\sin^3\phi}{\cos\phi(2 + \sin\phi) + 4\left(\frac{r_0}{R}\right)^2 + 2},$$

which is the gradient of the streamline

The stress field can be derived by combining Eq. 5.28b and 5.29b. The stress field for the von Mises material is shown in Fig. 5.4 (Baligh 1985a).

B-2 Frictional Material

The strength of the von Mises material is not a function of the octahedral stress. However, most geomaterials are c-ϕ materials, i.e., the strength of the ground is a function of the octahedral stress. Let us consider a simple case, where $S = k = \bar{k}\sigma$, as a starting point. $\bar{k}$ is a material constant which represents the internal friction of the material. As mentioned in the previous sections, the stress field of the frictional material can be determined by making the constant k in the von Mises criterion dependent on the octahedral stress in the deformed field.

A forward numerical scheme is developed to solve the stress field for the frictional material:

1) At the elastic-plastic boundary, let the initial k be equal to $\bar{k}\sigma_0$.
2) Compute the increments of the deviatoric strains for two points on a streamline.
3) Use Eq. 5.28b to get the increments of the deviatoric stresses.
4) Compute the spatial gradients of the deviatoric stresses.
5) Substitute the results from step 4 into Eq. 5.29a to obtain the increments of the octahedral stress at the next point.
6) Compute the octahedral stress at the next point.
7) Update the k value (Let $k = \bar{k}(\sigma + d\sigma)$).
8) Repeat steps 2 to 7 to get the entire stress field.

5.4 Further Research

The following issues have to be addressed in the next research phase:

1) Determine the stress field with models which can represent the mechanical properties of the ground better. An example is the extended von Mises criterion discussed above.
2) Examine the penetrator shape effect.

3) Obtain the penetration resistance from the stress field and predict the penetration depth with a given initial input energy (or impact energy). The penetration resistance can be evaluated by integrating the stresses acting on the surface of the penetrator at any given penetration depth. The penetration depth can also be determined by equating the input energy and the energy required to achieve a given penetration depth (this a rigorous solution; a simple solution will be presented in Chapter 6).

4) Obtain the pullout resistance using the stress field and interface shearing characteristics.

5) Introduce a free surface in the SPM approach. One of the limitations of SPM is that it assumes that penetration depth is great (approaching infinity) and that the effect of the free surface is negligible. To map the PEA problem better, a free surface can be generated by the superposition of a point source and its virtual image (see Sagaseta, 1987).

6) Extend the SPM approach to compressible materials in the two-dimensional case. Elghaib (1989) has already developed a SPM solution for the one-dimensional stress distribution along the centerline for a compressible, frictional material.

7) Most important will be the inclusion of the constitutive model for discontinuous brittle materials which realistically represents rock mass behavior.

Types of Material	Von Mises	Extended Von Mises	Extended Von Mises + Cohesion Intercept	Mohr-Coulomb	Mohr-Coulomb (ϕ=0)
Failure criterion	$S^2 = k^2$	$S^2 = \bar{k}^2\sigma^2$	$S^2 = \bar{k}^2(\sigma + c\cot\phi)^2$	$\sigma_r = \frac{2c\cos\phi}{1-\sin\phi} + \frac{1+\sin\phi}{1-\sin\phi}\sigma_\theta$	$\sigma_r = 2c + \sigma_\theta$
σ_r	$\sigma_p + 2k\ln\frac{r_p}{r}$	$\sigma_p\left(\frac{r_p}{r}\right)^{\frac{2k}{1+k}}$	$(\sigma_p + c\cot\phi)\left(\frac{r_p}{r}\right)^{\left(\frac{2\bar{k}}{1+\bar{k}}\right)} - c\cot\phi$	$(\sigma_p + c\cot\phi)\left(\frac{r_p}{r}\right)^{\frac{2\sin\phi}{1+\sin\phi}} - c\cot\phi$	$\sigma_p + 2c\ln\left(\frac{r_p}{r}\right)$
σ_p	$\sigma_0 + k$	$(1+\bar{k})\sigma_0$	$(1+\bar{k})\sigma_0 + \bar{k}c\cot\phi$	$(1+\sin\phi)\sigma_0 + c\cos\phi$	$\sigma_0 + c$
r_p	$\sqrt{\frac{G}{k}}R$	$\sqrt{\frac{G}{\bar{k}\sigma_0}}R$	$\left(\frac{G}{\bar{k}(\sigma_0 + c\cot\phi)}\right)^{\frac{1}{2}}R$	$\left(\frac{G}{\sin\phi(\sigma_0 + c\cot\phi)}\right)^{\frac{1}{2}}R$	$\sqrt{\frac{G}{c}}R$

Symbols:
S: second invariant of deviatoric stress
σ: octahedral stress
σ_r: radial stress
σ_p: radial stress at elastic-plastic boundary
R: radius of penetrator
k, $\bar{k}$: material constants
ϕ: friction angle
c: cohesion
r, r_p: radial distance, plastic boudary
G: shear modulus

Table 5.1. Summary of Radial Stress Distributions Far behind the Tip of the Penetrator for Various Types of Materials

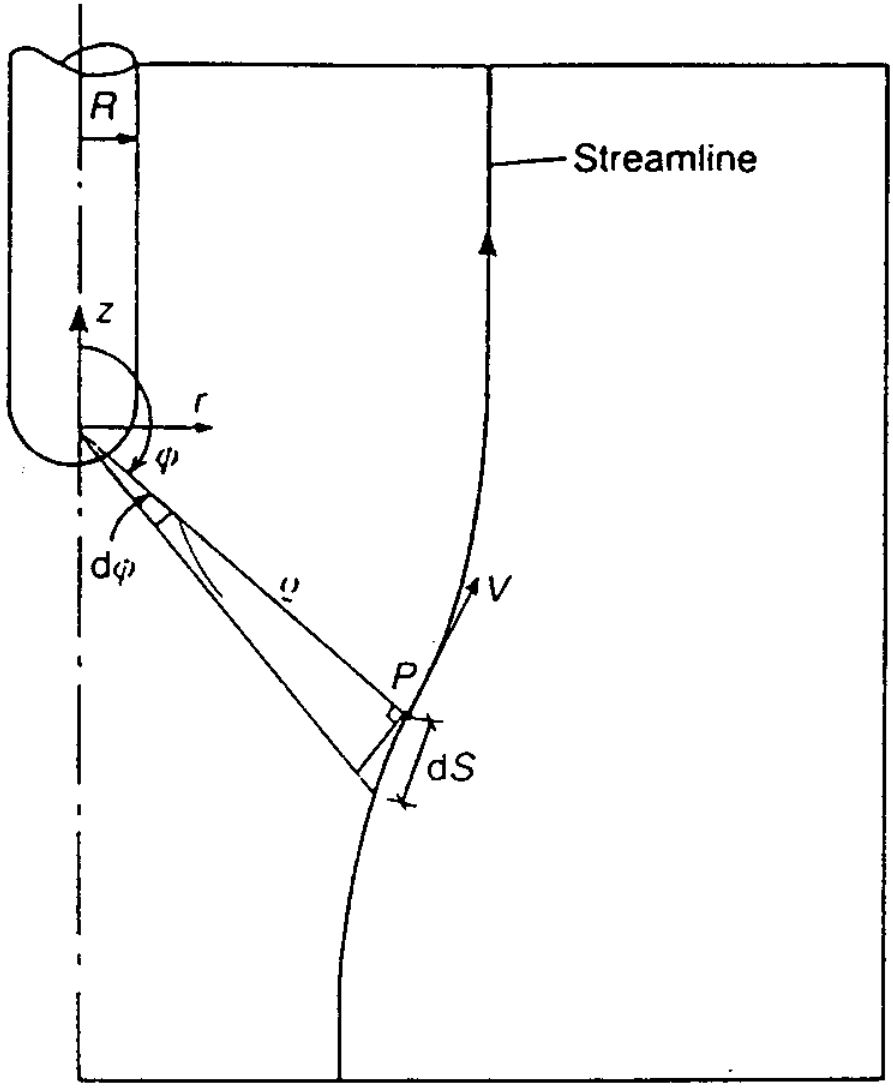

Figure 5.1. The Definition of the Coordinate System and Geometry of the Simple Pile and Stream Line (Baligh, 1985)

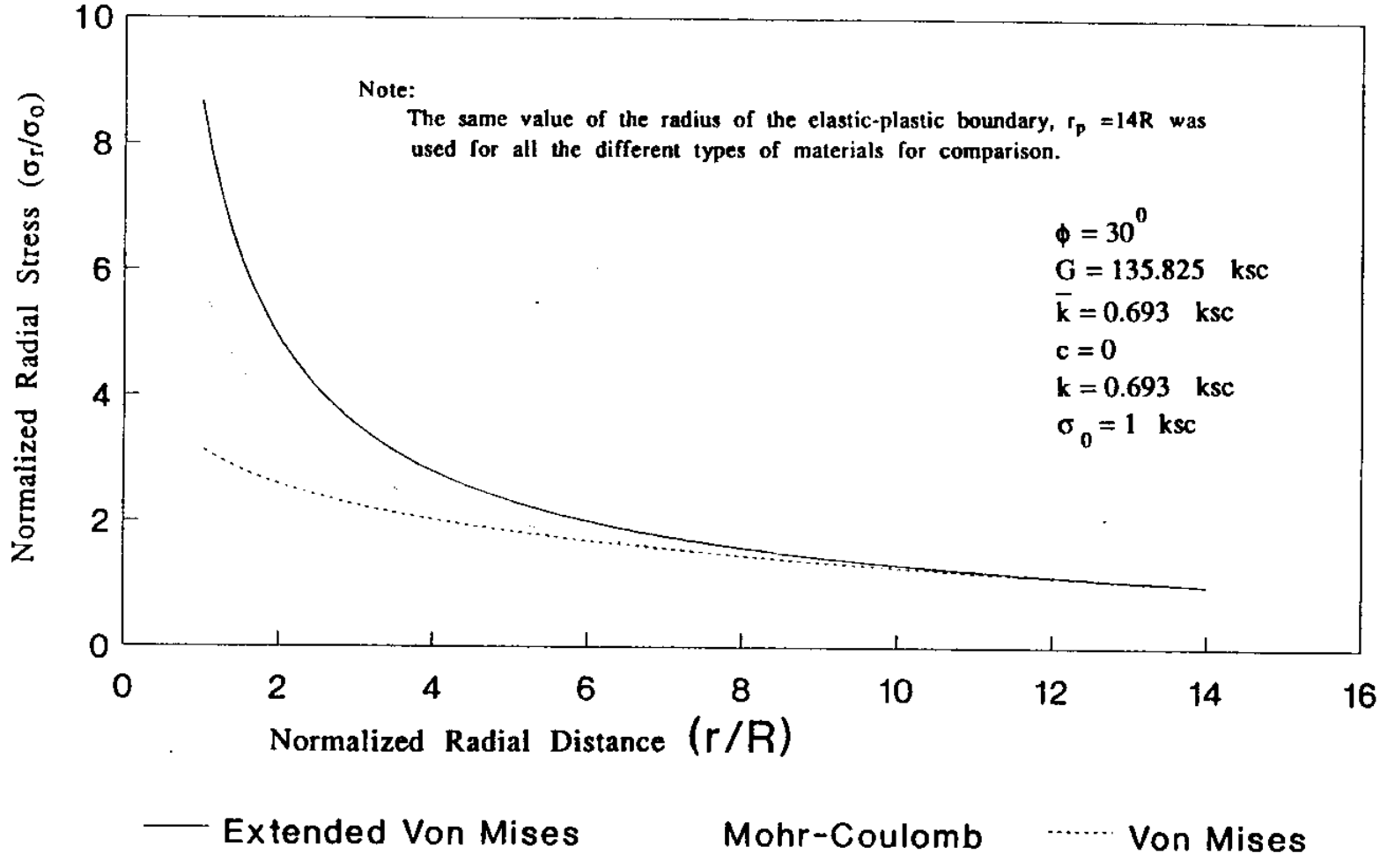

Figure 5.2. Radial Stress Distributions Far behind the Tip of the Penetrator for Various Types of Materials

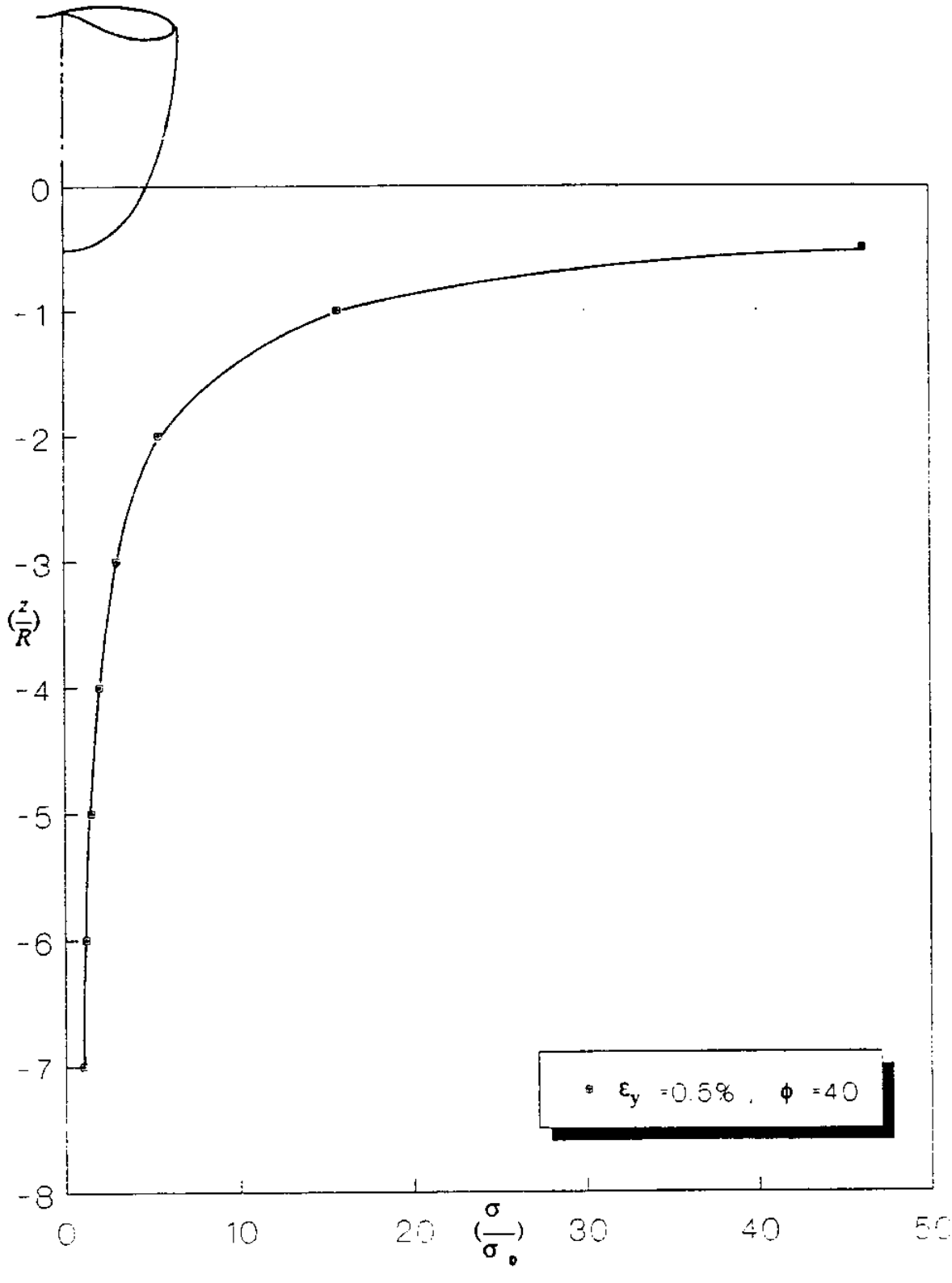

Figure 5.3. The Distribution of the Octahedral Stress along the Centerline beyond the Penetrator Tip for a Frictional Material (Elghaib, 1989)

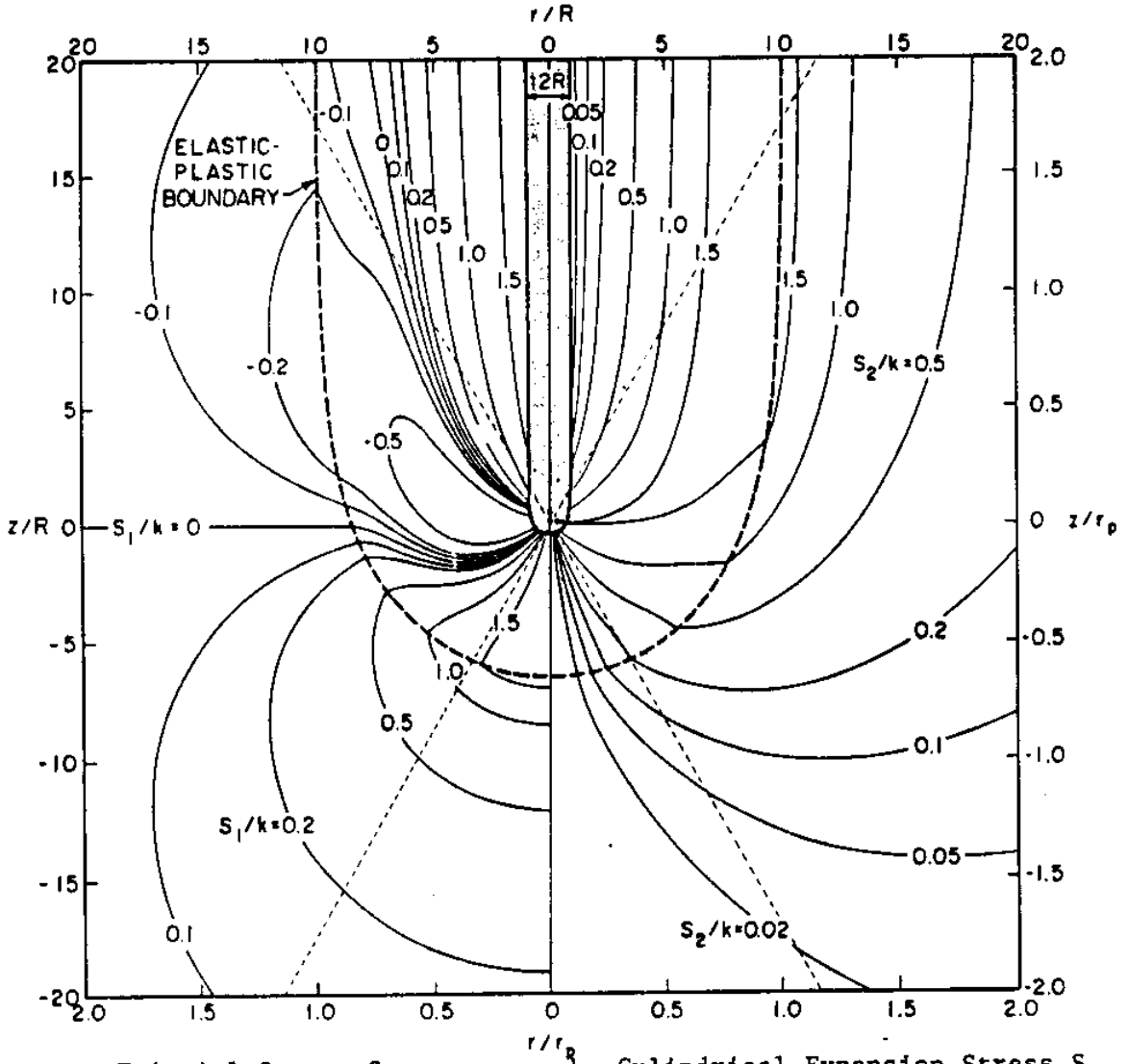

Figure 5.4. Deviatoric Stresses in a von Mises Material during Simple Pile Penetration (Baligh, 1985)

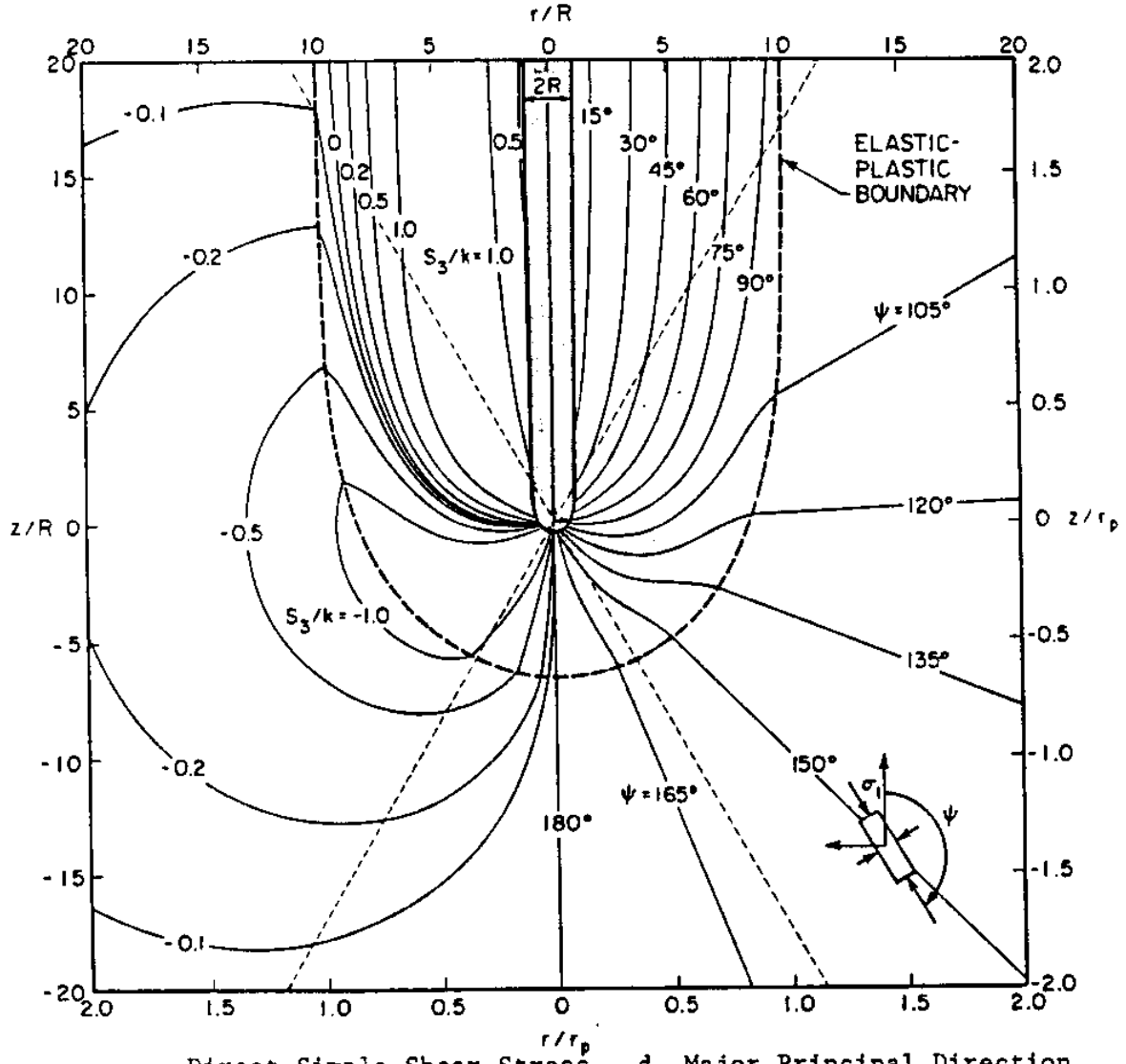

c. Direct Simple Shear Stress S_3 d. Major Principal Direction

Figure 5.4. Deviatoric Stresses in a von Mises Material during Simple Pile Penetration (Baligh, 1985)

CHAPTER 6
MODELING PENETRATION DEPTH

6.1 Introduction

Here we develop a simple analytical model for predicting impact penetration depth into clays and sands. This is based on the results of previous work on point resistance of the simple pile using the Strain Path Method (SPM). As will be seen, this approach requires only a few parameters which can be easily determined. Also, expressions to include friction and strain rate will be formulated in a similarly simple manner. The results obtained with the simple Strain Path-based approach will be compared to data from impact penetration tests. If the comparison shows satisfactory correspondence, it will not only tell us that we have a reasonable and simple approach to predict penetration depth but it will also indicate that the basic principles of the Strain Path Method are adequate to model the penetration process.

The total depth of penetration in an impact penetration problem may be solved by integrating the equation of motion of the penetrator:

$$F = ma = mv\frac{dv}{dz} \tag{6.1}$$

where: F = net force acting on the penetrator
m = mass of the penetrator
a = acceleration of the penetrator
v = velocity of the penetrator
z = depth of penetration

Thus, all the driving and resisting forces on the penetrator have to be identified and expressed in terms of the relevant parameters of the penetration problem. Forces resisting penetration include: bearing resistance of the ground (equal to the point resistance of the penetrator), skin friction between the penetrator surface and the ground, and inertial resistance of the ground. In the impact

penetration problem, the magnitude of the weight of the penetrator is small compared to the resisting forces. The driving force due to the weight of the penetrator may thus be neglected for practical purposes.

6.2 Point Resistance of the Simple Pile in Clays

Analytical expressions for the point resistance of the simple pile can be determined in two ways, by 1) energy considerations and 2) centerline analysis.

Baligh (1985) has applied the Strain Path Method to study deep, steady, undrained penetration in isotropic, homogeneous, incompressible cohesive ground (fully saturated clays). He used an elastic-perfectly plastic (bilinear) behavior obeying the von Mises yield criterion for the simple pile, a blunt indenter (for a detailed description of the Strain Path Method and the simple pile, see Appendix C.1). He derived an analytical expression for the point resistance q_{sp} of the simple pile from energy considerations. q_{sp} is defined as the upper bound force required to push the simple pile divided by its cross-sectional area, πR^2, R being the radius of the simple pile. In other words, q_{sp} is derived by assuming that the work done in pushing the pile is equal to the work done in overcoming the soil resistance due to initial stress, plastic flow and elasticity outside the plastic domain. Baligh gives an analytical expression of the form (Appendix C.2):

$$q_{sp} = N_{sp}\, k + \sigma_o \qquad (6.2)$$

where N_{sp} = simple pile point resistance factor (dimensionless) from energy considerations which depends on the octahedral yield strain E_y of the ground

$$N_{sp} = 1 + \sqrt{\frac{3}{4}}\left[\ln\left(\frac{3}{4}\right) - 2 - 4\ln E_y\right] \qquad (6.3)$$

$$E_y = \frac{1}{\sqrt{6}}\gamma_y \quad (\gamma_y = \text{engineering yield strain in the direct simple shear (DSS) test})$$

$$= \frac{1}{\sqrt{2}}\varepsilon_y \quad (\varepsilon_y = \text{axial yield strain in the triaxial compression (TC) test})$$

k = a measure of the undrained shear strength s_u of the soil

$= s_u(DSS) = s_u$ from DSS test

$= \frac{2}{\sqrt{3}} s_u(TC)$ ($s_u(TC) = s_u$ from TC test)

σ_o = initial isotropic stress in the ground

Fig. 6.1 shows N_{sp} values as a function of E_y for the bilinear model for $0.1\% < E_y < 10\%$. The values of N_{sp} are in the range 4-12. The figure indicates that for soils with larger yield strain, the point resistance factor is smaller. This is so because we get the same strain field for any incompressible ground. If the yield strain is larger then the plastic zone is smaller. Thus, less energy is required to deform the soil plastically.

Elghaib (1989) proposed a simplified method for evaluating the condition at the tip of the simple pile by considering that in the region ahead of the simple pile (see also Appendix C.1):

1. The dominant mode of shearing is triaxial compression.
2. The strain paths for elements approaching the pile tip involve monotonically changing strain rate and strain components.
3. Close to the pile centerline, there are only small gradients of the field variables in the radial direction; hence, realistic solutions can be obtained by considering only conditions of vertical equilibrium.

The above simplifications allow one to obtain closed-form solutions along the centerline for the simple pile geometry.

The point resistance q_c, assumed to be equal to the vertical stress at the tip of the simple pile, is given by (Appendix C.3)

$$q_c = N_c\, s_u(TC) + \sigma_o \qquad (6.4)$$

where N_c = point resistance factor from (one-dimensional) centerline analysis

$$N_c = 2\ln\left(\frac{1}{3} + \frac{2}{3}\frac{1}{E_y}\right) + \frac{4}{3} \qquad (6.5)$$

Fig. 6.2 shows N_c as a function of E_y for the bilinear model for $0.1\% < E_y < 10\%$. The values of N_c are in the range 5-15. These are in reasonable agreement with empirical cone resistance factors generally of a magnitude of 10-20.

Elghaib, comparing N_c with N_{sp} (Fig. 6.1) further noted that:

1. Predictions of tip resistance factors N_{sp} and N_c are qualitatively the same; for a given input parameter E_y, N_c is larger than N_{sp} by approximately 20%.
2. Predictions of point resistance q_c are approximately equal to those of q_{sp}. For example, for the bilinear model with $E_y = 2.0\%$

$N_c = 8.4$ $\qquad q_c - \sigma_o = N_c \frac{\sqrt{3}}{2} k = 7.3\ k$

$N_{sp} = 7.4$ $\qquad q_{sp} - \sigma_o = N_{sp}\, k = 7.2\ k$

The quantitative similarity of predicted point resistance using the centerline solution with the energy-based solution for the entire field suggests that the centerline solution can be used for describing the point resistance of the simple pile and for interpreting cone penetration tests. It should be noted however that this comparison was made for the case of simple, isotropic, elastic-perfectly plastic ground and an isotropic initial state of stress.

6.3 Point Resistance of the Simple Pile in Sands

Elghaib (1989) also developed a simple expression for point resistance based on centerline analysis of the simple pile for steady, deep, drained penetration in sands. He assumed that the sand is incompressible so that the strain field is identical to that for

undrained penetration in clay (he also developed a compressible solution which we are going to use later). The only difference is the constitutive model for the ground. For drained penetration, no excess pore pressure is generated in the ground and the behavior is modeled in terms of effective stresses. The ground is also described using a bilinear elastic-perfectly plastic model but failure (or yield) is described by an extended von Mises criterion expressed in terms of the friction angle ϕ' of the soil measured in triaxial compression.

The point resistance q_c', assumed to be equal to the vertical stress at the tip of the simple pile, is given by (see Appendix C.4)

$$q_c' = N_\sigma \sigma_o' \tag{6.6}$$

where N_σ = point resistance factor from centerline analysis which depends on the axial yield strain ε_y and the friction angle ϕ' of the soil

$$N_\sigma = \frac{3(1+\sin\phi')}{3-\sin\phi'}\left(\frac{1}{3}+\frac{2}{3}\frac{1}{\varepsilon_y}\right)\frac{2\sin\phi'}{1+\sin\phi'} \tag{6.7}$$

σ_o' = initial isotropic effective stress in the soil

Figures 6.3 and 6.4 show N_σ as a function of ϕ' and ε_y respectively, indicating that:

1. For a given friction angle ϕ', the point resistance N_σ decreases with increasing axial yield strain ε_y (or decreasing size of the plastic zone)
2. The point resistance N_σ can vary by a factor of 10 at a given friction angle ϕ' (Fig. 6.4) depending on the axial yield strain ε_y.
3. For a given yield strain ε_y, the point resistance N_σ increases with increasing friction angle ϕ'; N_σ changes by a factor of 4 when ϕ' varies in the range of interest (30° to 40°).

Elghaib has shown that his solution is bounded by Vesic's (1972) spherical cavity expansion, and Vesic's (1977) hybrid spherical cavity expansion with plastic bearing capacity failure, models. Elghaib's solution is approximately equal to the hybrid

model at low friction angles ϕ' (Fig. 6.5 for the case $\varepsilon_y = 0.7\%$). It has been shown that Vesic's basic cavity expansion solution underpredicts actual bearing capacity resistance whereas the hybrid solution gives values substantially closer to Belotti's experimental data on Ticino sand (Einstein et al 1987).

6.4 Penetration Depth Predictions in Clays

6.4.1 Basic Model (Point Resistance Only)

So far we have shown that the point resistance for the simple pile for undrained penetration in clays can be determined for deep, constant-velocity penetration and that it depends only on ground properties such as shear strength and yield strain. As a first approximation, let us assume that 1) the point resistance is the major contributor to the resistance of the penetrator, 2) the same expression for point resistance applies to the entire impact penetration process, i.e., starting at impact velocity at the free surface of the ground until the penetrator comes to rest and 3) the simple pile geometry is adequate to represent general penetrator tip shapes.

Therefore, using the point resistance based on the entire strain field using energy considerations (Eq. 6.2) and substituting in the equation of motion (Eq. 6.1), we have

$$-\int_o^z (N_{sp}k + \sigma_o)dz = \frac{m}{\pi R^2}\int_{v_o}^{o} v dv \qquad (6.8)$$

where: $\sigma_o = \sigma_o' + \gamma_w z$

$\sigma_o' = 1/3\ (1+2K_o)\ \gamma_b z$

$\gamma_b = \gamma - \gamma_w$

$s_u = S\sigma_{vo}'$

$\sigma_{vo}' = \gamma_b z$

γ_w, unit weight of water; K_o, coefficient of lateral stress at rest; γ_b, buoyant unit weight of the clay; γ, wet unit weight of the clay; S, ratio of undrained shear strength to initial

effective vertical stress σ_{vo}'; v_o, impact velocity of the penetrator.

Integrating Eq. 6.8 we obtain in terms of the kinetic energy K.E of the penetrator at impact, the penetration depth:

$$z = \sqrt{\frac{2(K.E.)}{\left\{\left[N_{sp}S + \frac{1}{3}(1+2K_o)\right]\gamma_b + \gamma_w\right\}A}} \qquad (6.9)$$

where K.E. $= \frac{1}{2}mv_o^2$, A=cross-sectional area of the penetrator.

A similar expression can be obtained using the alternative expression for point resistance based on centerline analysis. The above equation indicates that the total depth of penetration z: a) increases with increasing K.E. (i.e., increasing mass and increasing impact velocity of the penetrator), and b) decreases with increasing N_{sp} (i.e., decreasing ε_y), increasing unit weight and increasing shear strength of the soil and increasing cross-sectional area of the penetrator.

The validity of the above approach was evaluated by predicting depths in free-fall impact model tests on partially saturated compacted kaolin clay by Murff & Coyle (1973) with a 7.26 lb, 1.56 " dia. short ogive (1.25 caliber) at velocities of 18-116 ft/sec. Since a constant value for the undrained shear strength (4.1 psi from triaxial compression tests) was given by Murff & Coyle, Eq. 6.9 with constant k becomes

$$z = -\frac{N_{sp}}{\gamma} + \sqrt{\left(\frac{N_{sp}k}{\gamma}\right)^2 + \frac{2(K.E.)}{\gamma\pi R^2}} \qquad (6.10)$$

N_{sp} values for the prediction of penetration depths for clay were obtained by assuming a typical range of axial yield strain values, say 0.1 to 10%, in the absence of information on this. The predictions are plotted in Fig. 6.6 against the kinetic energy of the penetrator at impact: (a) depth of penetration and (b) ratio of predicted to actual depth, for the assumed limits of 0.1 and 10% for

the axial yield strain of the clay. One will note that we overpredict penetration depth with increasing discrepancy as kinetic energy increases (overprediction of 30-300% at the lowest velocity to 590-1300% at the highest velocity). There are three classes of possible reasons for this. First, there are possible inaccuracies in the experimental data (measurement of soil properties especially the undrained shear strength and other parameters in the problem). It should be stressed that the model can only be verified by using available data and verifications conducted are also subject to the limitations of the experiment. Second, test conditions deviate from the basic assumptions of the model (e.g., incompressibility vs. compressibility of partially saturated clay, isotropic state of stress vs. anisotropic state of stress in compacted clay and absence of interface friction vs. the presence of interface friction). Third, there are factors which may be important but not included in the model (e.g., strain rate effects, inertial resistance and tip shape effects).

6.4.2 Effect of Strain Rate

It has been observed that decreasing the time to failure results in an increase in the undrained shear strength of clays. Lacasse (1979) in an extensive literature review reports that the increase in undrained shear strength of clay varies with the logarithm of time to failure. Increase in the undrained shear strength ranges from 3 to 20% per log cycle of time for time to failure of 1-140 min in triaxial tests. The strain rate effect for clays increases with higher plasticity and higher overconsolidation ratio OCR.

The undrained shear strength s_u of a clay sheared at a rate of $\dot{\varepsilon}$, in terms of its strength $(s_u)_o$ at some reference rate of straining $\dot{\varepsilon}_o$, can be expressed as

$$s_u = (s_u)_o\left[1 + \alpha \log_{10}\left(\frac{\dot{\varepsilon}}{\dot{\varepsilon}_o}\right)\right] \qquad (6.11)$$

where α is the strain rate factor, the increase in strength per log cycle of time to failure.

Using the expression for the rate of axial straining at the centerline for the simple pile (Eq. 13, Appendix C), the rate of straining at the tip is given by

$$\dot{\epsilon}_{zz} = \frac{4U}{R} \qquad (6.12)$$

where U is the velocity of penetration and R the radius of the simple pile. Thus, Eq. 6.11 can be expressed as

$$s_u = (s_u)_o\left[1 + \alpha \log_{10}\left(\frac{4U/R}{\dot{\epsilon}_o}\right)\right] \qquad (6.13)$$

Three values of α (0.10, 0.15, 0.20) based on the results of Lacasse's study were used to incorporate rate effects in our predictions. We used modified s_u values based on the impact velocity of the penetrator and the standard shearing rate in a triaxial test (=0.5% /hr). The corrected plots are shown in Fig. 6.7, 6.8, and 6.9 for α values of 0.10, 0.15, and 0.20, respectively. The reader will note that the predictions have been brought closer to the actually observed depths with the improvement increasing with larger α values. The penetration depths are still overpredicted, and this, to a larger extent at high kinetic energies.

6.4.3 Effect of Skin Friction

The simple pile solution assumes that the penetrator is smooth which means that there is no interface friction between the penetrator and the ground. However, if the penetrator is rough and is in full contact with the ground during the penetration process, then sidewall resistance will be developed.

Theoretically, the unit skin friction may be assumed to consist of two components: adhesion a, which is independent of the normal stress q_s acting on the shaft of the penetrator and friction, which should be proportional to the normal stress (Vesic 1977). This may be expressed as

$$f_s = a + q_s \tan \delta \qquad (6.14)$$

where tan δ represents the coefficient of friction between the ground and the shaft of the penetrator.

In the absence of information on ground-penetrator properties a and δ and an analytical expression for the distribution of q_s during penetration (the two-dimensional stress field solution is being developed at present), an estimate can be generated by using available empirical data on pile capacity. For clays, it was found that the skin friction can be expressed as a factor of the undrained shear strength s_u (Tomlinson 1957)

$$f_s = \beta s_u \qquad (6.15)$$

where β is a coefficient varying from 0.2 to 1.5 depending on the pile type and soil conditions. It has been suggested that for soft to firm clays (s_u < 0.5 tsf), β should be 1.0. Therefore, the additional resisting force $F_s(z)$ due to skin friction acting on the penetrator at any depth z is given by

$$F_s(z) = 2\pi R z \cdot s_u \qquad (6.16)$$

The above expression was used to incorporate skin friction in our case study based on the experimental data by Murff & Coyle, and it will be noted that the predictions have been brought down considerably even at high K.E.'s (Fig. 6.10). This is due to the fact that the depth of penetration is larger at higher velocities; consequently, relatively larger corrections have been applied to these data points.

It is interesting to note that the Strain Path Method with its assumption of no interface friction has been successfully applied to clays of low overconsolidation ratio (OCR = 1-4) in cone penetration tests (Baligh 1985; Elghaib 1989) and pile installation problems (Whittle 1987). However, in our case study, we have a compacted clay whose behavior is similar to that of an overconsolidated clay. Application of the skin friction correction modified our predictions such that the overprediction is consistently low even at high kinetic

energies, a result which was not achieved when only the strain rate effect correction was applied. This may be an indication that skin friction is important for highly overconsolidated clays.

Dayal and Allen (1975) observed that interface friction is also strain-rate dependent based on sleeve friction measurements from static cone penetration tests on pottery clay. They found that skin friction increases with the logarithm of velocity of penetration by at least 17% per log cycle of velocity in the range of 0.0044-0.456 ft/sec and at least 38% per log cycle beyond 0.456 ft/sec to 2.662 ft/sec.

We decided therefore to apply both the strain rate and the skin friction correction simultaneously. As Fig. 6.11 and 6.12 show, these corrected predictions lie within the range of observed data (Murff & Coyle) for the range of ε_y values assumed and for α values of 0.10 and 0.15, respectively.

6.5 Penetration Depth Predictions in Sands

6.5.1 Basic Model (Point Resistance Only)

An approach similar to that in clays can be used to express penetration depth in sands. The point resistance from centerline analysis (Eq. 6.6), the only available closed-form expression for point resistance, is used. Substituting this result in the equation of motion (Eq. 6.1) we have

$$-\int_0^z (N_\sigma \sigma_o')dz = \frac{m}{\pi R^2}\int_{v_*}^0 dz \qquad (6.17)$$

where σ_o' is the isotropic effective stress in the soil, as defined for clays. Integrating Eq. 6.14, we obtain in terms of the K.E. of the penetrator at impact the penetration depth

$$z = \sqrt{\frac{2(\text{K.E.})}{N_\sigma[(1+2K_o)\gamma_b + \gamma_w]A}} \qquad (6.18)$$

Therefore, as in clays, the penetration depth z: a) increases with increasing K.E. of the penetrator at impact and b) decreases with

increasing N_σ (i.e., increasing angle of friction ϕ' and increasing axial yield strain ε_y) and increasing cross-sectional area A of the penetrator.

Data from impact penetration tests by Wang (1971) on loose and dense Ottawa sand were used to evaluate the model. Wang used a cylindrical flat-ended penetrator with weights of 0.088 to 2.93 lb, impact velocities of 10 to 25 ft/sec and diameters of $\frac{3}{4}$, $1\frac{1}{2}$ and 2". Ground properties such as friction angle ϕ' and axial yield strain ε_y were taken from data on Ottawa sand collected by Elghaib (1989) (loose, $\phi'=35.9^o$, $\varepsilon_y=1.15\%$; dense, $\phi'=43^o$, $\varepsilon_y=0.107\%$). It will be noted that the range of parameters studied is such that the actual penetration depths into sand are relatively shallow especially for dense sand (Fig. 6.13) as compared to the diameters of penetrator of $\frac{3}{4}$, $1\frac{1}{2}$, and 2" used. The results of the predictions are shown in Fig. 6.13 and 6.14 for dense and loose sands, respectively. The predictions are plotted against the ratio of the kinetic energy K.E. of the penetrator at impact to its cross-sectional area A. Fig. 6.13(a), 6.14(a) show penetration depth and Fig. 6.13(b), 6.14(b), the ratio of predicted to actual depth. It will be noted that for the loose sand, penetration depth is overpredicted on the average by 27% with larger overpredictions at low K.E./A ratios. On the other hand, for the dense sand, penetration depth is underpredicted on the average by 11% with larger underpredictions at high K.E./A's.

Again, the discrepancy between the predicted and actual values may be attributed to three classes of possible reasons as cited in the predictions for clay: possible inaccuracies in the experimental data of the case study, deviation of test conditions from basic assumptions of the model (e.g., incompressibility vs. compressibility of real sand, deep penetration vs. shallow penetration and absence of friction vs. presence of friction) and non-inclusion in the model of effects such as those of high strain rate, of inertia of the target material and of tip shape.

6.5.2 Effect of Strain Rate

The earliest tests on the effect of time of loading on dry sands were performed by Casagrande and Shannon (1949) on dense Manchester sand. They observed a 10% increase in strength from a 10-min static, to a 0.02-sec rapid loading, triaxial compression test (equivalent to 2.2% increase in strength per log cycle of time of loading). Whitman & Healy (1962) found only a slight variation in friction angle (likely to be less than 5%, no more than 10%) based on triaxial compression tests on dry loose and dense Ottawa sand from a rate of loading of 0.012 in/sec to 18 in/sec. Schimming, Hass & Saxe (1966) performed dynamic direct simple shear tests on dry loose and dense ASTM C-190 sand with time to failure of 1-5 milliseconds and compared them with rapid static tests with time to failure of 30-50 sec. They concluded that dynamic effects are minimal. Dayal and Allen (1975) performed constant-velocity cone penetration tests on dry silica-70 loose and dense sand at velocities of 0.0044-2.662 ft/sec. They observed no appreciable difference in either cone or friction sleeve resistance. Based on the above tests, we can conclude that there is no significant strain rate effect on the strength of dry sands.

In undrained loading of saturated sands, the strain rate effect may be important as Seed and Lundgren (1954) report an increase of 15-20% in strength for both loose and dense Sacramento sand from slow (6 in/min) to rapid (40 in/min) transient triaxial compression tests. On the other hand, Whitman & Healy (1962) report an increase by as much as 40% in the strength of dense Ottawa sands as the displacement rate increased from 0.08 in/sec to 18 in/sec in triaxial compression tests, but they observed no change in strength on loose Ottawa sand.

In our case study we are using data from Wang (1971), which come from tests on dry sand. In such cases, corrections for strain rate effects are not needed.

6.5.3 Effect of Skin Friction

The theoretical considerations on skin friction for sands are similar to those for clays. In the absence of information needed for a

theoretical analysis, skin friction in sands may then be estimated by assuming that the coefficient of friction between the soil and the penetrator shaft is $\tan\phi'$ and that at least lateral ground conditions at rest exist (therefore, the coefficient of lateral stress may be approximated by $1-\sin\phi'$). Thus, assuming skin friction f_s to be composed of a friction component only (adhesion is negligible), then f_s is given by

$$f_s = (1 - \sin\phi')\tan\phi'\sigma_{vo}' \qquad (6.19)$$

and the additional resisting force due to skin friction is thus given by

$$F_s(z) = 2\pi R(1 - \sin\phi')\tan\phi'\gamma_b z^2 \qquad (6.20)$$

Integration of the equation of motion with skin friction included results in a cubic equation which is solved numerically.

Incorporating skin friction means that an additional force resists penetration. Thus, the original predictions for the loose sand improved considerably (the average overprediction was lowered by 9%) (Fig. 6.15) while those for the dense sand were unchanged. This is so because for the dense sand, the point resistance is high (N_σ=402) and the contact area is small with penetration being shallow; the relative change due to skin friction is therefore minimal. For the loose sand, however, the point resistance is lower (N_σ=39.8) and the contact area is larger as penetration is relatively deep; thus, interface friction becomes significant.

6.6 Effect of Inertia, Free Surface, Tip Shape and Others

The inertia of the ground mass is believed to become important in the penetration process as the velocity of the penetrator increases. As the velocity of the penetrator increases, a considerable amount of energy becomes available to displace and impart velocity of considerable magnitude to the target material around the ground-penetrator interface. This can occur in both the vertical and lateral (radial) directions. The relative velocity of penetration at which

resistance due to inertia of the ground mass becomes significant still has to be investigated.

There are a number of ways in which the effect of inertia of the ground mass can be considered.

Hill (1980) in his cavitation model proposed that the inertial effect causes a cavity larger than the penetrator to be formed due to plastic flow of the target material around the penetrator at high velocities. This was observed in experiments on metals. Hill's model, however, is semi-empirical because he uses an expression for inertial resistance with constants to be determined from experiments. For ground masses, no experimental data have been found yet on the velocity of penetration at which cavitation occurs.

Inertial effects may be present in the high rate of straining of clay. Whether inertial effects have been reflected in part or in whole by incorporating strain rate effects in clay is uncertain.

So far, only deep penetration has been considered. The shallow penetration mechanism may be different. Free-surface or shallow penetration effects will be significant only if 1) the shallow stage makes up a substantial portion of the penetration process and 2) its mechanism is different. Thus, we need to determine if shallow penetration is different and if so, the extent by which it differs from deep penetration. If it is important, we also have to know to which category, shallow or deep, our problem cases belong.

An approximate method to model shallow penetration using the results from the Strain Path Method is to assume that the strain rate field around the penetrator is the same as that for deep penetration but extending only up to the level of the free surface. Then the energy required to cause this deformation is evaluated which can be expressed in terms of the depth of embedment.

We also have to determine how accurate it is to use the blunt-tip simple pile geometry to model general penetrator shapes for impact penetration.

The penetration depth model for frictional materials has been applied to sand assuming it is an incompressible material. However, sands exhibit compressibility. Therefore, this has to be addressed in further research, also.

6.7 Conclusions

A simple analytical model for penetration depth prediction based on point resistance of the simple pile from the Strain Path Method has been developed for incompressible cohesive and frictional ground. It requires only a few parameters which can be easily determined (s_u, ε_y for clays and ϕ', ε_y for sands). The model gives reasonable predictions for sands using published data on impact penetration by Wang (1971). On the average, for the dense sand, the predictions are within 10% of actual values; for the loose sand, within 30%. This is satisfactory considering the simple approximation used. The model significantly overpredicts penetration depths in compacted clay using experimental data by Murff & Coyle (1973).

Incorporating effects of factors such as strain rate and skin friction can be done in a similarly simple manner. Including effects of skin friction in dry loose sands using data by Wang improves the predictions considerably. Including the effects of strain rate and skin friction in clays using data by Murff brings predictions close to the measured values. This indicates that strain rate and skin friction effects are important in penetration into overconsolidated clays and that the Strain Path Method can be extended to include these effects to give realistic estimates of penetration depth.

Since we can predict penetration depth reasonably well using a Strain Path-based approach, we can say that the basic principles of the Strain Path Method are adequate to model the rapid penetration process.

The effects of inertia and compressibility of the target material, the free surface and penetrator tip shapes are not well understood yet and need to be investigated in further research.

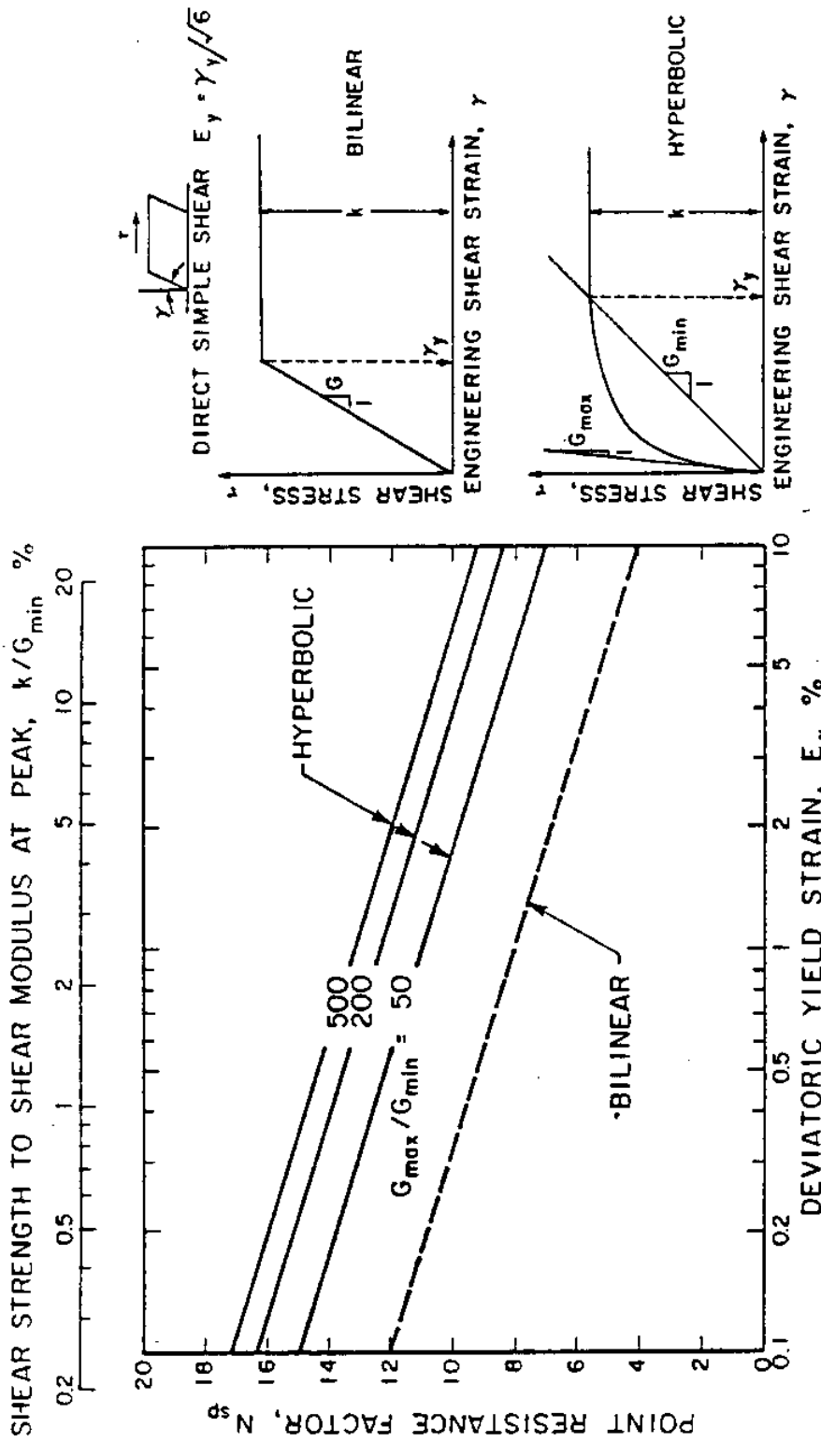

Fig. 6.1 Predicted Point Resistance of the Simple Pile in Clays (after Baligh 1985a)

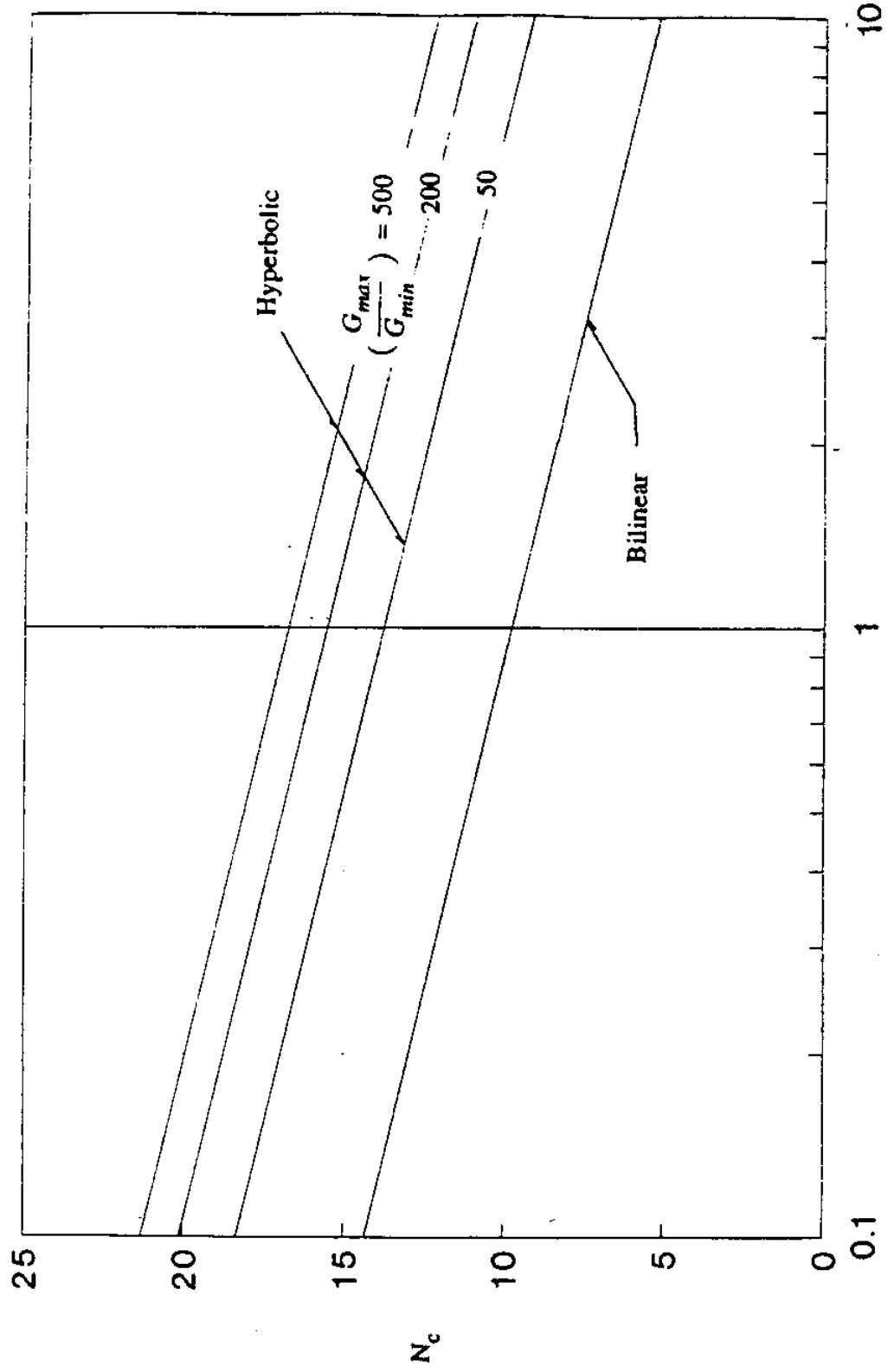

Fig. 6.2 Predictions of Point Resistance Factor during Simple Pile Penetration in Isotropically Consolidated Clays (after Elghaib 1989)

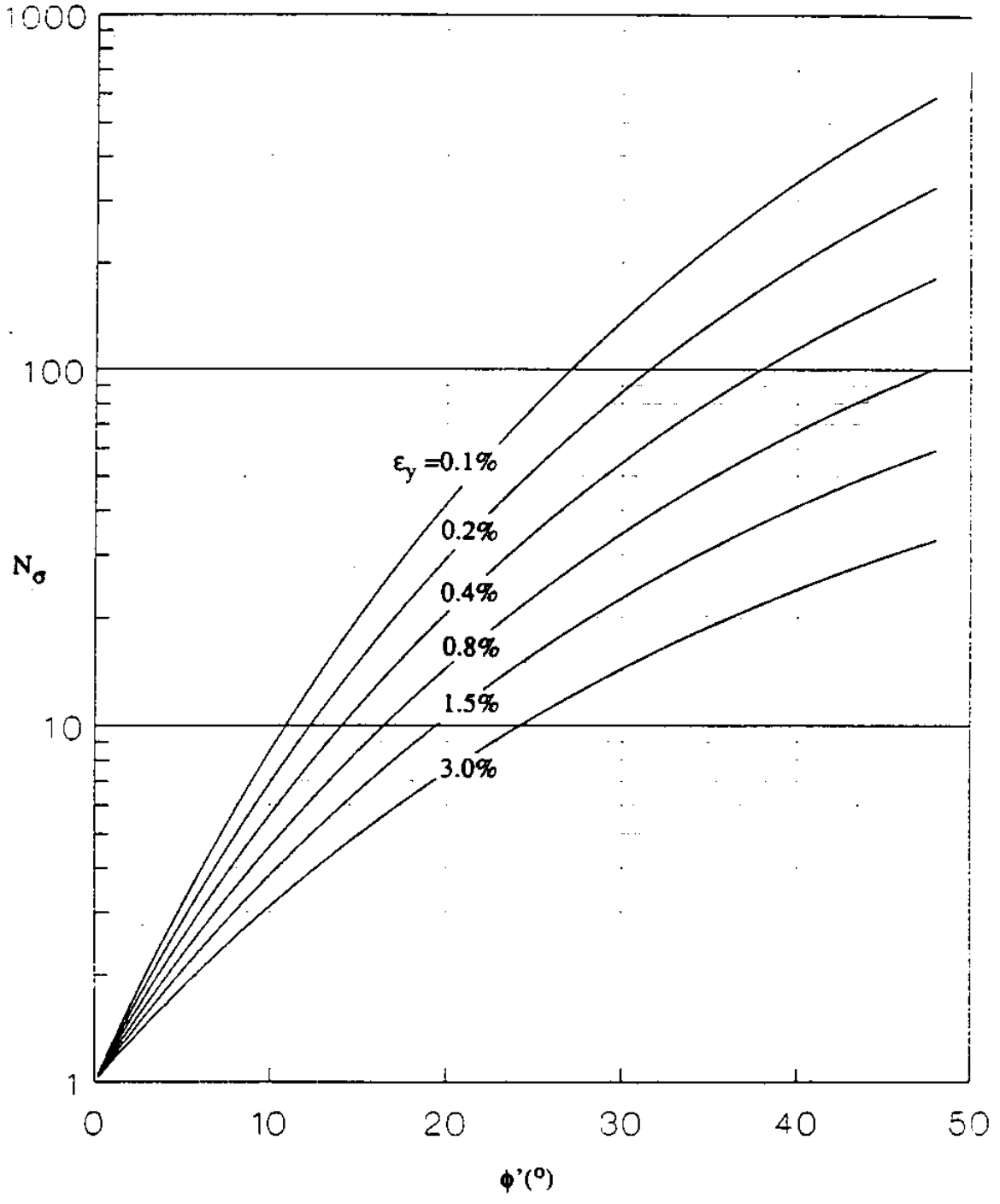

Fig. 6.3 Point Resistance Factor vs. Friction Angle
(after Elghaib 1989)

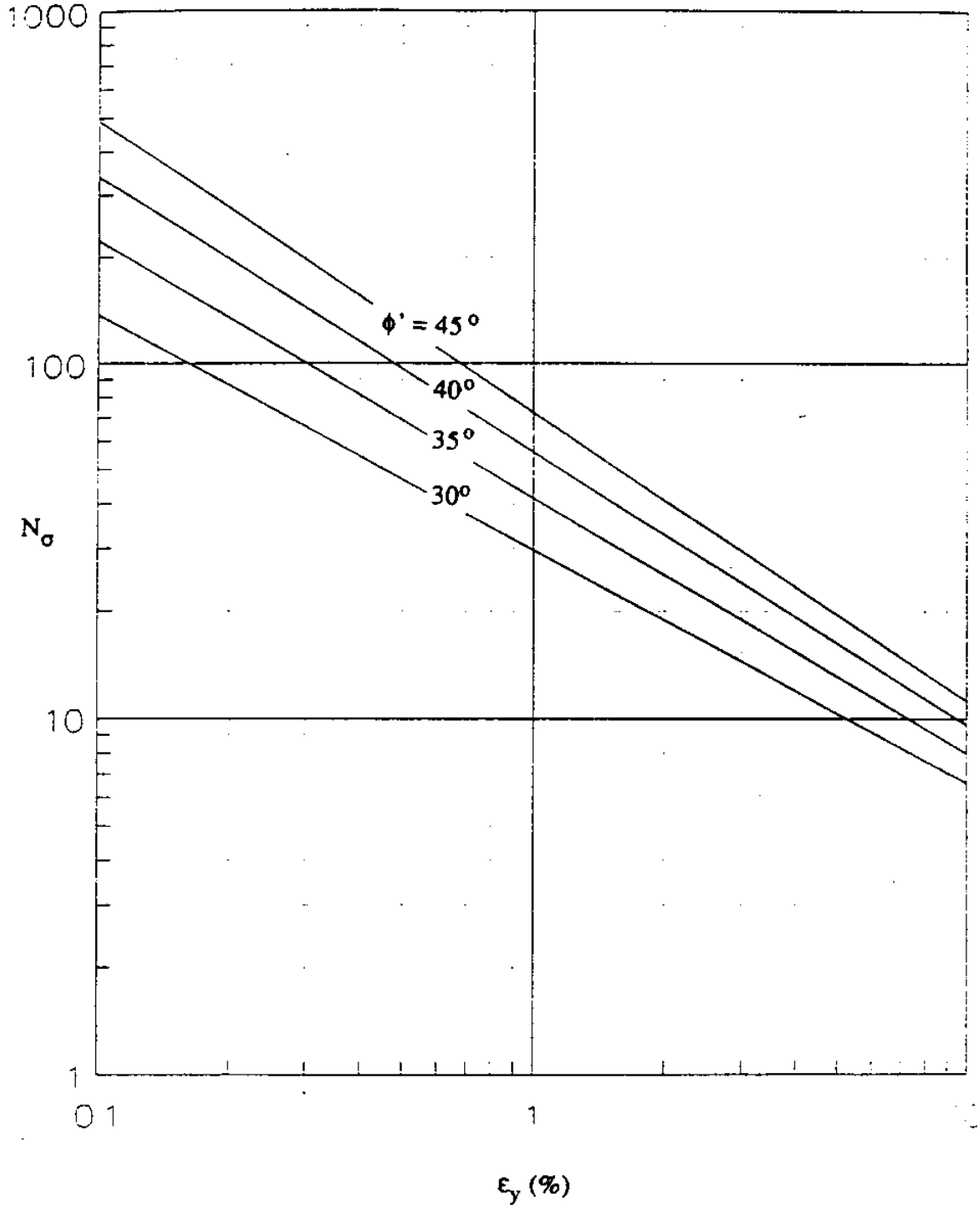

Fig. 6.4 Point Resistance Factor vs. Axial Yield Strain
(after Elghaib 1989)

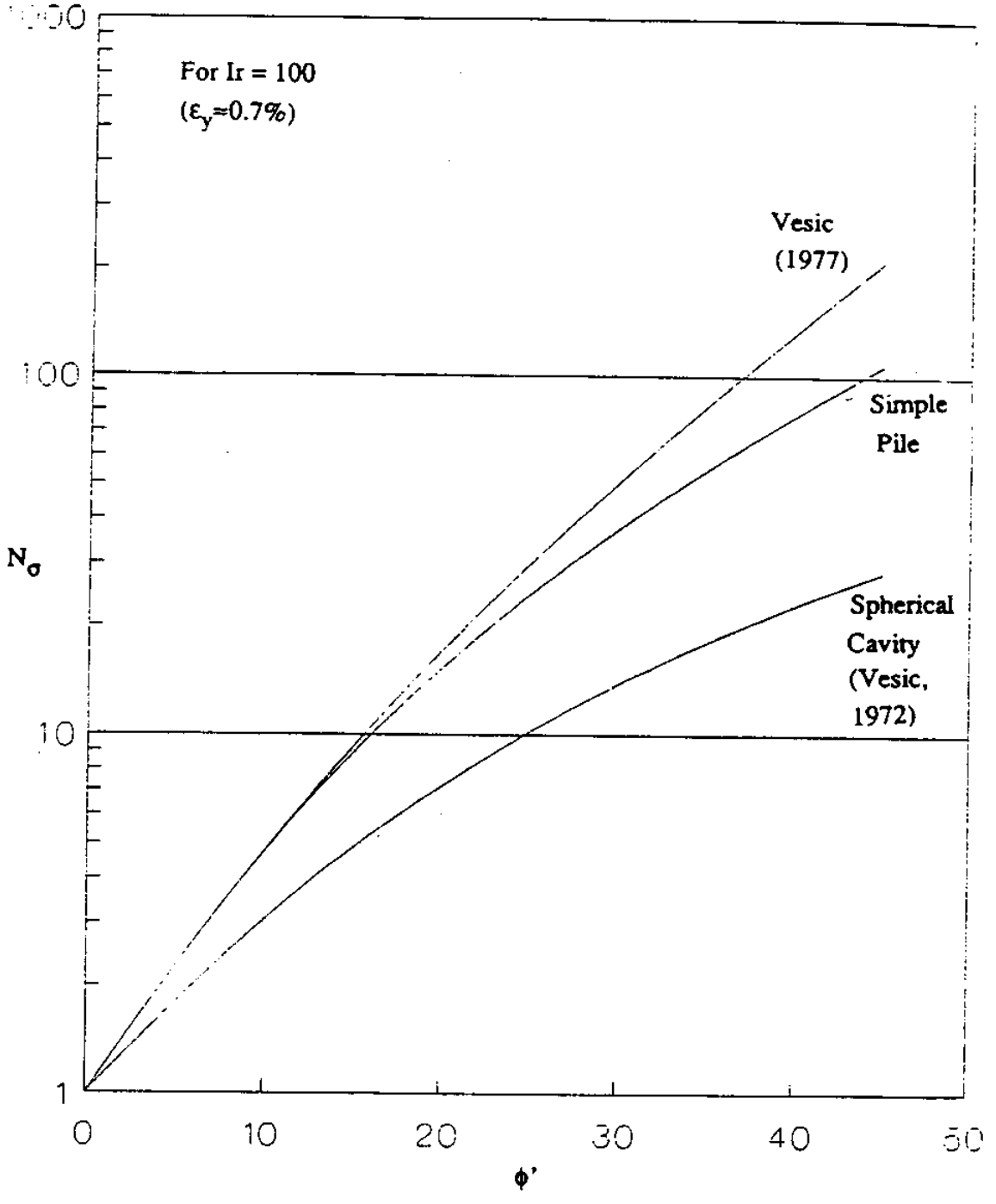

Fig. 6.5 Comparison between Simple Pile and Spherical Cavity Predictions (after Elghaib 1989)

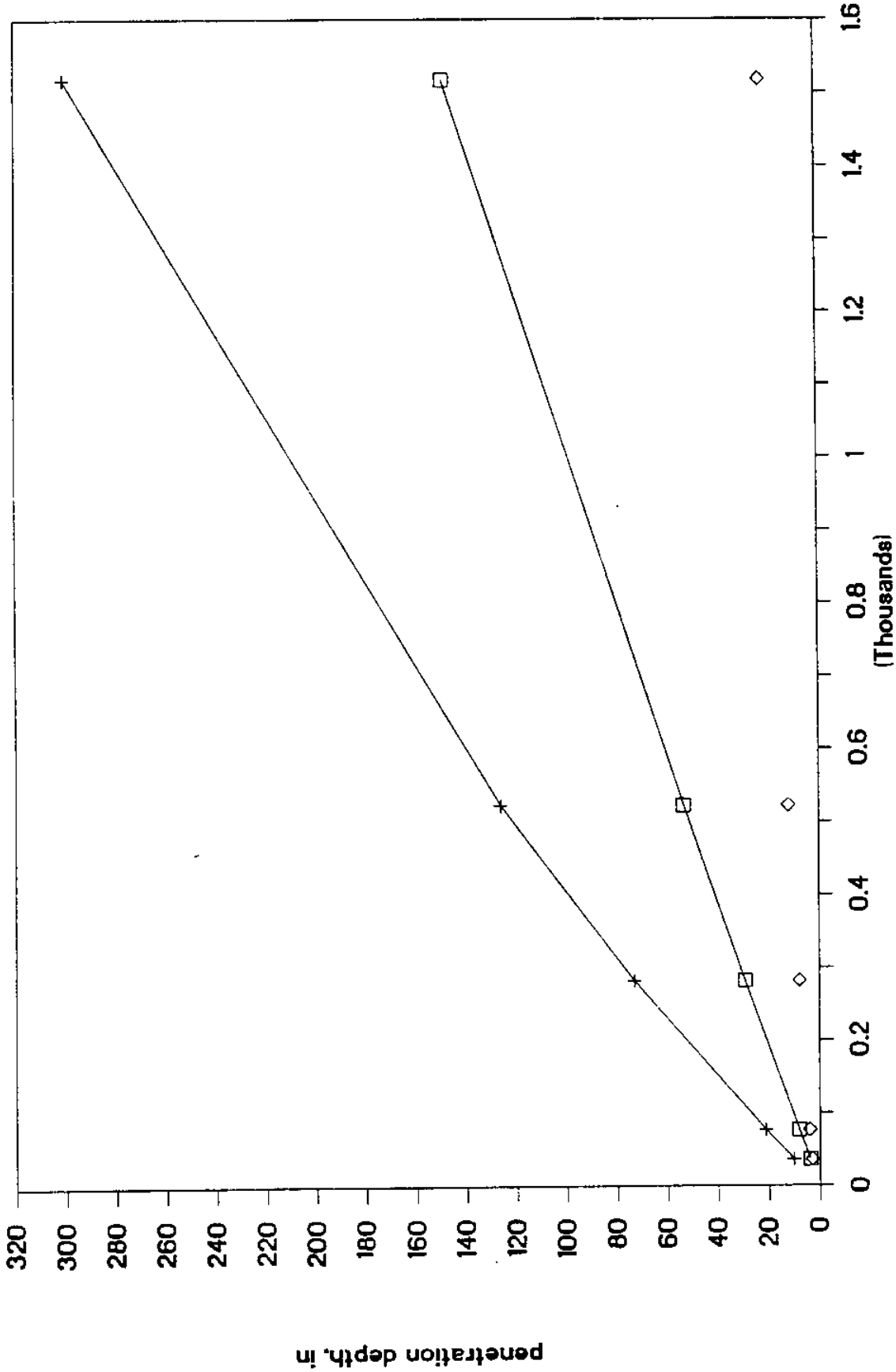

Fig. 6.6 Penetration Depth Predictions in Clay: Basic Model (Point Resistance Only)
(a) penetration depth vs. kinetic energy of the penetrator at impact

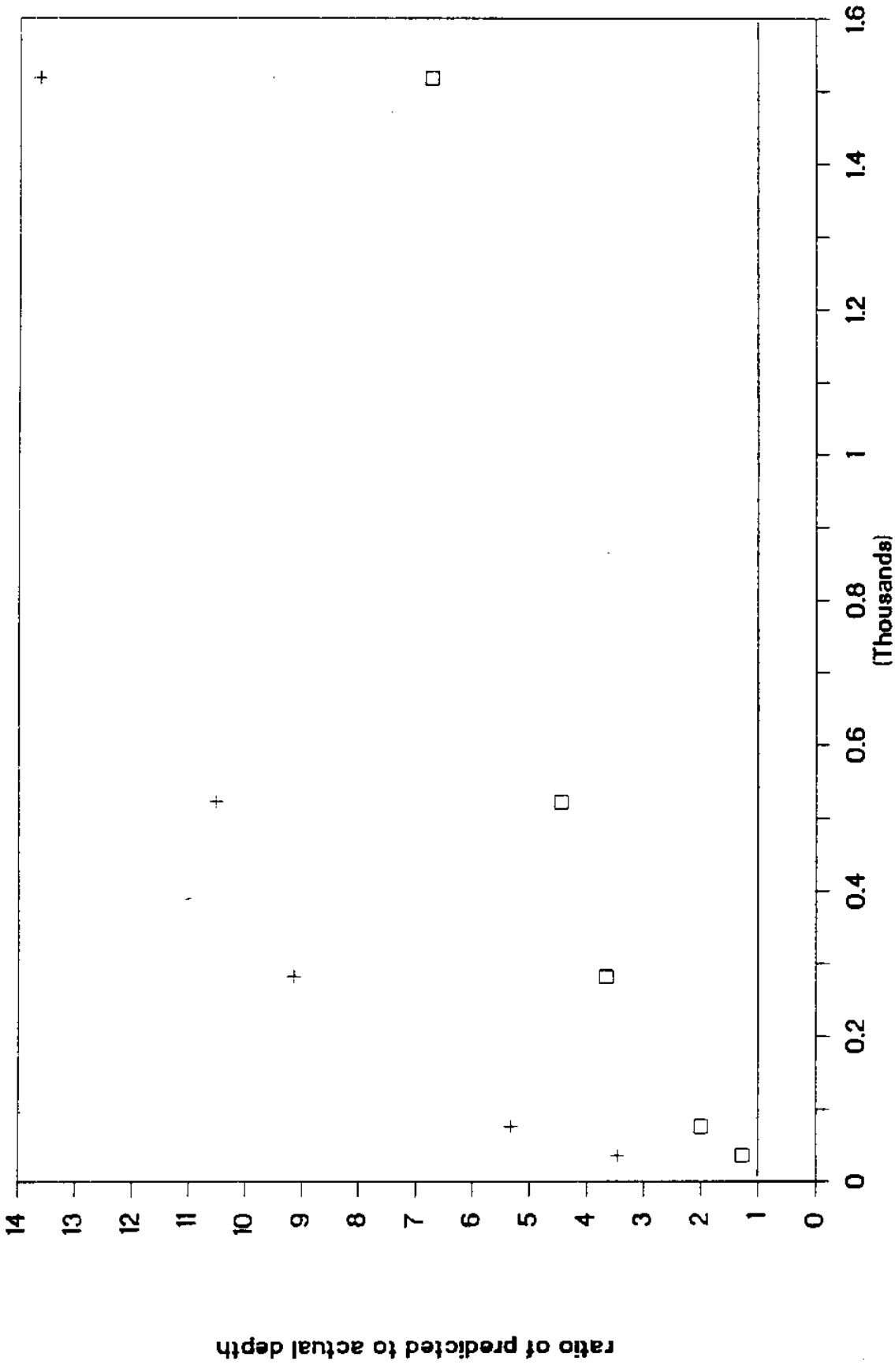

Fig. 6.6 Penetration Depth Predictions in Clay: Basic Model (Point Resistance Only)
(b) ratio of predicted to actual penetration depth vs. kinetic energy of the penetrator at impact

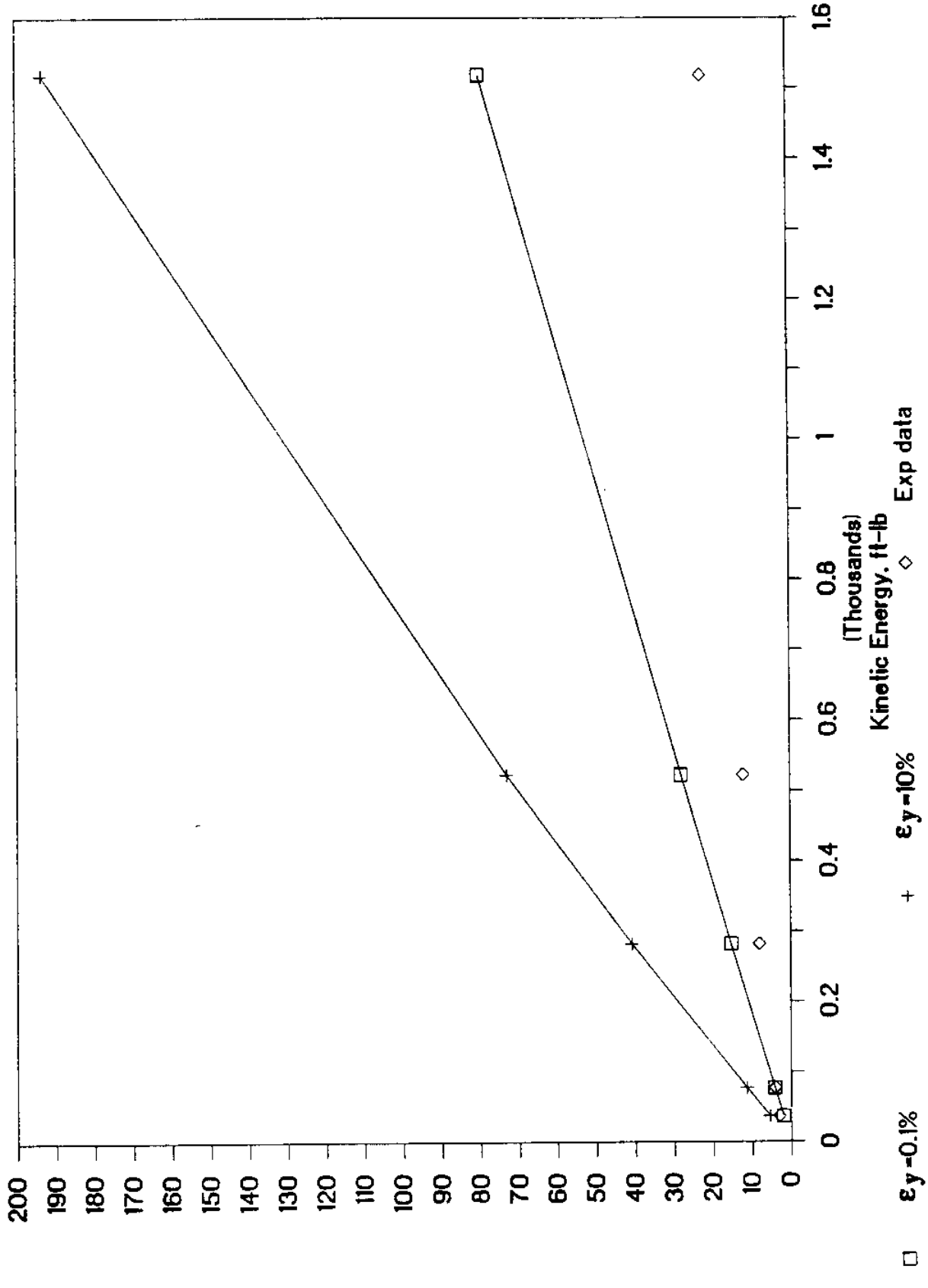

Fig. 6.7 Penetration Depth Predictions in Clay: Corrected for Strain Rate (α=0.10)
(a) penetration depth vs. kinetic energy of the penetrator at impact

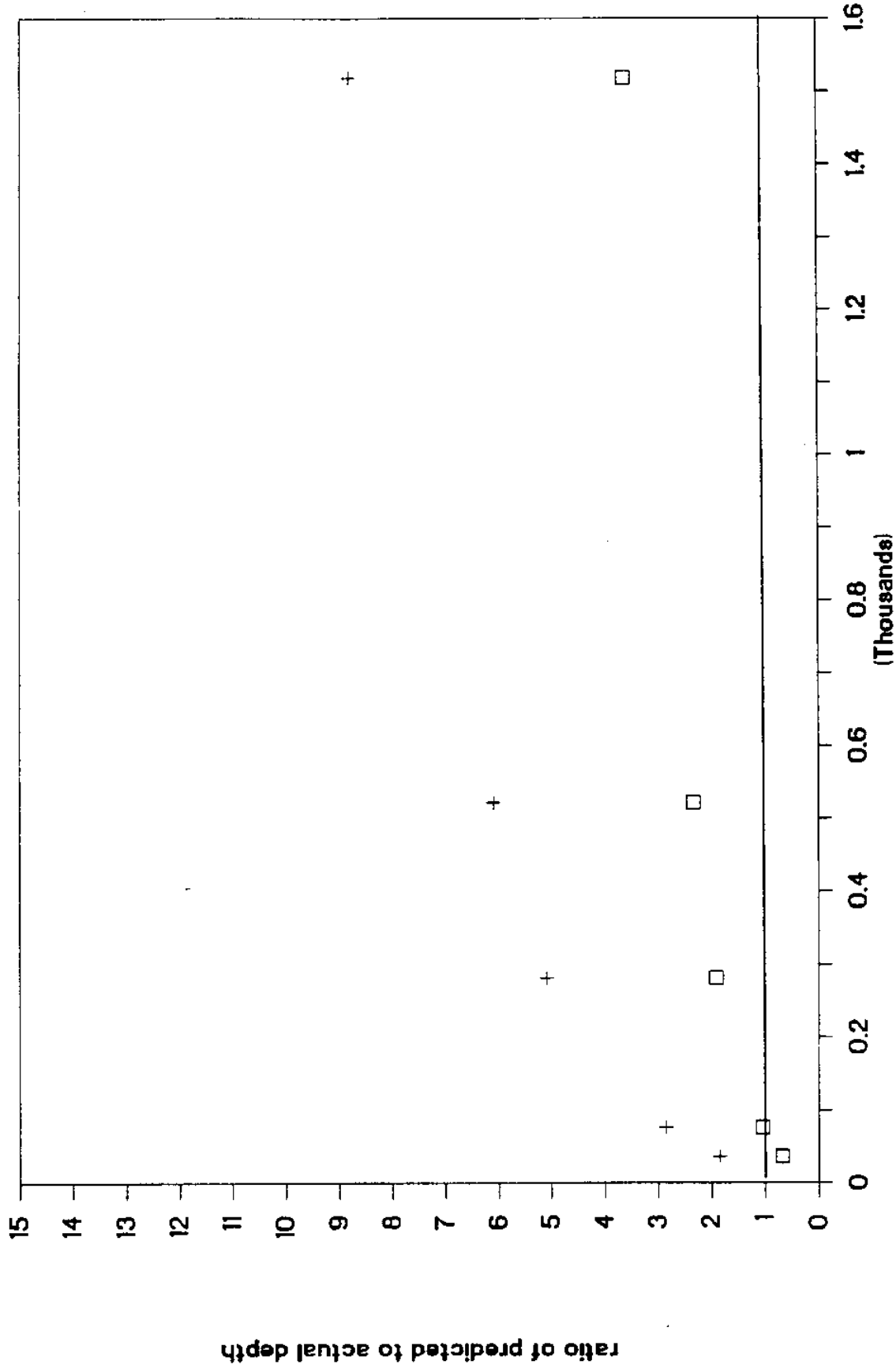

Fig. 6.7 Penetration Depth Predictions in Clay: Corrected for Strain Rate (α=0.10)
(b) ratio of predicted to actual penetration depth vs. kinetic energy of the penetrator at impact

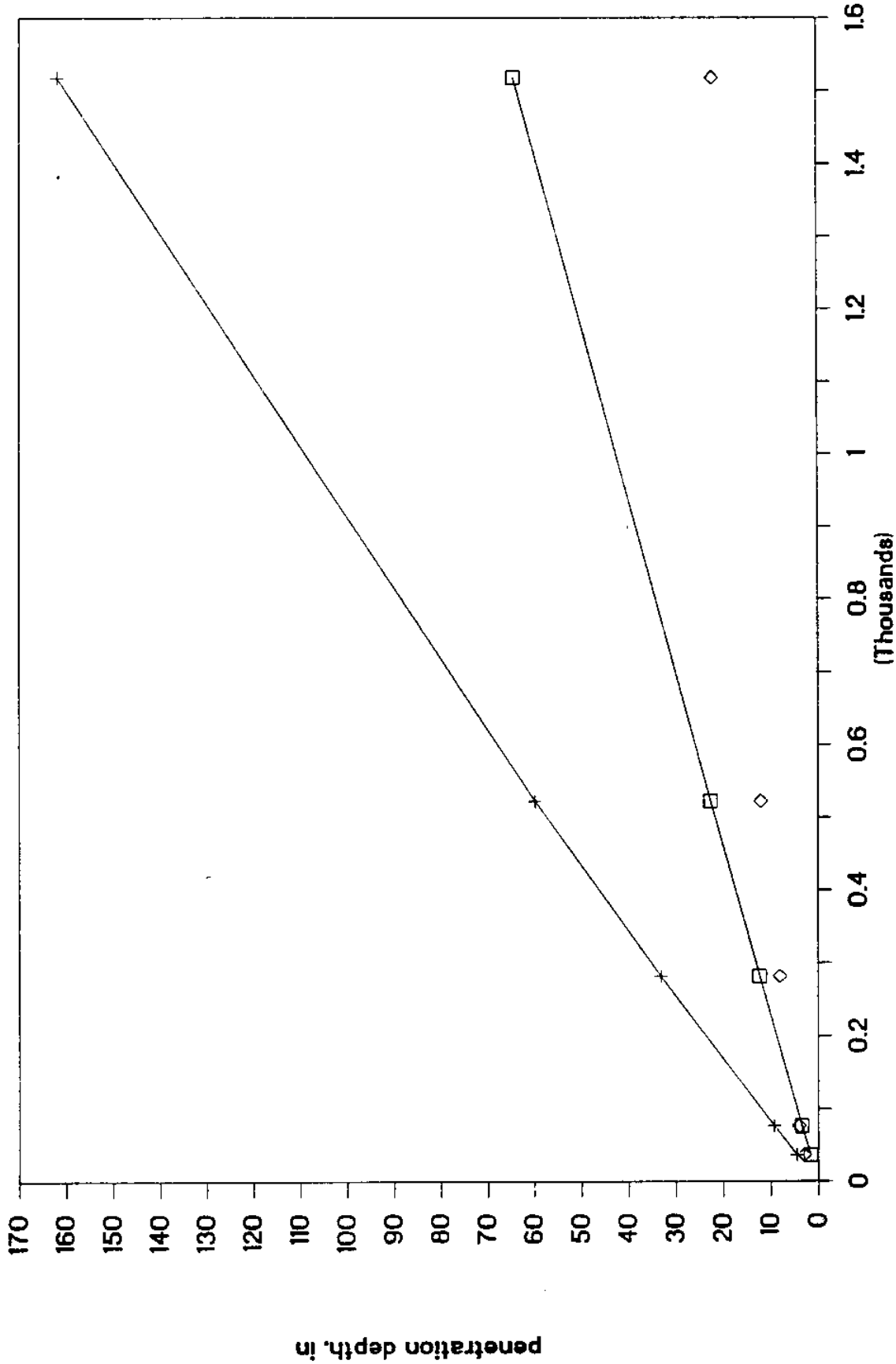

Fig. 6.8 Penetration Depth Predictions in Clay: Corrected for Strain Rate (α=0.15)
(a) penetration depth vs. kinetic energy of the penetrator at impact

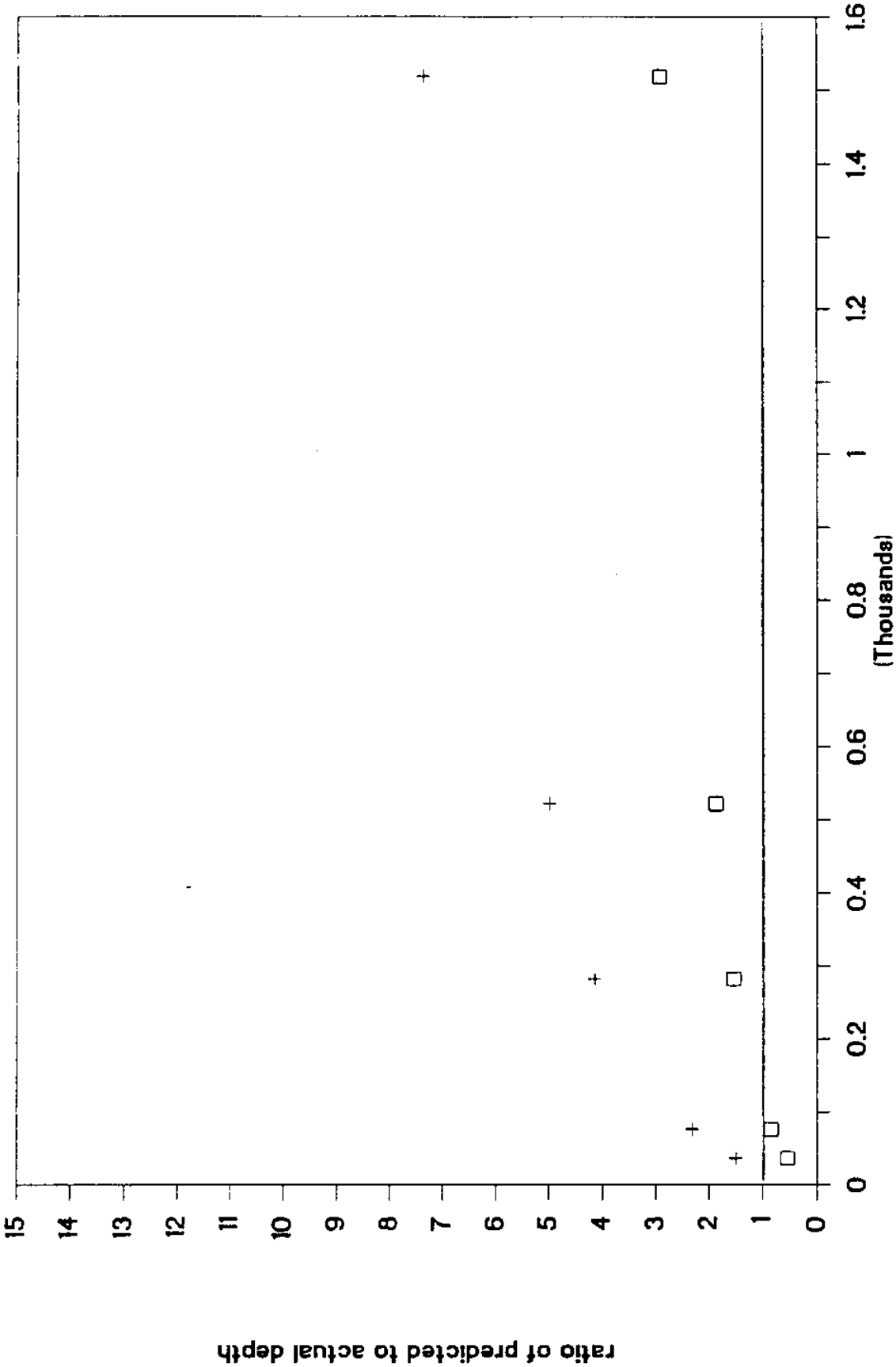

Fig. 6.8 Penetration Depth Predictions in Clay: Corrected for Strain Rate (α=0.15)
(b) ratio of predicted to actual penetration depth vs. kinetic energy of the penetrator at impact

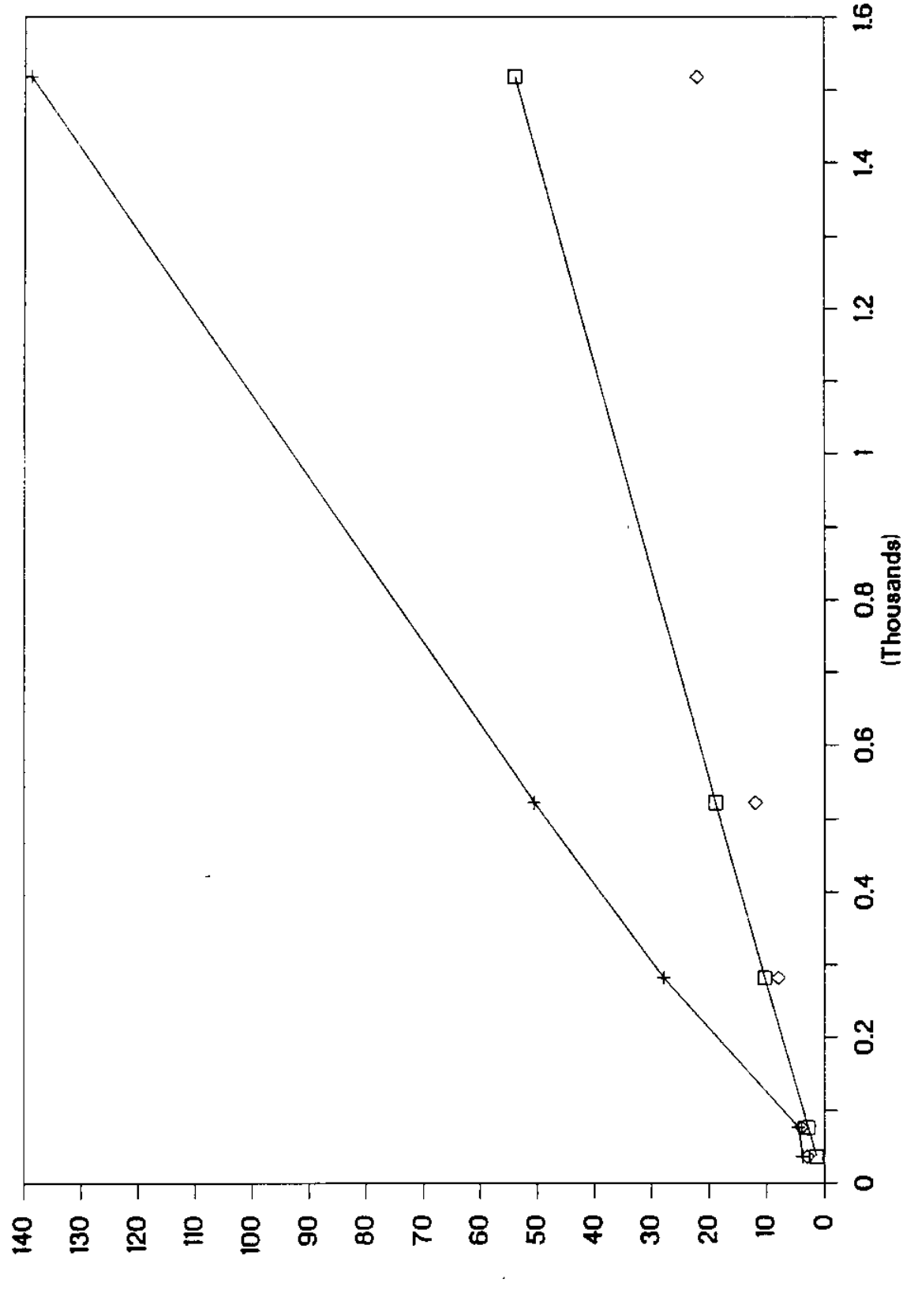

Fig. 6.9 Penetration Depth Predictions in Clay Corrected for Strain Rate (α=0.20)
(a) penetration depth vs. kinetic energy of the penetrator at impact

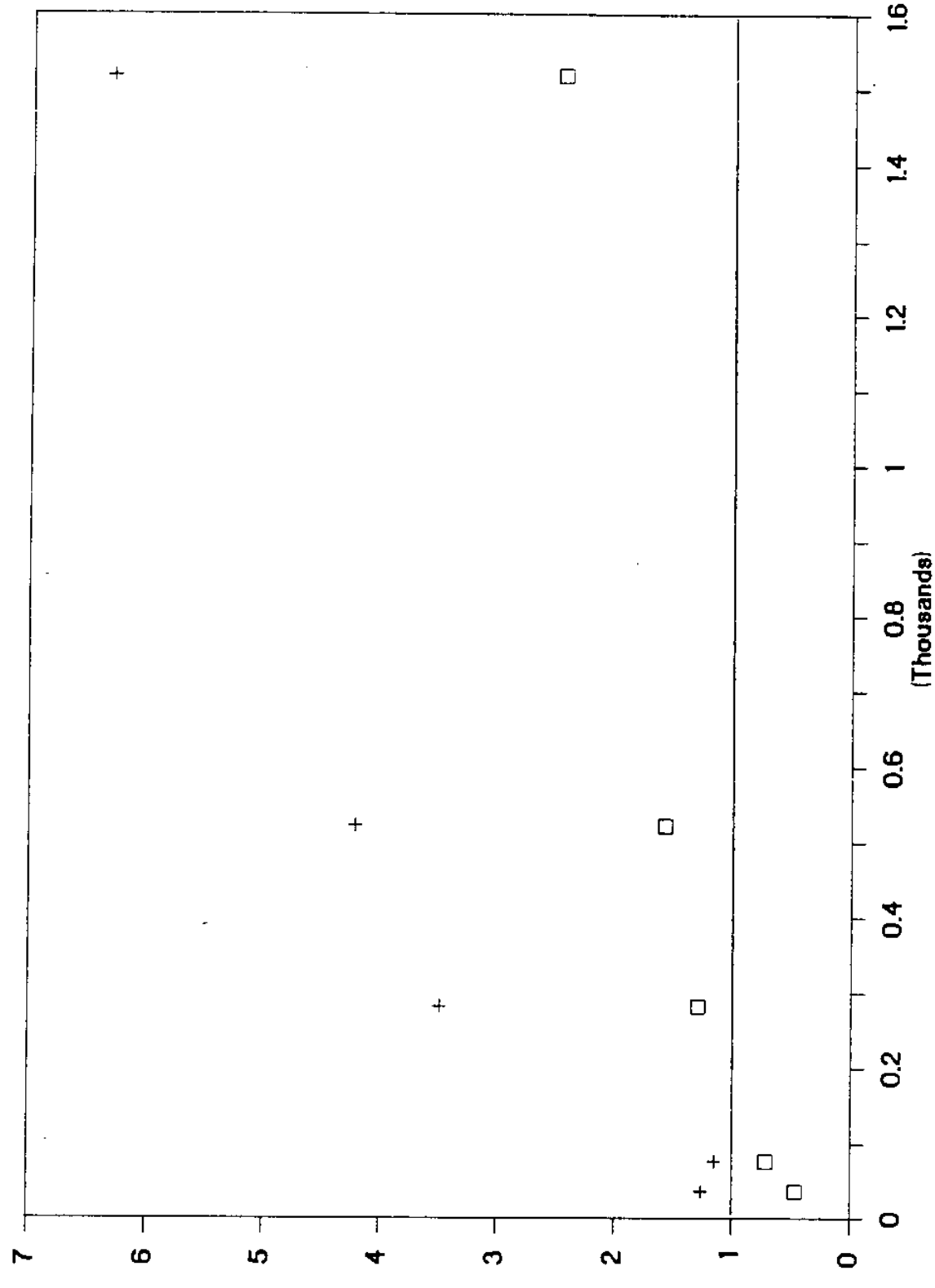

Fig. 6.9 Penetration Depth Predictions in Clay: Corrected for Strain Rate (α=0.20)
(b) ratio of predicted to actual penetration depth vs. kinetic energy of the penetrator at impact

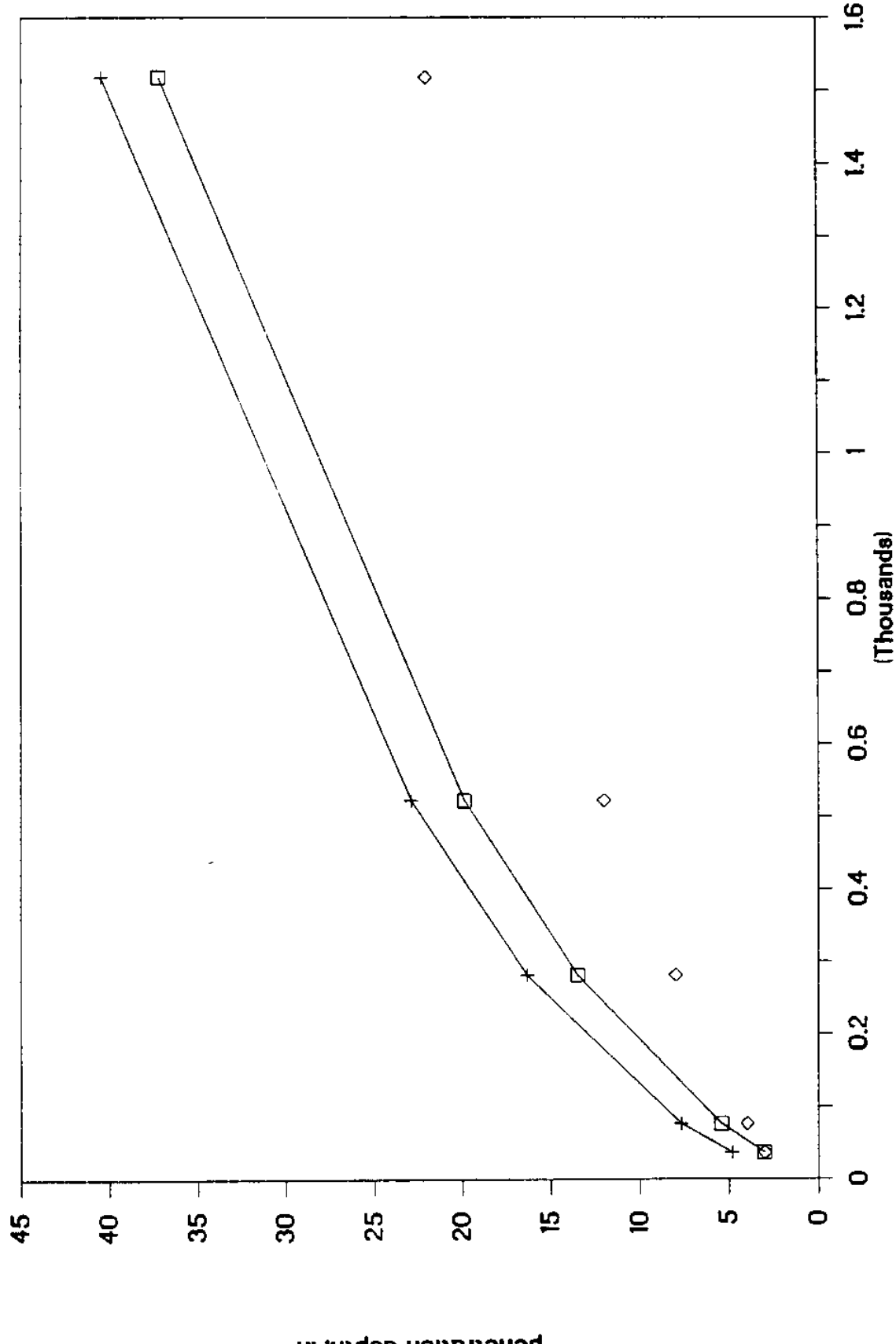

Fig. 6.10 Penetration Depth Predictions in Clay: Corrected for Skin Friction
(a) penetration depth vs. kinetic energy of the penetrator at impact

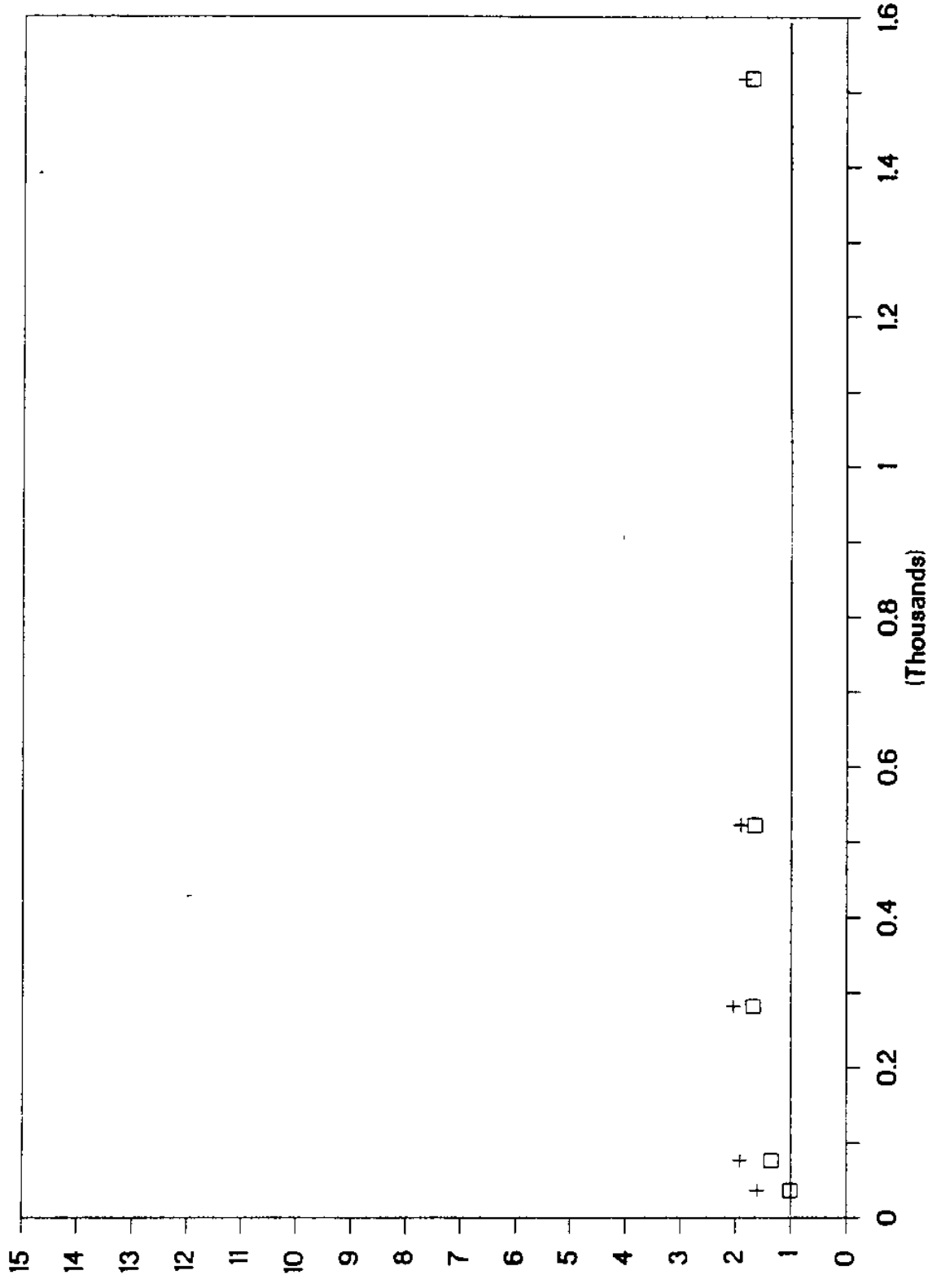

Fig. 6.10 Penetration Depth Predictions in Clay: Corrected for Skin Friction
(b) ratio of predicted to actual penetration depth vs. kinetic energy of the penetrator at impact

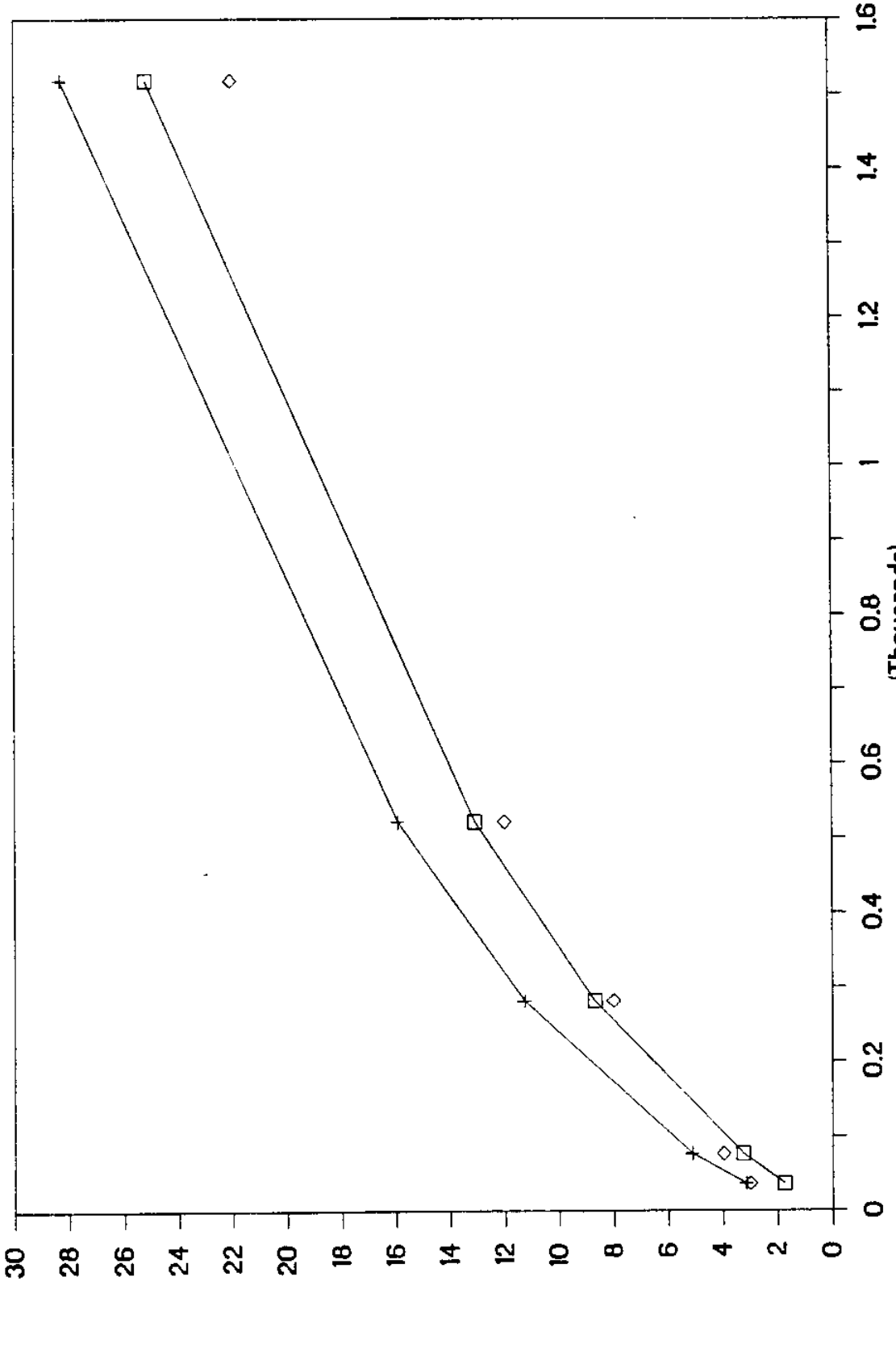

Fig. 6.11 Penetration Depth Predictions in Clay: Corrected for Strain Rate (α=0.10) & Skin Friction
(a) penetration depth vs. kinetic energy of the penetrator at impact

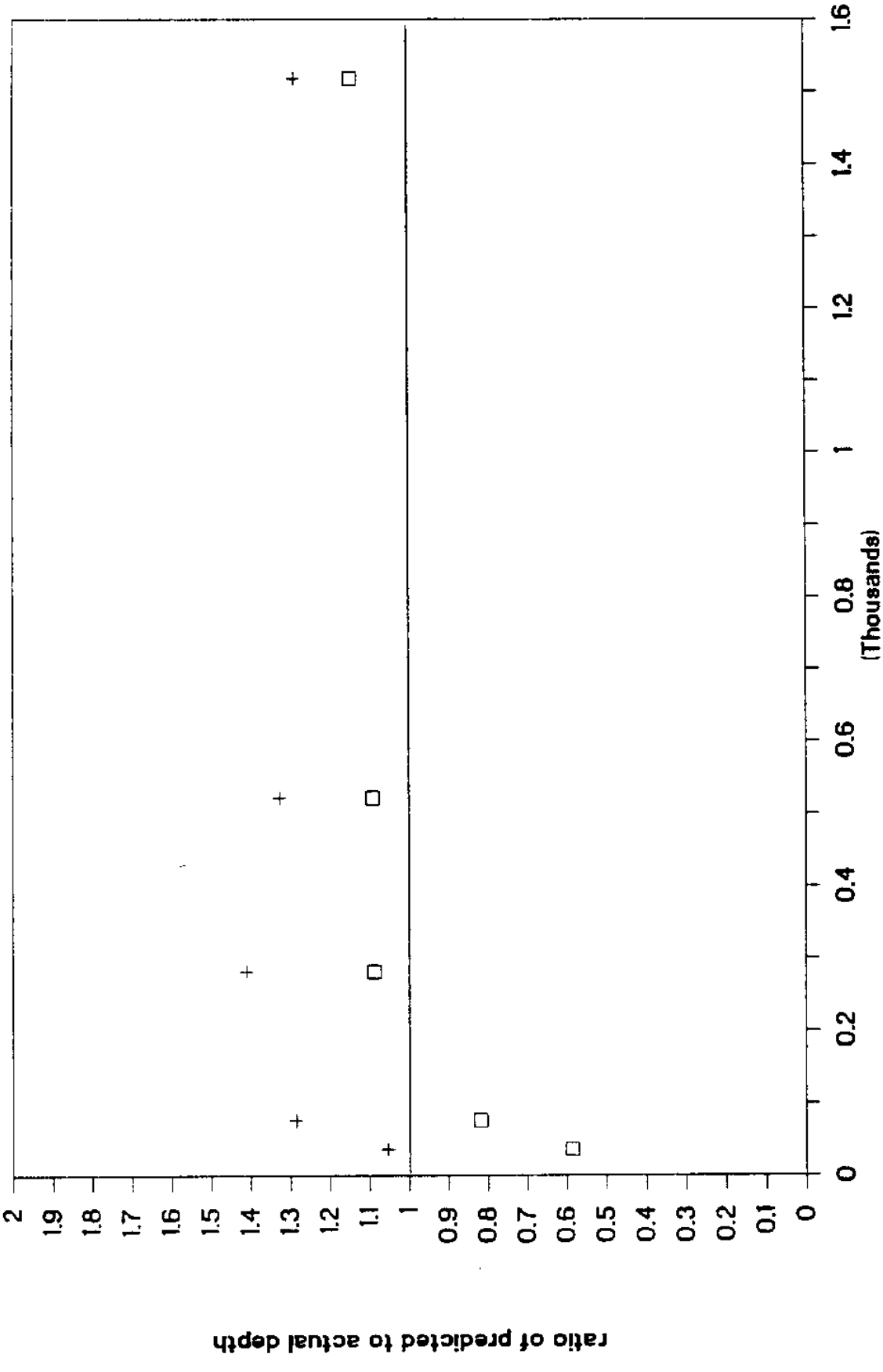

Fig. 6.11 Penetration Depth Predictions in Clay: Corrected for Strain Rate (α=0.10) & Skin Friction
(b) ratio of predicted to actual penetration depth vs. kinetic energy of the penetrator at impact

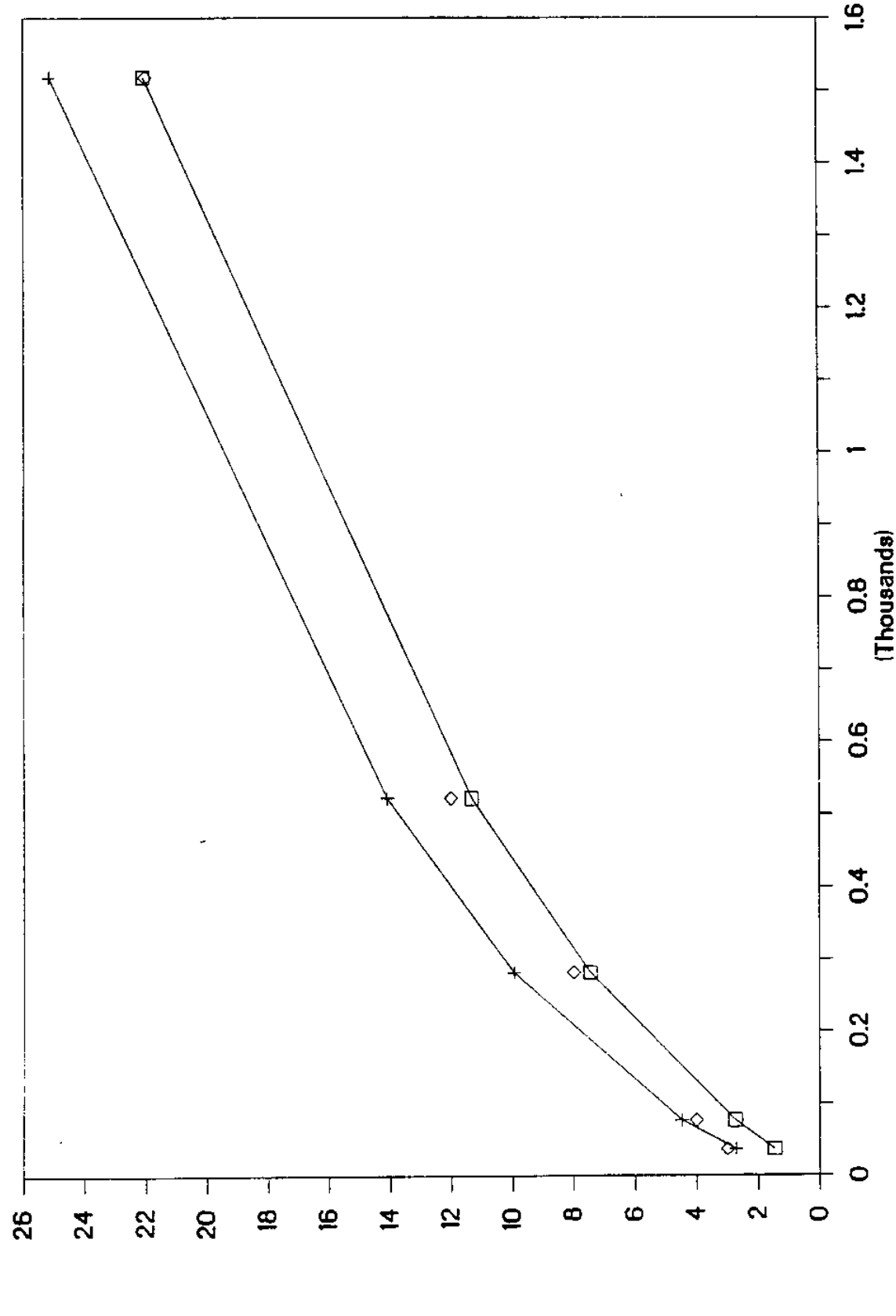

Fig. 6.12 Penetration Depth Predictions in Clay: Corrected for Strain Rate (α=0.15) & Skin Friction
(a) penetration depth vs. kinetic energy of the penetrator at impact

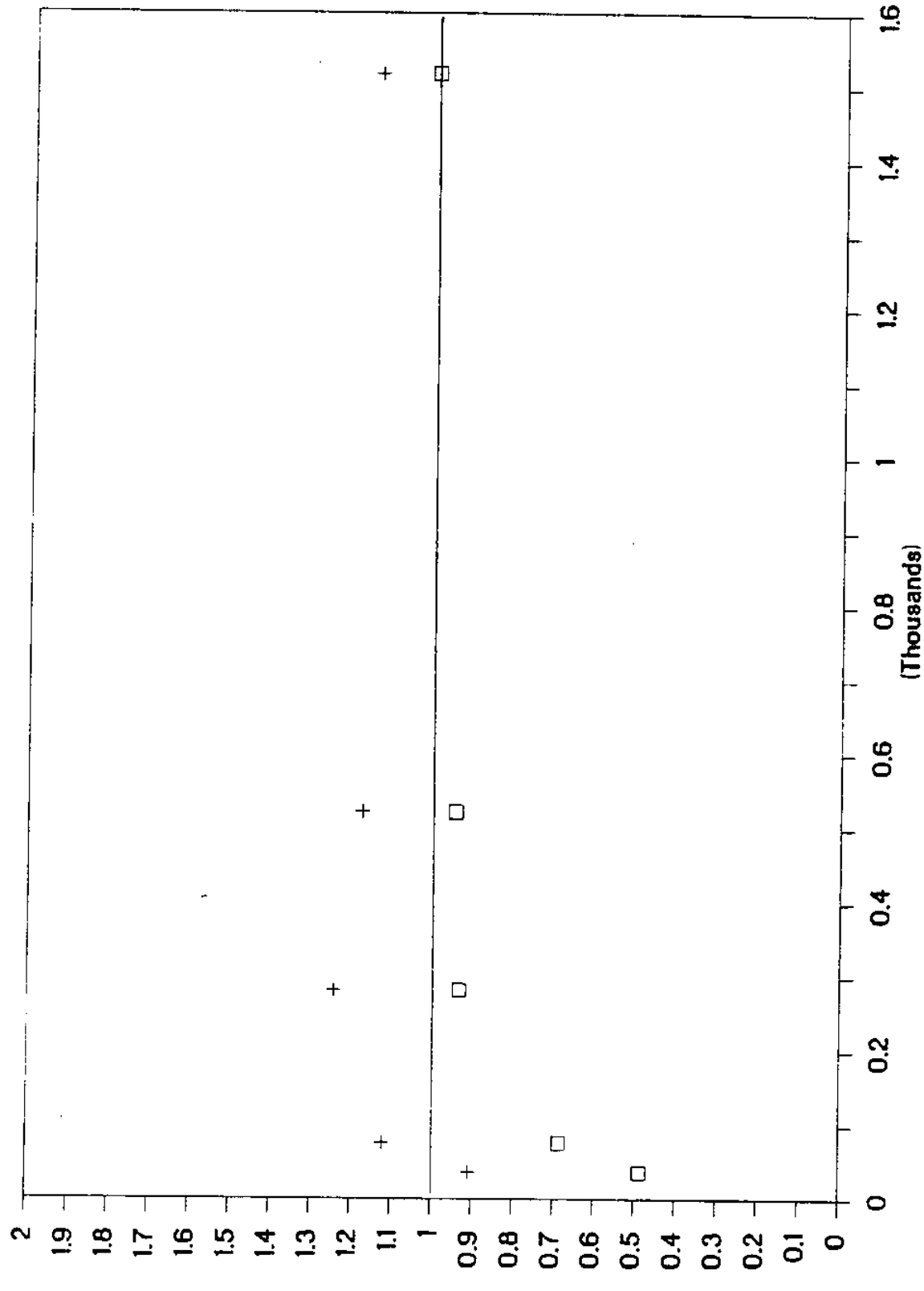

Fig. 6.12 Penetration Depth Predictions in Clay: Corrected for Strain Rate (α=0.15) & Skin Friction
(b) ratio of predicted to actual penetration depth vs. kinetic energy of the penetrator at impact

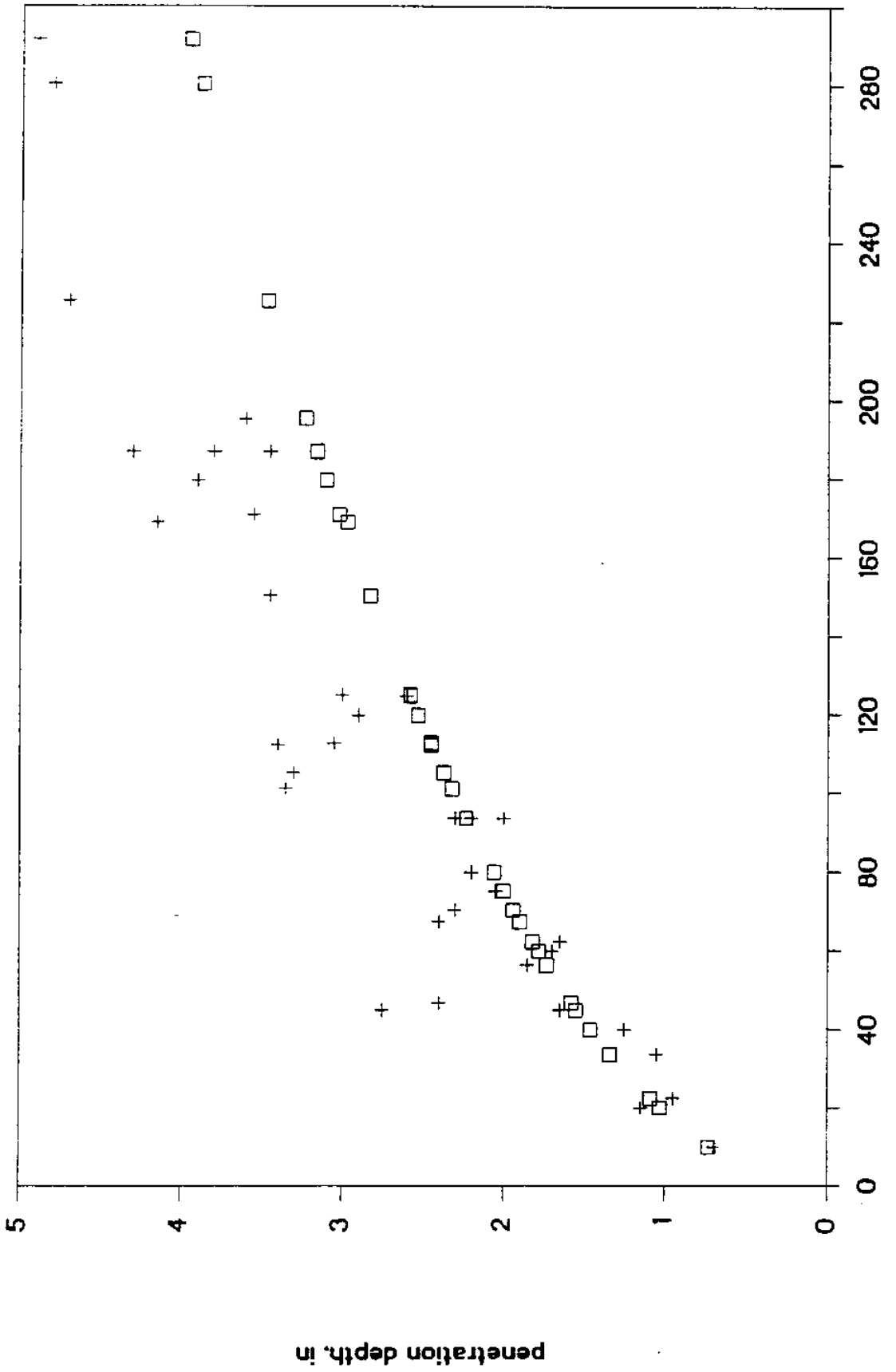

Fig. 6.13 Penetration Depth Predictions in Dense Sand: Basic Model (Point Resistance Only)
(a) penetration depth vs. penetrator kinetic energy (K.E.) at impact/cross-sectional area A

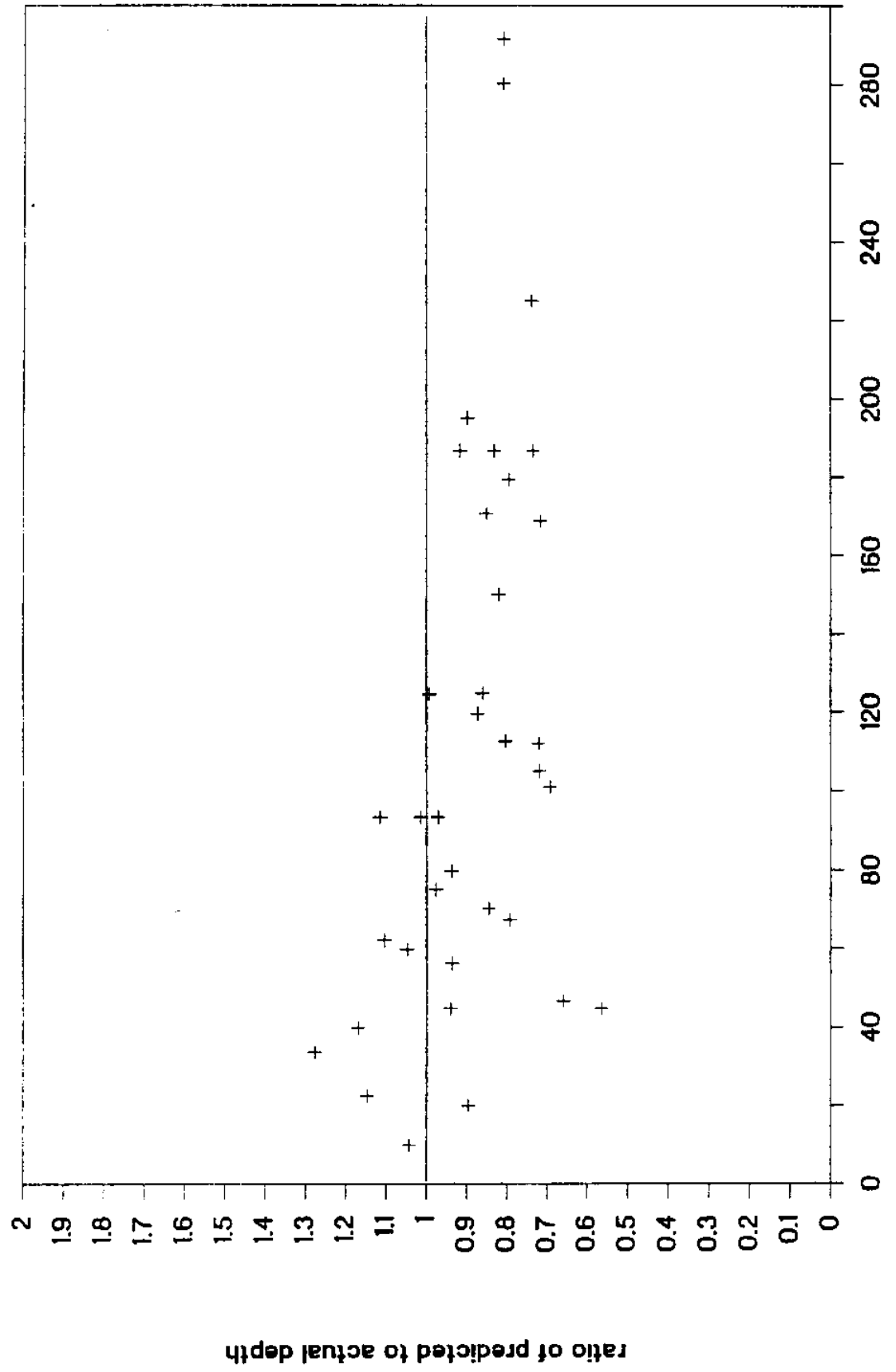

Fig. 6.13 Penetration Depth Predictions in Dense Sand: Basic Model (Point Resistance Only)
(b) ratio of predicted to actual depth vs. penetrator kinetic energy (K.E.) at impact/cross-sectional area A

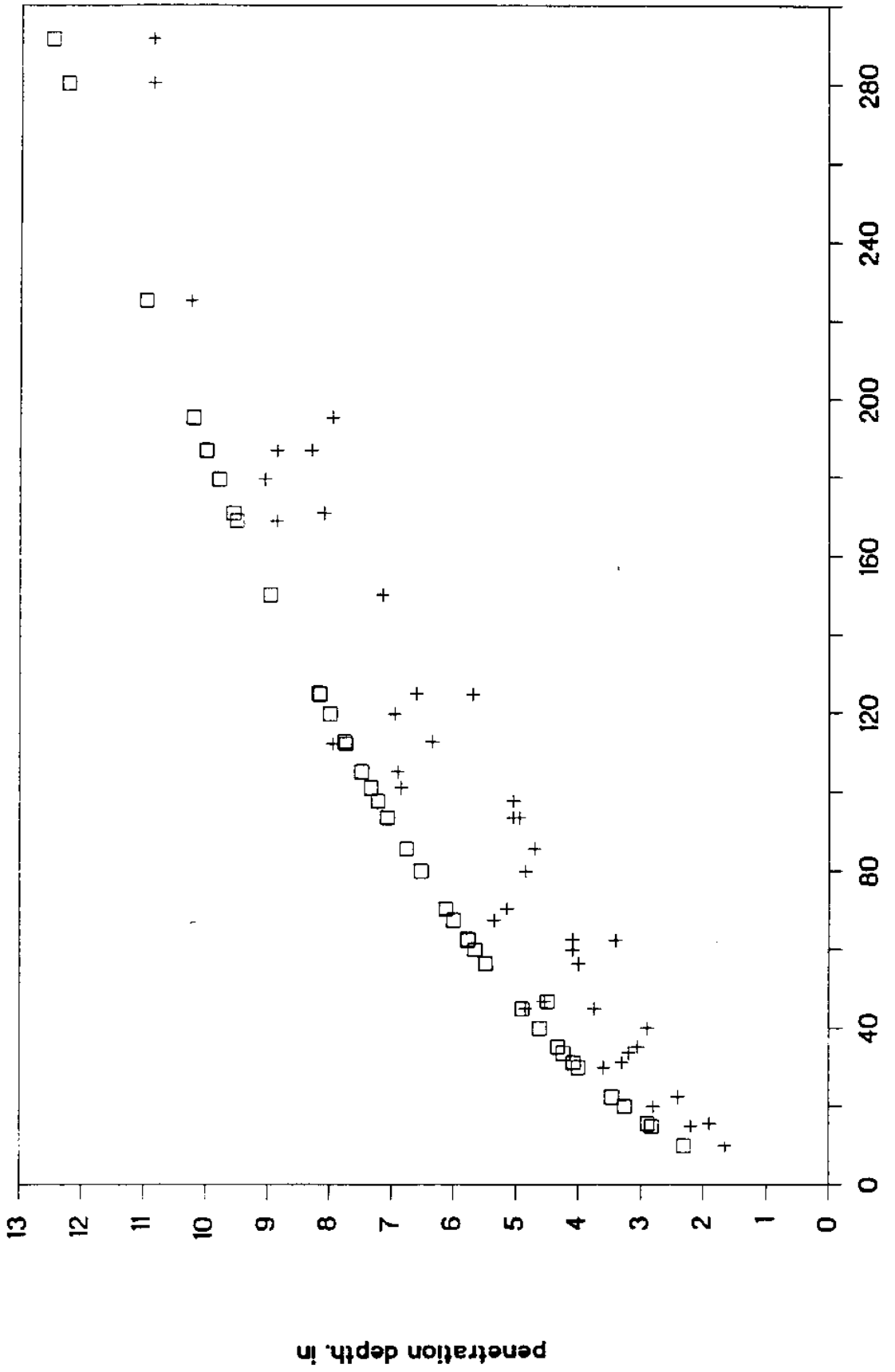

Fig. 6.14 Penetration Depth Predictions in Loose Sand: Basic Model (Point Resistance Only)
(a) penetration depth vs. penetrator kinetic energy (K.E.) at impact/cross-sectional area A

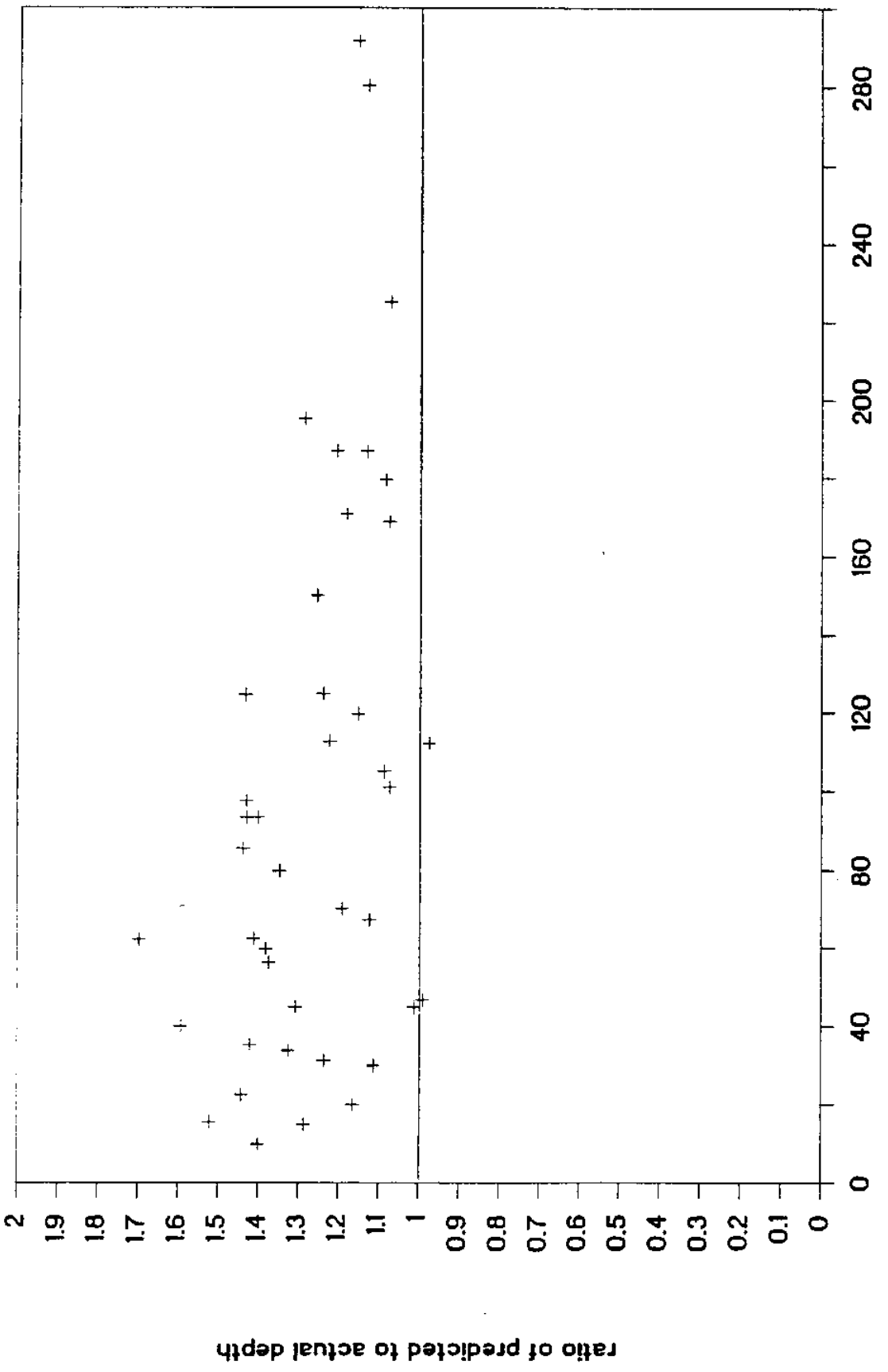

Fig. 6.14 Penetration Depth Predictions in Loose Sand: Basic Model (Point Resistance Only)
(b) ratio of predicted to actual depth vs. penetrator kinetic energy (K.E.) at impact/cross-sectional area A

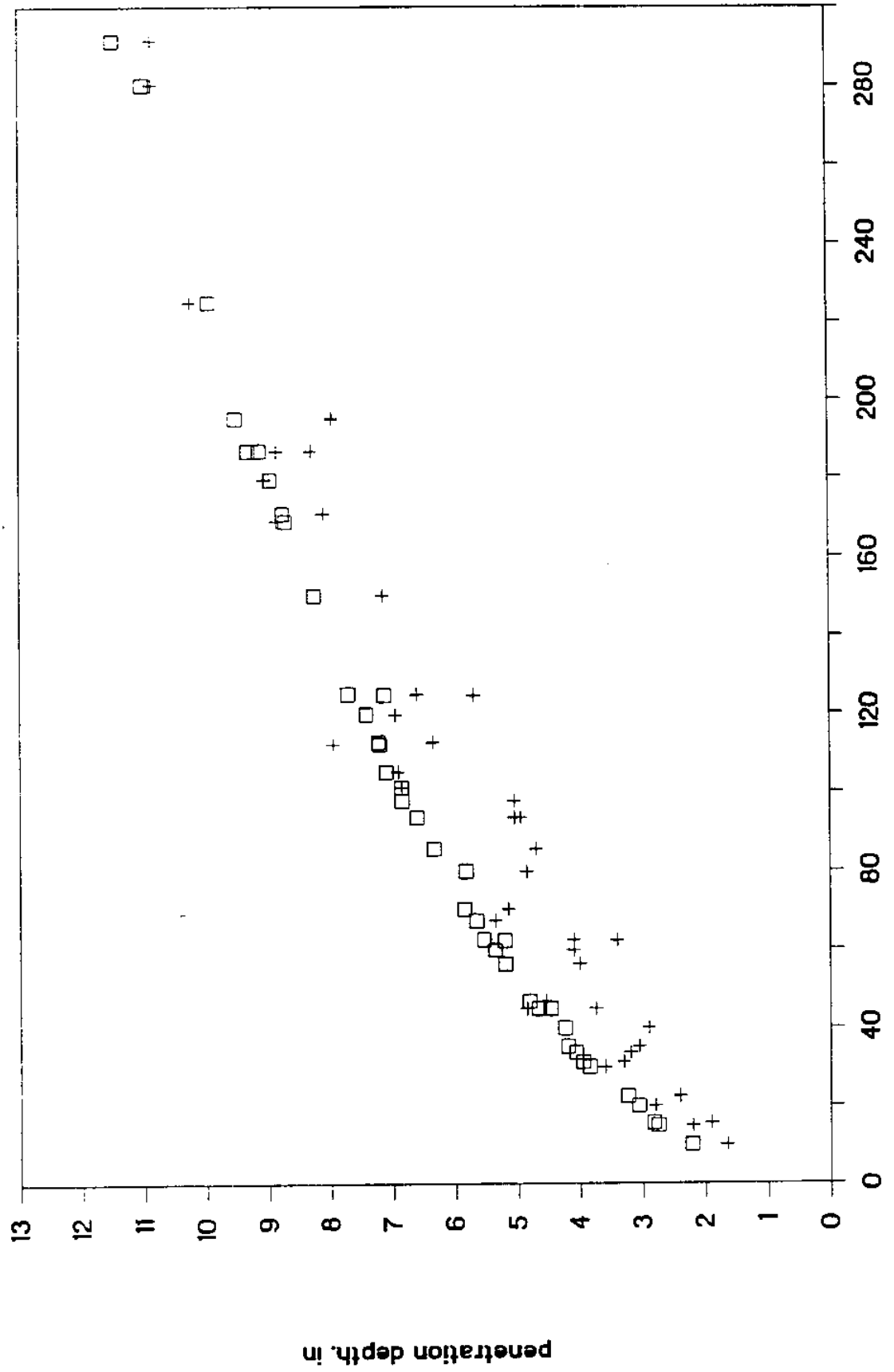

Fig. 6.15 Penetration Depth Predictions in Loose Sand: Corrected for Skin Friction
(a) penetration depth vs. penetrator kinetic energy (K.E.) at impact/cross-sectional area A

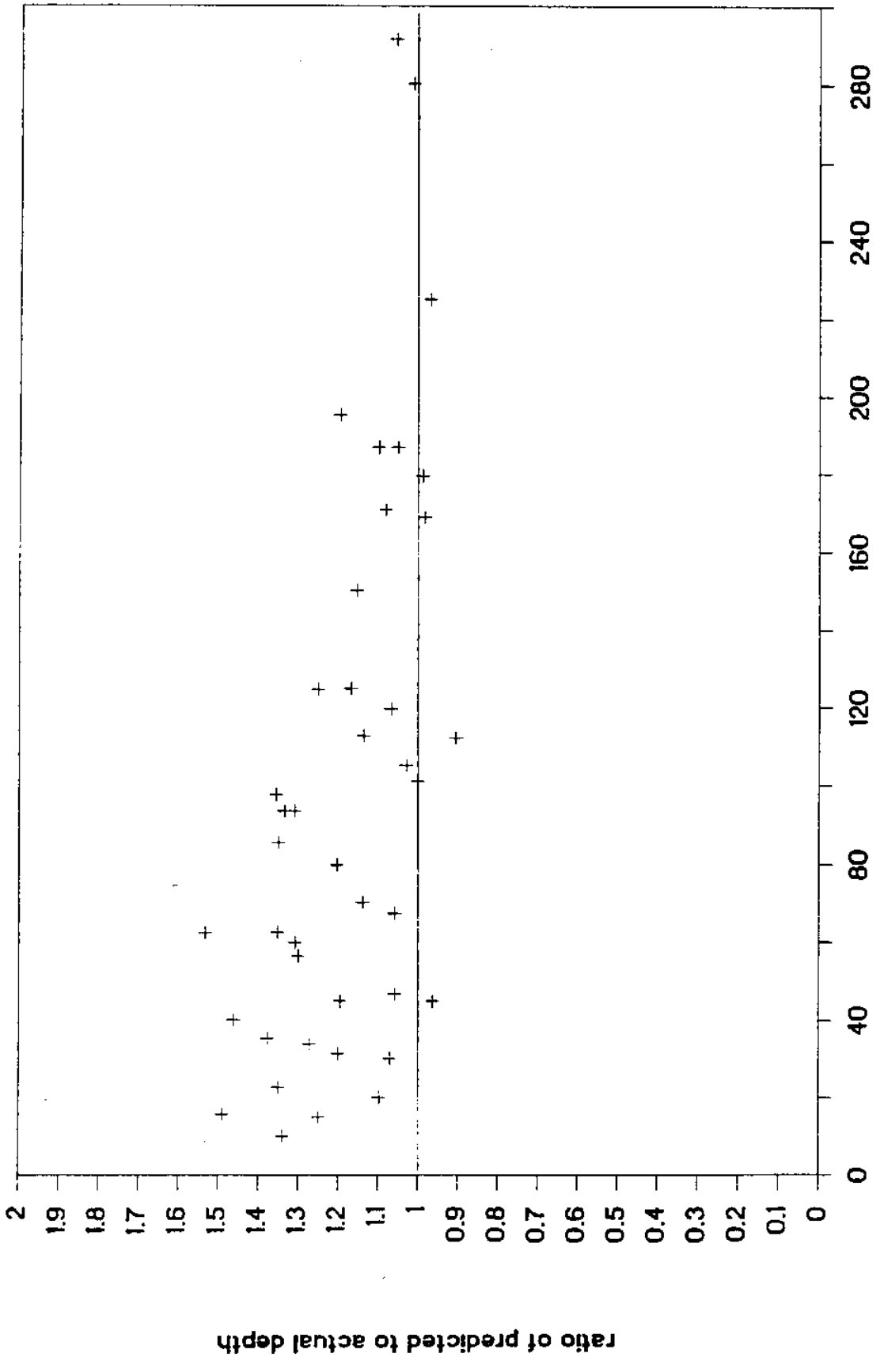

Fig. 6.15 Penetration Depth Predictions in Loose Sand: Corrected for Skin Friction
(b) ratio of predicted to actual depth vs. penetrator kinetic energy (K.E.) at impact/cross-sectional area A

CHAPTER 7
CONCLUSIONS

The 1989 research in Propellant Embedded Anchors had an experimental and an analytical modelling component.

Experimentally, we completed our initial test series with small scale (3.7 mm diameter) penetrators and 5.1 x 10.2 cm cylindrical models with varying joint spacing and consisting of gypsum or resin. Slow and rapid penetration tests as well as pullout tests were conducted. The results consisted again of observing penetration and crack pattern, of fractography, of force-displacement measurements (in the case of slow penetration and pullout) and of confining stress measurements during the entire penetration-pullout tests. The gypsum tests confirmed the results of the preceding test series while the resin tests, particularly those with a modified curing agent content showed more ductile behavior both in penetration and pullout. Also very interesting is the fact that the penetration energy during slow penetration compares well with the penetration energy during rapid penetration; it provides a reliable bound. The confining stress measurements also yielded new information. First it was conclusively shown that stresses remain locked into the medium after pullout; second, it was possible to backfigure a friction coefficient between medium and penetrator (at present with quite a bit of scatter, however).

In preparation for the validation test series to be conducted this (1990) and next year, we developed and built the testing equipment consisting of a Hilti 600N gun (donated by Hilti) instrumented with an accelerometer and of a strain gauge instrumented model as main components. The penetrator size and the model diameter were doubled, compared to the preceding test series (~6 mm and ~10 cm respectively). The initial tests, the validation tests and the tests at UC Berkeley, comprise thus a series of increasingly larger scale experiments which will provide a solid basis for checking our analytical scaling relations. The validation test equipment was calibrated and satisfactorily checked in a few shake down tests with wood and gypsum.

Our modelling effort is based on the strain path method. As stated in earlier reports, this method correctly represents the fundamental physics of penetration and can make use of standard parameters. Starting with a velocity field, a strain field is determined from which, in turn, the stress field is derived using the appropriate constitutive relations and equilibrium conditions. The advantage of the method, compared to cavity expansion approaches, is the fact that the entire two-dimensional stress field can be derived which is essential for the determination of penetration depth and pullout resistance as well as for the extension to brittle discontinua.

At the start of the PEA modelling effort, a version of the strain path method for ductile, incompressible and frictionless material existed; also initial work on a strain path based solution for ductile frictionless compressible and incompressible materials was completed (centerline stresses only). As a first step in our work, we developed the ductile frictional solutions for the complete stress field. This sets the stage for incorporation of constitutive relations for brittle continua and discontinua (i.e. intact and jointed rock). In addition, the ductile frictional solutions provide also a bound for the jointed rock. In incorporating the constitutive relations for brittle discontinua, we will make use of the MIT jointed rock model expanded by observations in the initial test series. These observations showed that the joints concentrate cracking in the intact material bounded by the joints, that the cracking intensity in the intact blocks is roughly the same, independent of joint spacing, and that cracking intensity has a substantial effect on pullout resistance.

We expect that the complete stress field computed with the strain path method will provide us with the information to predict penetration depth and pullout resistance. To make sure that the strain path based approach is reasonable for rapid penetration, for which it has not been used so far, and to have a simpler penetration prediction method, we pursued a second modelling effort during 1989. This consisted of the development of a penetration depth prediction method for ductile incompressible non-frictional and frictional materials. In this method the strain path method is used but only the point resistance is determined (not the entire stress

field). Correction factors were introduced to consider strain rate effects and interface (penetrator-medium) friction effects, which can be determined with standard laboratory tests. The results were compared to field observations reported in the literature. The comparison is satisfactory both for clay (frictionless) and sand (frictional). The goals of having a first indication that the strain path method can predict penetration depth in rapid penetration and of having a simple penetration depth prediction method have thus been achieved. We intend to extend this approach to include free surface effects, material compressibility and, possibly, brittle material properties.

With regard to publications, a paper, "Model Experiments for Propellant Embedded Anchors", on the 1988/89 initial test series has been submitted for publication in Rock Mechanics and Rock Engineering. The 1987 review of field tests by the Navy is being written up and will be coauthored by NCEL- and MIT people.

APPENDIX A

CALCULATION OF ϵ_θ AND σ_θ FROM VOLTAGE READOUTS

The circumferential strain (ϵ_θ) and stress (σ_θ) can be determined using the following equations:

$$\epsilon_\theta = \frac{\text{measured voltage (mV)}}{\text{input voltage (v)}} \text{ x } 2000 \text{ x } 10^{-6}$$

$$\sigma_\theta = E\,\epsilon_\theta$$

where E = Young's modulus = 2×10^5 MPa

For example, let the measured voltage = 0.35 mV and the input voltage = 2 V; then

$$\epsilon_\theta = \frac{0.35}{2} \times 2000 \times 10^{-6} = 350 \times 10^{-6}$$

$$\sigma_\theta = 2 \times 10^5 \text{ MPa} \times 350 \times 10^{-6} = 70 \text{ MPa}$$

APPENDIX B

DIMENSIONS AND YIELD STRAIN OF THE CLAMP

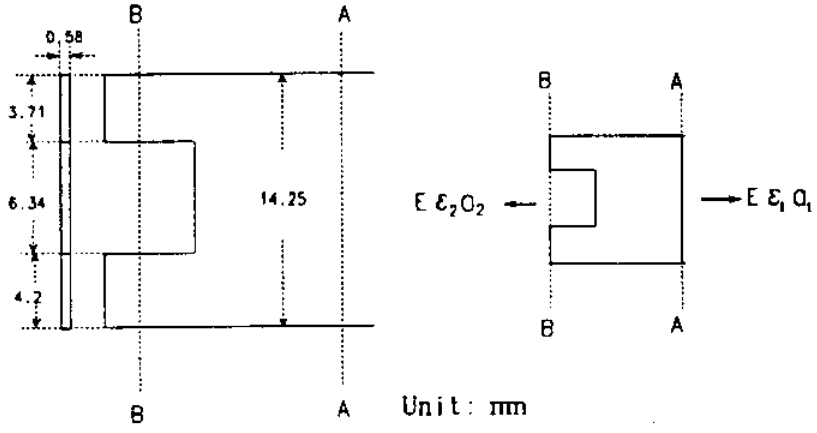

The areas at cross section AA and BB are:

$$A_{\text{cross section AA}} = 14.25 \times 0.58 = 8.265 \times 10^{-6}\ m^2 = a_1$$

$$A_{\text{cross section BB}} = (3.71 + 4.2) \times 0.58 = 4.588 \times 10^{-6}\ m^2 = a_2$$

$$\frac{a_2}{a_1} = 0.555$$

The yield strain of stainless steel is 0.2 %.

The forces acting on cross section BB and AA are equal such that:

$E\ \epsilon_1\ a_1 = E\ \epsilon_2\ a_2$, where ϵ_1 and ϵ_2 are the hoop strains at AA and BB, respectively.

When ϵ_2 reaches its yield limit (0.2 %), ϵ_1 becomes

$$\epsilon_1 = \epsilon_2 \frac{a_2}{a_1} = 0.2\ \%\ X\ 0.555 = 0.111\ \%$$

That is, if ϵ_0 at cross section AA is greater than 0.11 %, then yielding must have occurred.

APPENDIX C
DETAILS OF THE STRAIN PATH METHOD AND ITS APPLICATION TO PENETRATION PREDICTION

Appendix C.1
The Strain Path Method for the Simple Pile: Penetration in Incompressible Cohesive Materials (Clays) (Baligh 1985a, b)

The Strain Path Method is an approximate analytical technique developed by Baligh (1985a, b) to describe fundamental mechanisms of deep penetration in soil. It is assumed that due to the severe kinematic constraints related to deep penetration problems, deformations and strains are essentially independent of the shearing resistance of the soil. Therefore, deep penetration problems are considered to be strain-controlled and deformations and strains can be determined with reasonable accuracy based only on kinematic considerations and boundary conditions. Deviatoric (shear) stresses can then be determined in an approximate way by assuming a constitutive model and finally octahedral stresses are solved by imposing equilibrium. The steps in applying the Strain Path Method to steady deep penetration in incompressible cohesive materials by the simple pile are given in the following sections. Initially, one estimates the velocity field in the target due to penetration by the simple pile at a constant velocity. This is done by using the solution for a spherical source in an ideal fluid in uniform flow.

1. Velocity Field

Consider a single spherical source located at r = 0 in a spherical coordinate system (Fig. C.1(a)) emitting volume V per unit time. The radius of the spherical cavity after a time t will be given by:

$$V_t = \frac{4}{3}\pi R^3 \qquad (1a)$$

$$R = \left[\frac{3}{4\pi} V_t\right]^{1/3} \qquad (1b)$$

If we expand such a cavity in the soil at the rate V, an element A originally located a distance ρ_o from the center of the cavity (origin) would be displaced according to the following conservation of volume equation:

$$\frac{4}{3}\pi\rho^3 = \frac{4}{3}\pi\rho_o^3 + \frac{4}{3}\pi R^3 \qquad (2a)$$

where ρ = new distance of element A from the origin.
Solving for $\rho(t)$:

$$\rho(t) = \left[\rho_o^3 + R^3(t)\right]^{1/3} \qquad (2b)$$

Differentiating $\rho(t)$ with time will give us the radial velocity v_ρ of the particles in the medium

$$v_\rho = \frac{d\rho}{dt} = \frac{1}{3}\left[\rho_o^3 + R^3(t)\right]^{-2/3}\frac{d(R^3)}{dt} \qquad (3a)$$

$$v_\rho = \frac{V}{4\pi}\frac{1}{\rho^2} \qquad (3b)$$

In the cylindrical coordinate system (Fig. C.1(b)), the velocity components are given by:

radial: $$v_r = \frac{V}{4\pi}\frac{\sin\phi}{\rho^2} \qquad (4)$$

vertical: $$v_z = \frac{V}{4\pi}\frac{\cos\phi}{\rho^2}$$

where $\rho^2 = r^2 + z^2$

ϕ = arctan (r/z)

For a single spherical source in a uniform flow field with velocity U in the z-direction (Fig. C.2), the soil particle velocity components are given by:

$$v_r = v_r^o$$
$$v_z = U + v_z^o \tag{5}$$

where v_r^o and v_z^o correspond to the point source solution given by Eq. (4).

2. Soil Deformations

In the cylindrical coordinate system, the velocity components v_r and v_z in terms of the stream function ψ are given by:

$$v_r = \frac{1}{r}\frac{\partial \psi}{\partial z}$$
$$v_z = -\frac{1}{r}\frac{\partial \psi}{\partial r} \tag{6}$$

Integrating the above equations for ψ, using Eq. (5) and (4)

$$\psi = \frac{V}{4\pi}\cos\phi - \frac{r^2}{2}U \tag{7}$$

The rate of volume discharge V can be related to the area of the cylindrical cavity and velocity of penetration U:

$$V = (\pi R^2)U$$
$$R = \sqrt{\frac{V}{\pi U}} \tag{8}$$

Therefore ψ can be expressed as:

$$\psi = \frac{R^2 U}{4}\cos\phi - \frac{r^2 U}{2} \tag{9}$$

To arrive at the expression for the deformation of soil particles, we make use of the property of the streamline: ψ = constant. Thus, for any given streamline, the value of ψ in the far field equals its value in the near field:

$$\psi_{\substack{\text{far field} \\ (r = r_o \\ \phi = -\pi)}} = \psi_{\substack{\text{near field} \\ (r = r \\ \phi = \phi)}} \tag{10}$$

This gives us the streamline or path of any particle originally located at a distance r_o:

$$\left(\frac{r}{R}\right)^2 = \left(\frac{r_o}{R}\right)^2 + \frac{1}{2}(1 + \cos\phi) \tag{11a}$$

When $r_o = 0$, corresponding to soil elements initially located at the centerline, Eq. (11) yields the analytical expression for the geometry of the simple pile:

$$\left(\frac{r}{R}\right)^2 = \frac{1}{2}(1 + \cos\phi) \tag{11b}$$

Thus, the simple pile as given by Eq. (11b) has the following characteristics (Fig. C.3):

1. The tip is located at z=-R/2.
2. The parameter R actually represents the radius of the simple pile at sufficiently large distance behind the tip.
3. Theoretically, the radius of the simple pile increases indefinitely but for all practical purposes, it can be assumed to have a uniform radius equal to R from point C in Fig. C.3 located 4R behind the tip.

Although seemingly complicated and apparently not very practical, the simple pile geometry was selected in order to simplify the generation and presentation of solutions and hence address the fundamental mechanism of penetration without cumbersome

numerical details. The geometry of the simple pile guarantees the absence of a relative normal velocity of the soil-pile interface (i.e., the soil particle velocities are in the tangential direction with respect to the pile surface).

3. Strain Rates

The nonvanishing components of strain rates in axisymmetric penetration in an infinite medium are three normal strain rates (positive when compressive):

$$\begin{aligned} \dot{\varepsilon}_{rr} &= -\frac{\partial v_r}{\partial r} \\ \dot{\varepsilon}_{zz} &= -\frac{\partial v_z}{\partial z} \\ \dot{\varepsilon}_{\theta\theta} &= -\frac{v_r}{r} \end{aligned} \tag{12a}$$

and one (tensorial) shearing strain rate

$$\dot{\varepsilon}_{rz} = -\tfrac{1}{2}\left(\frac{\partial v_r}{\partial z} + \frac{\partial v_z}{\partial r}\right) \tag{12b}$$

where v_r and v_z are positive in the positive r and z directions. Carrying out the differentiation using Eq. (5):

$$\begin{aligned} \dot{\varepsilon}_{rr} &= -\frac{UR^2}{4\rho^3}A_{rr}(\phi) \\ \dot{\varepsilon}_{zz} &= -\frac{UR^2}{4\rho^3}A_{zz}(\phi) \\ \dot{\varepsilon}_{\theta\theta} &= -\frac{UR^2}{4\rho^3} \\ \dot{\varepsilon}_{rz} &= -\frac{UR^2}{4\rho^3}A_{rz}(\phi) \end{aligned} \tag{13}$$

where $A_{rr}(\phi) = \cos^2\phi - 2\sin^2\phi$

$A_{zz}(\phi) = \sin^2\phi - 2\cos^2\phi$

$A_{rz}(\phi) = -3/2 \sin(2\phi)$

$\phi = \arctan(r/z)$

$\rho = r/\sin\phi$

In view of the assumed incompressibility of the soil, the sum of the three normal strain rates vanishes and only three components are sufficient to fully describe the sets of change in soil strains. The three deviatoric strain rate components $\dot{E}_i$ ($\dot{E}_1$, $\dot{E}_2$, $\dot{E}_3$) defined by the expressions:

$$\begin{aligned} \dot{E}_1 &= \dot{\varepsilon}_{zz} \\ \dot{E}_2 &= \frac{1}{\sqrt{3}}(\dot{\varepsilon}_{rr} - \dot{\varepsilon}_{\theta\theta}) \\ \dot{E}_3 &= \frac{2}{\sqrt{3}}\dot{\varepsilon}_{rz} \end{aligned} \qquad (14)$$

are convenient because they provide a clear picture of the shearing modes of the soil in axisymmetric problems. Under idealized testing conditions, conventional triaxial tests impose $\dot{E}_1$ type of straining rates and $\dot{E}_2 = \dot{E}_3 = 0$; pressuremeter tests or cylindrical cavity expansion apply $\dot{E}_2$, and simple shear tests impose $\dot{E}_3$, modes of shearing. Furthermore, the deviatoric strain rates $\dot{E}_i$ have an equal relative effect on the second invariant of the deviatoric strain rates, $\dot{E}$ (where $\dot{E}^2 = \frac{1}{3}\dot{\varepsilon}_{ij}\dot{\varepsilon}_{ij}$):

$$\dot{E} = \frac{1}{\sqrt{2}}\left[\dot{E}_1^2 + \dot{E}_2^2 + \dot{E}_3^2\right]^{1/2} \qquad (15)$$

Combining Eq. (14) and Eq. (13) and substituting in Eq. (15):

$$\dot{E} = \frac{UR^2}{2\sqrt{2}} \frac{1}{\rho^3} \qquad (16)$$

where $\rho = (r^2 + z^2)^{1/2}$

4. Strain Paths

4.1 Strain Paths Close to the Pile

For soil elements close to the pile, the deviatoric strain paths are shown in Fig C.4; they were obtained by numerical integration taking into consideration changes in geometry. The strain paths indicate that:

1. The straining levels close to the pile are much greater than normally imposed in common laboratory and pressuremeter tests as illustrated by the shaded zones in Fig. C.4. Therefore, the post-peak behavior of the clay should be expected to have an important effect on stresses and pore pressures in the soil close to the pile.
2. Ahead of the pile, straining of the soil located near the axis takes place essentially due to E_1 (vertical compression) with possibly some contribution of E_3 well before E_2 (cylindrical expansion) is felt.
3. In reaching the final state of strain behind the tip (i.e., at large values of z), the strain components of a soil element exhibit significant reversals (The reversal of strain paths and the high straining levels caused by penetration have a major influence on stress predictions).

4.2 Far Field Strains

At sufficiently large distances from the pile, changes in soil geometry may be neglected, streamlines become approximately vertical and hence any strain rate component such as ε_{zz} can be expressed as:

$$\dot{\varepsilon}_{zz} = \frac{d\varepsilon_{zz}}{dt} \cong U \cdot \frac{d\varepsilon_{zz}}{dz} \qquad (17)$$

where $$\frac{d\varepsilon_{zz}}{dz} = \frac{d\varepsilon_{zz}}{d\phi} \cdot \frac{d\phi}{dz} \qquad (18)$$

Therefore, integrating Eq. (17) using Eq. (13) and (18) gives us ε_{zz}. The other strain rate components are determined similarly. Thus, the cylindrical strain components in the far field are given by:

$$\begin{aligned}
\varepsilon_{rr} &= \left(\frac{R}{2r}\right)^2 B_{rr}(\phi) \\
\varepsilon_{zz} &= \left(\frac{R}{2r}\right)^2 B_{zz}(\phi) \\
\varepsilon_{\theta\theta} &= \left(\frac{R}{2r}\right)^2 B_{\theta\theta}(\phi) \\
\varepsilon_{rz} &= \left(\frac{R}{2r}\right)^2 B_{rz}(\phi)
\end{aligned} \qquad (19)$$

where $B_{rr}(\phi) = 1+\cos\phi(1+\sin^2\phi)$
$B_{zz}(\phi) = -\cos\phi\sin^2\phi$
$B_{\theta\theta}(\phi) = -(1+\cos\phi)$
$B_{rz}(\phi) = -\sin^3\phi$

Defining the deviatoric strain components E_i (E_1, E_2, E_3) by the expressions:

$$\begin{aligned}
E_1 &= \varepsilon_{zz} \\
E_2 &= \tfrac{1}{\sqrt{3}}(\varepsilon_{rr} - \varepsilon_{\theta\theta}) \\
E_3 &= \tfrac{2}{\sqrt{3}}\varepsilon_{rz}
\end{aligned} \qquad (20)$$

closed form expressions for the deviatoric strain components E_i in the far field can be determined by direct substitution of Eq. (19) into Eq. (20).

The second invariant of the deviatoric strains E ($E^2=\frac{1}{3}E_{ij}E_{ij}$) is of special significance for isotropic yielding of the von Mises type. In axisymmetric problems

$$E=\frac{1}{\sqrt{2}}[E_1^2 + E_2^2 + E_3^2]^{1/2} \qquad (21)$$

Eq. (21), (20) and (19) indicate that in the far field, where changes in geometry can be neglected, E is given by the expression

$$E = \left(\frac{R}{r}\right)^2\left[\frac{1+\cos\phi}{24}(1+\cos\phi+\sin^2\phi)\right]^{\frac{1}{2}} \qquad (22)$$

The elastic-plastic boundary, where $E=E_y$, would be defined, using Eq. (22), as

$$r = R\frac{1}{\sqrt{E_y}}\left[\frac{1+\cos\phi}{24}(1+\cos\phi+\sin^2\phi)\right]^{\frac{1}{4}} \qquad (23)$$

Eq. (22) describes the geometry of the contour lines E=constant in the far field as shown in Fig. C.5(b). Results in Fig. C.5(b) also show contour lines of E close to the pile, obtained by numerical integration after incorporating changes in geometry. Fig. C.5(a) presents spherical contour lines of $\dot{E}$ in the case of a simple pile with radius R=1.78 cm penetrating at a velocity U=2 cm/sec as in standard cone penetration testing.

5. Constitutive Model (The Prandtl-Reuss Bilinear Model) and Shear Stresses

The Prandtl-Reuss (P-R) total stress model (Fig. C.6) is the simplest yet relevant model of deviatoric behavior. The Prandtl-Reuss material is assumed to be incompressible, isotropic, inviscid and linearly elastic prior to yield. Moreover, it obeys the von Mises yield criterion, exhibits no strain hardening or softening during plastic flow (i.e., it is perfectly plastic) and follows an associated flow rule.

For axisymmetric problems, the stress-strain relationships are given by the following:

$$S^2 = \frac{2}{3}k^2 \qquad (24)$$

where k is a measure of the undrained shear strength of the soil and the second invariant of the deviatoric stress state S ($S^2=\frac{1}{3}S_{ij}S_{ij}$) is given by

$$S = \frac{\sqrt{2}}{3}\left[S_1^{\,2} + S_2^{\,2} + S_3^{\,2}\right]^{\frac{1}{2}}; \qquad S \geq 0 \qquad (25)$$

where the deviatoric (shear) stress components S_i are defined by

$$\begin{aligned} S_1 &= \sigma_{zz} - \tfrac{1}{2}(\sigma_{rr} + \sigma_{\theta\theta}) \\ S_2 &= \tfrac{\sqrt{3}}{2}(\sigma_{rr} - \sigma_{\theta\theta}) \\ S_3 &= \sqrt{3}\,\sigma_{rz} \end{aligned} \qquad (26)$$

where σ_{zz}, σ_{rr}, $\sigma_{\theta\theta}$, σ_{rz} are the vertical, radial, tangential (or hoop), and meridional shear stress components in a cylindrical frame, respectively. The stress-strain relationships for a P-R material actually describe a bilinear shear behavior given by the following expressions:

in the elastic range: $$E_i = \frac{S_i}{3G}; \quad i=1,2,3 \quad \text{and} \quad E = \frac{S}{2G} \qquad (27)$$

in the plastic range: $$\dot{E}_i = \frac{\dot{S}_i}{3G} + \sqrt{\frac{2}{3}}\frac{\dot{E}}{k}S_i; \quad i=1,2,3 \qquad (28)$$

where G is the (undrained) shear modulus of the soil and the deviatoric strain rate $\dot{E}$ during simple pile penetration is given by Eq. (16).

A description of the undrained clay behavior by means of the P-R bilinear model requires estimates of the shear strength

parameter k and the shear stiffness G. Setting $S_1=S_2=0$ in Eq. (24) to (26), the strength parameter k equals $s_u(DSS)$ where $s_u(DSS)$ is the undrained shear strength (maximum value of σ_{rz}) of the clay in direct simple shearing. Alternatively, according to the P-R model, $k = \frac{2s_u(T)}{\sqrt{3}}$ where $s_u(T)$ represents the undrained shear strengths in either triaxial compression or extension tests ($s_u = \frac{1}{2}|\sigma_v - \sigma_h|$ at peak resistance).

The most significant model limitations in the P-R material when simulating real undrained behavior of clays are believed to be: 1) clay behavior is nonlinear at small strain levels, 2) clay may be anisotropic and exhibit strain softening especially for anisotropically consolidated clays and 3) rate effects are neglected by the model.

6. Equilibrium and Octahedral Stresses

After determining the deviatoric (shear) stresses by means of a constitutive soil model, the octahedral stresses can now be determined by considering equilibrium.

Octahedral stresses σ during undrained penetration must satisfy equilibrium. For our problem of vertical axisymmetric penetration, the stress components in the cylindrical frame can be written in terms of σ and the deviatoric deviatoric stresses S_i:

$$\begin{aligned} S_1 &= \sigma_{zz} - \tfrac{1}{2}(\sigma_{rr} + \sigma_{\theta\theta}) \\ S_2 &= \tfrac{\sqrt{3}}{2}(\sigma_{rr} - \sigma_{\theta\theta}) \\ \sigma_{\theta\theta} &= -\tfrac{1}{3}\left(\sqrt{3}S_2 - S_1\right) + \sigma \\ \sigma_{rz} &= \tfrac{1}{\sqrt{3}}S_3 \end{aligned} \qquad (29)$$

where $$\sigma = \tfrac{1}{3}(\sigma_{rr} + \sigma_{\theta\theta} + \sigma_{zz}) \qquad (30)$$

For deep penetration, the magnitude of changes in stresses in the soil around the tip due to its weight are negligible (i.e., body

forces are small compared to stress gradients). Equilibrium can thus expressed in terms of σ and S_i.

In the radial direction,

$$\frac{\partial \sigma}{\partial r} = g_r; \qquad g_r = -\frac{1}{\sqrt{3}}\left[\frac{\partial}{\partial r}\left(S_2 - \frac{S_1}{\sqrt{3}}\right) + \frac{\partial S_3}{\partial z} + \frac{2S_2}{r}\right] \tag{31}$$

In the vertical direction,

$$\frac{\partial \sigma}{\partial z} = g_z; \qquad g_z = -\frac{1}{\sqrt{3}}\left[\frac{\partial S_3}{\partial r} + \frac{2}{\sqrt{3}}\frac{\partial S_1}{\partial z} + \frac{S_3}{r}\right] \tag{32}$$

For sufficiently smooth stress fields, differentiation of Eq. (31) and (32) indicates that equilibrium also requires that σ satisfies the Poisson equation:

$$\nabla^2 \sigma = g; \qquad g = \frac{1}{r}\frac{\partial}{\partial r}(r g_r) + \frac{\partial g_z}{\partial z} \tag{33}$$

Therefore, given the deviatoric stress S_i, the octahedral stress σ can be computed in a number of ways. One approach consists of integrating Eq. (31) along radial lines (z=constant) from infinity where $\sigma=\sigma_0$, the initial octahedral stress in the soil, to any radial distance r. Alternatively, σ can be calculated from Eq. (32) by integration along vertical lines or from both Eq. (31) and (32) along any integration path; or by solving Eq. (33). In case of exact solutions, all approaches lead to unique values of σ independent of the integration path. In approximate solutions like the Strain Path Method (where the strain field is assumed to be independent of the constitutive behavior of the material), g_r and g_z do not satisfy Eq. (33) everywhere in the soil. Discrepancies between σ values estimated on the basis of Eq. (31), (32) and (33) represent a measure of sensitivity to analytic simplification and an index for the reliability of S_i at various locations around the penetrating pile.

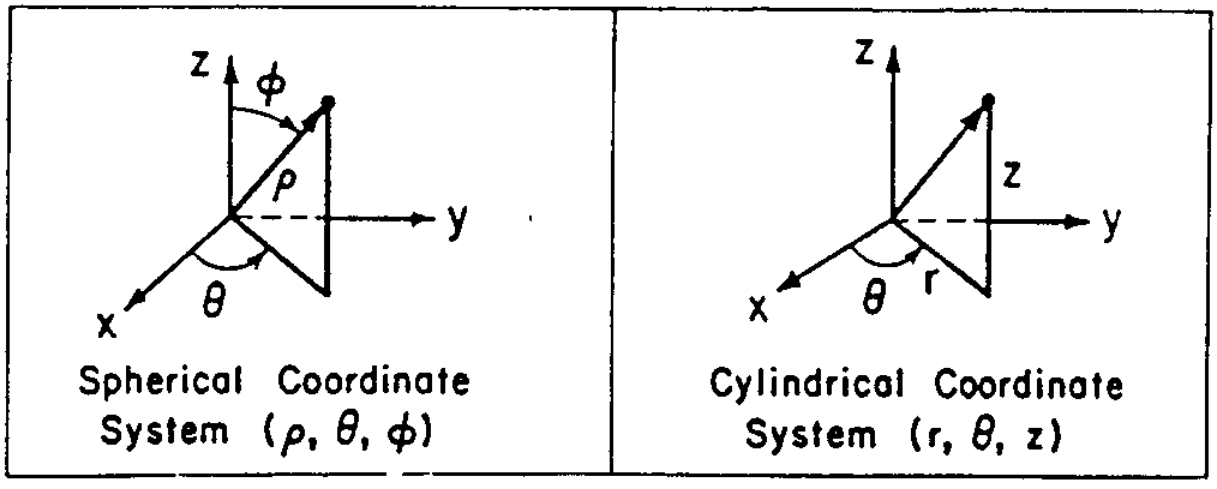

Fig. C.1 Spherical and Cylindrical Coordinate Systems

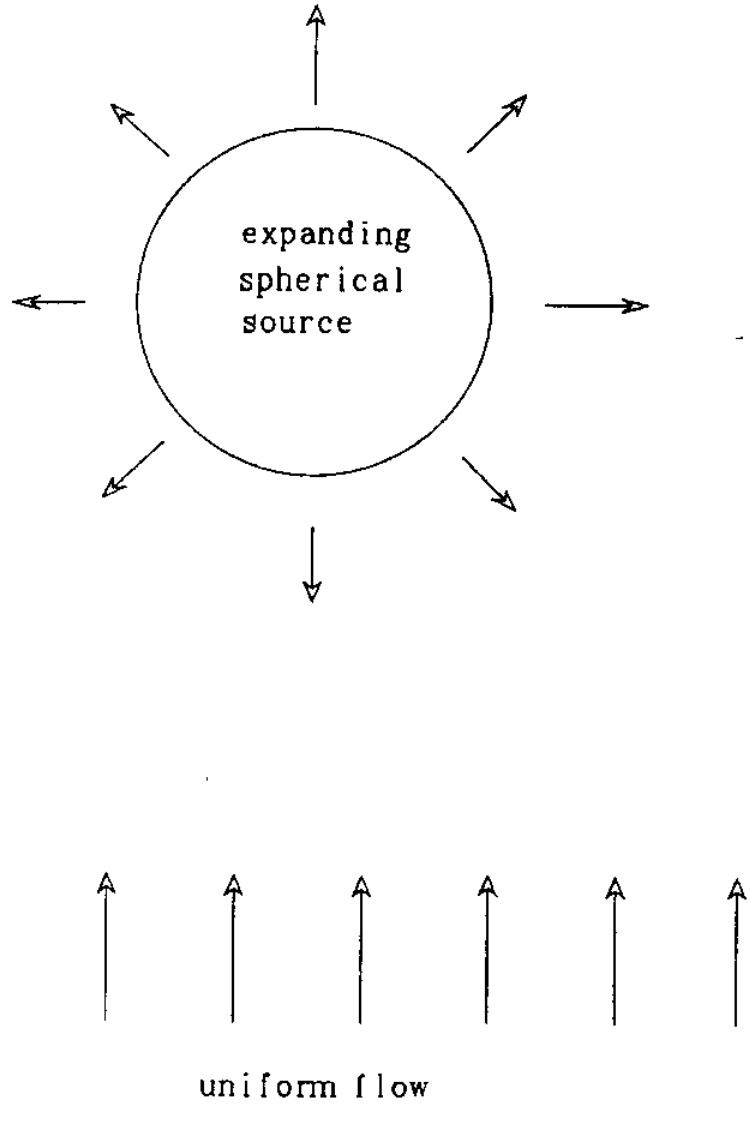

Fig. C.2 A spherical source in an ideal fluid in uniform flow

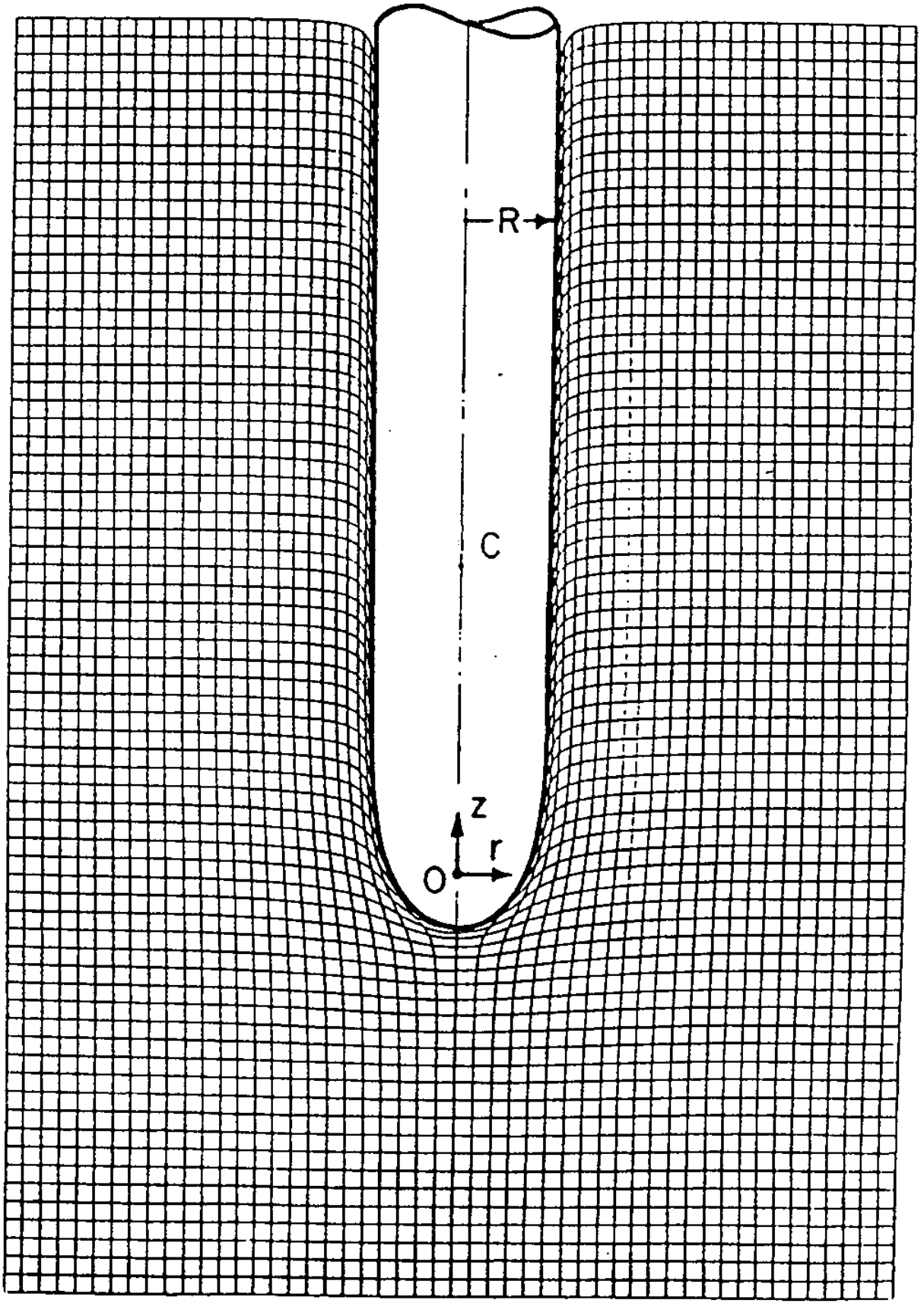

Fig. C.3 Shear Deformations in Saturated Clay: Simple Pile Penetration (after Baligh 1985a)

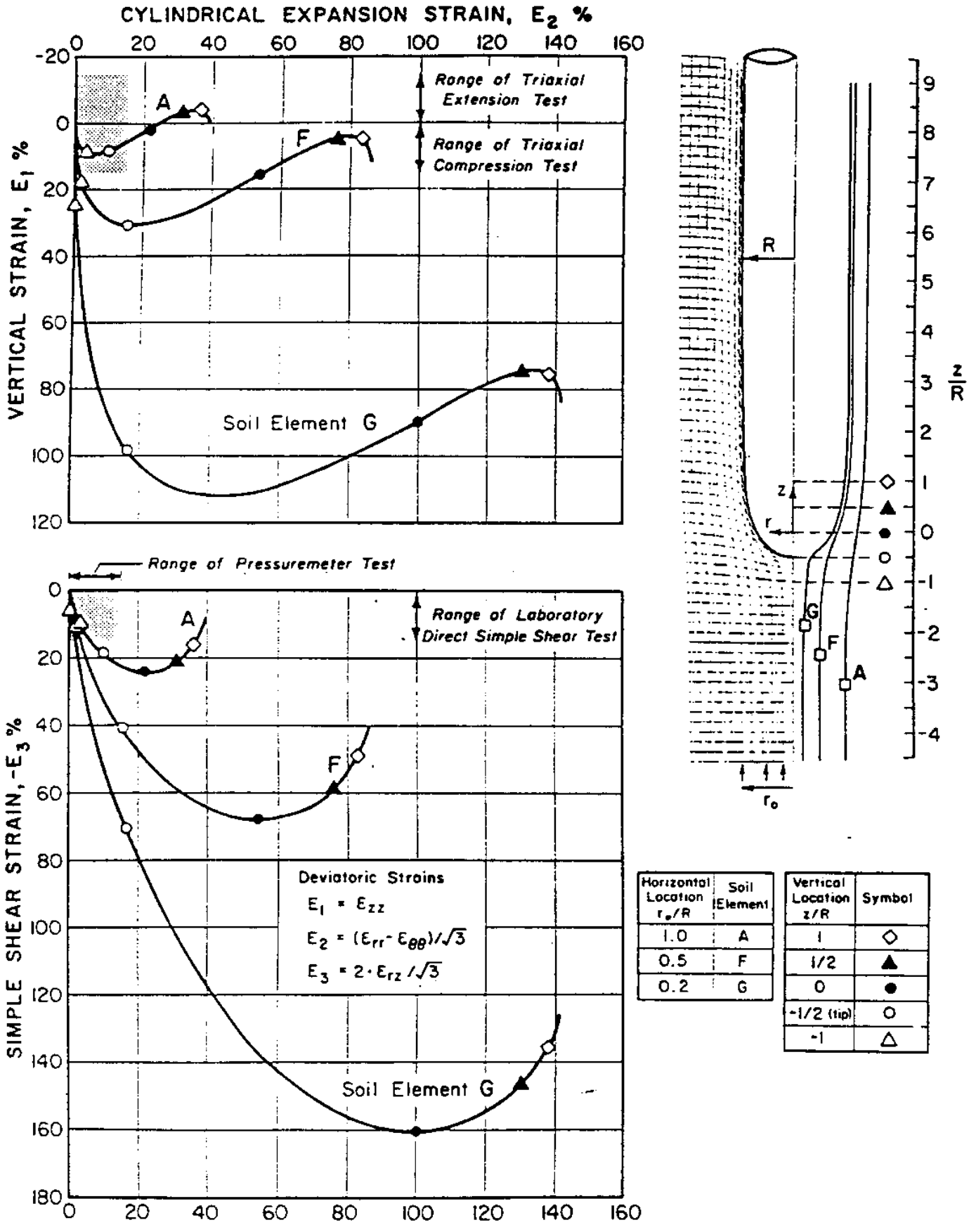

Fig. C.4 Strain Paths during Simple Pile Penetration (after Baligh 1985a)

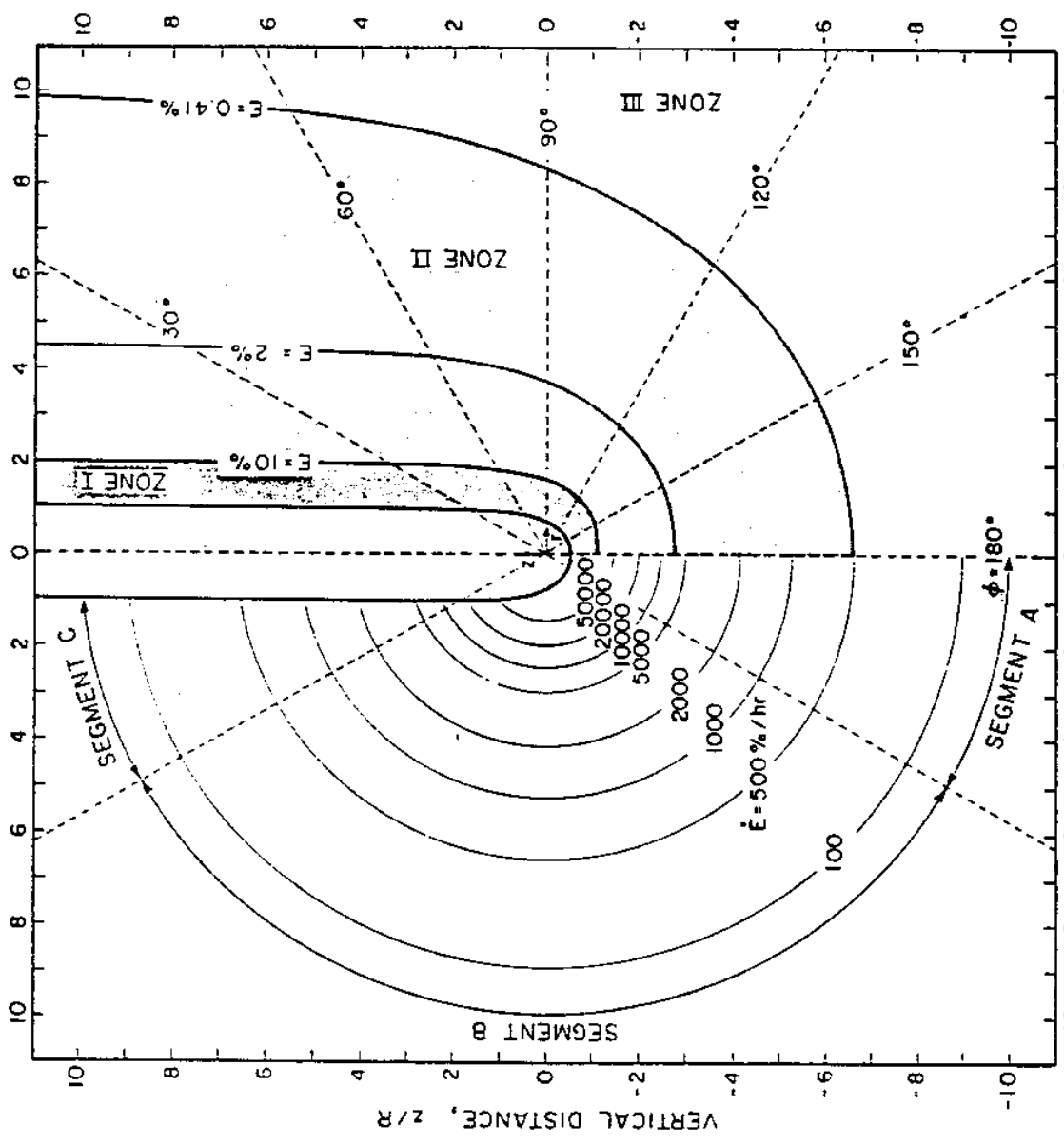

Fig. C.5 Shear Straining during Simple Pile Penetration (after Baligh 1985a)
(a) Strain Rates, $\dot{E}$, for R=1.78 cm (b) Strain Levels, E
and U=2 cm/sec

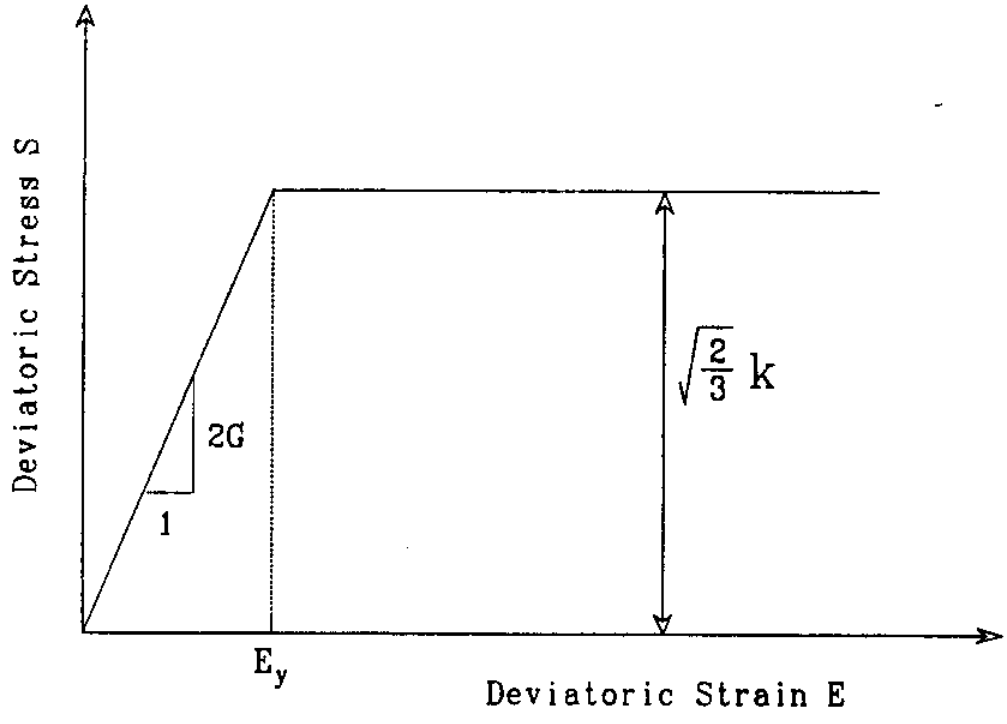

Fig. C.6 The Prandtl-Reuss Bilinear Model

Appendix C.2
Simple Pile Point Resistance in Clays - Energy Method
Baligh(1985a)

The absence of viscous effects in the P-R soil model and the neglect of inertial effects imply that the quasi-static penetration of the simple pile with velocity U requires work to be done at a steady rate of

$$\dot{W} = P_{sp} U \tag{34}$$

where P_{sp} is the estimated upper bound force required to push the simple pile. In view of the smoothness of the simple pile shaft, the power $\dot{W}$ is required to overcome tip resistance only. Neglecting the small negative work done in order to achieve simple upper bound solutions, this power can be divided into three components:

$$\dot{W} = \dot{W}_o + \dot{W}_p + \dot{W}_e \tag{35}$$

The first component, $\dot{W}_o$ is needed to overcome the initial stresses in the ground and is given by:

$$\dot{W}_o = \pi R^2 U \sigma_o \tag{36}$$

where σ_o is the assumed initial isotropic stress in the soil prior to penetration.

The second component, $\dot{W}_p$, is needed to cause plastic flow of the soil in the yielded zone surrounding the pile and the third, $\dot{W}_e$, is the rate of energy required by soil elasticity outside the plastic domain.

For the P-R model, the rate of plastic work dissipation is given by:

$$\dot{W}_p = \int_{V_p} d\dot{W}_p \tag{37}$$

where $d\dot{W}_p$ is the rate of energy dissipated per unit volume and V_p is the volume of the plastic zone. It can be shown that

$$d\dot{W}_p = \sqrt{6}\, k\dot{E}\, dV \tag{38}$$

where $\dot{E}$ is the octahedral strain rate. Using Eq. (16) and (34), Eq. (33) can be expressed as, in spherical coordinates,

$$\dot{W}_p = \frac{\sqrt{3}}{2} kR^2 U \int_{V_p} \frac{dV}{\rho^3} \tag{39}$$

The integral can be expressed as

$$\int_{V_p} = \int_{\theta=0}^{2\pi} \int_{\phi=0}^{\pi} \int_{\rho_1(\phi)}^{\rho_2(\phi)} \tag{40}$$

where $\rho_1(\phi)$ defines the simple pile geometry and $\rho_2(\phi)$ that of the elastic-plastic boundary. They are given by Eq. (11a) and (11b):

$$\rho_1(\phi) = \frac{r_1}{\sin\phi};\ r_1 = Rg_1(\phi);\ g_1(\phi) = \left(\frac{1+\cos\phi}{2}\right)^{\frac{1}{2}};\ \phi = \arctan\left(\frac{r}{z}\right) \tag{41a}$$

$$\rho_2(\phi) = \frac{r_2}{\sin\phi};\ r_2 = Rg_2(\phi);\ g_2(\phi) = \frac{1}{\sqrt{E_y}}\left[\frac{1+\cos\phi}{2}\left(1+\cos\phi+\sin^2\phi\right)\right]^{\frac{1}{4}} \tag{41b}$$

dV is given by:

$$dV = \rho^2 \sin\phi\, d\phi\, d\theta \tag{42}$$

Carrying out the integration in Eq. (39) using Eq. (40), (41) and (42):

$$\dot{W}_p = \pi R^2 k U \frac{\sqrt{3}}{4}\left[\log_e\left(\frac{3}{4}\right) - 2 - 4\log_e(E_y)\right] \qquad (43)$$

where $$E_y = \frac{k}{\sqrt{6G}} \qquad (44)$$

using Eq. (24) and (27).
The elastic strain energy density in the plastic zone doesn't vary during penetration and hence changes in the elastic strain energy density take place only in the elastic zone. The rate of elastic energy change is thus given by

$$\dot{W}_e = \int_{V_e} d\dot{W}_e \qquad (45)$$

where $d\dot{W}_e$ is the elastic strain energy density change rate and V_e is the elastic soil domain outside the elastic-plastic boundary. $d\dot{W}_e$ can be expressed as

$$d\dot{W}_e = 3S\frac{dE}{dt}dV \qquad (46)$$

$\int_{V_e}$ is given by:

$$\int_{V_e} = \int_{\theta=0}^{2\pi}\int_{\phi=0}^{\pi}\int_{\rho_2(\phi)}^{\infty} \qquad (47)$$

Performing the integration of Eq. (41) as in the plastic energy change rate case using Eq. (46), (47) and (42):

$$\dot{W}_e = \pi R^2 k U \qquad (48)$$

$\dot{W}_p$ and $\dot{W}_e$ can be expressed as

$$\dot{W}_p = \pi R^2 kU \cdot N_p \tag{49}$$

$$\dot{W}_e = \pi R^2 kU \cdot N_e \tag{50}$$

where

$$N_p = \frac{\sqrt{3}}{4}\left[\log_e\left(\frac{3}{4}\right) - 2 - 4\log_e(E_y)\right] \tag{51}$$

$$N_e = 1 \tag{52}$$

Let's define the simple pile point resistance q_{sp} and point resistance factor N_{sp}

$$q_{sp} = \frac{P}{\pi R^2} = N_{sp}k + \sigma_o \tag{53}$$

Substituting Eq. (49), (50) and (36) into Eq.(34), we have

$$N_{sp} = N_e + N_p = 1 + \frac{\sqrt{3}}{4}\left[\log_e\left(\frac{3}{4}\right) - 2 - 4\log_e(E_y)\right] \tag{54}$$

The expression for N_{sp} indicates the following features of this estimated upper bound for simple pile penetration resistance:

1. The pile radius R has no effect on the point resistance q_{sp} of the simple pile as defined by Eq. (53).
2. An increase in the initial isotropic stress σ_o causes an equal increase in q_{sp}. Practically, this describes the effect of depth below the ground on penetration resistance. The independence of N_{sp} from depth is intimately related to the assumed absence of frictional behavior of the soil during undrained penetration. For anisotropic yielding, $k=s_u(DSS)$ and $k=\frac{2}{\sqrt{3}}s_u(TC)$.
3. The point resistance q_{sp} is proportional to the shear strength parameter k.

4. The point resistance factor N_{sp} of the simple pile is principally controlled by the deviatoric yield strain E_y because it determines the size of the plastic zone and hence plastic work for penetration. In direct simple shear tests, $E_y=\frac{1}{\sqrt{6}}\gamma_y(DSS)$, where $\gamma_y(DSS)$ is the engineering strain at yield and in triaxial compression tests, $E_y=\frac{1}{\sqrt{2}}\varepsilon_y$, where ε_y is the axial strain at yield.

Appendix C.3

The Simple Pile Point Resistance in Clays - Centerline Analysis (Elghaib 1989)

1. Strains

Along the pile centerline, soil elements are subjected to triaxial compression mode of shearing, i.e.,

$$E_1 = \varepsilon_{zz} = \sqrt{2}E$$
$$E_2 = E_3 = 0 \qquad (55)$$

For the simple pile geometry, the axial strain ε_{zz} is given by

$$\varepsilon_{zz} = \ln\left(1 - \frac{R^2}{4z^2}\right) \qquad (56)$$

which for sufficiently large depth can be approximated by

$$\varepsilon_{zz} = \frac{R^2}{4z^2} \qquad (57)$$

The extent of the plastic zone is then

$$\frac{z_p}{R} = \sqrt{\frac{1}{4\varepsilon_y}} \qquad (58)$$

2. Shear Stresses

Deviatoric stresses also reduce to one component, $S_1=(\sigma_{zz}-\sigma_{rr})$. In the elastic zone

$$S_1 = \frac{3R^2}{4z^2}G;\ \frac{z}{R} < -\frac{z_p}{R} \qquad (59)$$

In the plastic zone, S_1 is directly related to the undrained shear strength measure k:

$$S_1 = \sqrt{3}k \tag{60}$$

3. Equilibrium

The octahedral stress σ is obtained from the equation of vertical equilibrium (Eq. (32)):

$$\frac{d\sigma}{dz} = -\frac{1}{\sqrt{3}}\left(\frac{2}{\sqrt{3}}\frac{dS_1}{dz} + \frac{S_3}{r}\right) \tag{61}$$

Along the centerline, $S_3=0$ and $r=0$; however $\frac{S_3}{r}$ is finite in magnitude. In the elastic zone, the following expression is valid

$$\frac{S_3}{r} = \frac{\sqrt{3}GR^2}{2z^3} \tag{62}$$

In the plastic zone, assuming a) no curvature along the centerline streamline and b) an elastic-plastic representation of soil behavior,

$$\frac{S_3}{r} \approx \frac{\sqrt{3}GR^2}{2z^3}\left(\frac{1}{1 - 2\dot{\lambda}\frac{G}{U}z}\right) \tag{63}$$

where $\dot{\lambda}$ is the plastic multiplier: $\dot{\lambda} = \frac{\sqrt{6}\dot{E}}{2k}$ (64)

Therefore,

$$\frac{S_3}{r} \approx \frac{3k}{z}\left[\frac{2}{2 + \left(\frac{z}{z_p}\right)^2}\right] \tag{65}$$

Using the expression of $\frac{S_3}{r}$ and the equilibrium equation, the change in mean stress can be found: for the bilinear model, $\Delta\sigma=0$ in the elastic zone ($z<-z_p$). Thus, the change in the octahedral stress at the elastic-plastic boundary, $\Delta\sigma_p(z=-z_p)=0$. In the plastic zone $\left(\frac{z}{R}>-\frac{z_p}{R}\right)$, the vertical equilibrium for the case of a perfectly plastic material is written

$$\frac{d\sigma}{dz}=-\frac{4\sqrt{3}}{2+\left(\frac{z}{z_p}\right)^2}\cdot\frac{k}{z} \qquad (66)$$

The integration of Eq.(66) from the plastic boundary to any element at a depth z ($-z_p/R<z/R<-0.5$) gives the expression for the mean stress $\Delta\sigma$ induced by undrained penetration in the plastic zone:

$$\Delta\sigma=\frac{\Delta\sigma_p}{k}+\sqrt{3}\ln\left[\frac{1}{3}+\frac{2}{3}\left(\frac{z_p}{z}\right)^2\right] \qquad (67)$$

4. Point Resistance

Based on centerline analysis, the point resistance q_c of the simple pile is given as

$$q_c=\sigma_{zz}\left(\frac{z}{R}=-0.5\right) \qquad (68)$$

In this case, the net point resistance Δq_c ($=q_c-\sigma_o$) is obtained from the stress state at the pile tip

$$\Delta q_c=\Delta\sigma+\frac{2}{\sqrt{3}}k \qquad (69)$$

The point resistance factor N_c for centerline analysis defined as

$$N_c = \frac{\Delta q_c}{s_u(TC)} \tag{70}$$

where $s_u(TC)$ is the undrained shear strength in a triaxial compression mode of shearing and $s_u(TC) = \frac{\sqrt{3}}{2}k$ is thus given by

$$N_c = 2\ln\left(\frac{1}{3} + \frac{2}{3}\frac{1}{\varepsilon_y}\right) + \frac{4}{3} \tag{71}$$

Appendix C.4
The Simple Pile Point Resistance in Sands - Centerline Analysis
(Elghaib 1989)

The soil is also described using a bilinear elastic-perfectly plastic model. Failure (yield) is described by an extended von Mises criterion:

$$S^2 - \frac{2}{3}\bar{k}^2\sigma'^2 = 0 \qquad (72)$$

where $\bar{k}$ is the friction ratio (the ratio of the shear to the normal effective stress) at failure. In triaxial space, this reduces to

$$S_1 = \sqrt{3}\bar{k}\sigma' \qquad (73)$$

The friction ratio $\bar{k}$ can be defined in terms of the friction angle ϕ' measured in triaxial compression by equating the von Mises criterion with the Mohr-Coulomb criterion:

$$\bar{k} = 2\sqrt{3}\frac{\sin\phi'}{3 - \sin\phi'} \qquad (74)$$

For the centerline solution of the simple pile, the octahedral stress can be obtained by integration of the equilibrium equation in the vertical direction (z-direction). Under all previous assumptions in the elastic zone ($z<-z_p$ or $\varepsilon<\varepsilon_y$), the mean effective stress remains constant and is equal to the initial isotropic effective stress σ_o'. In the plastic zone ($z_p>-z_p$ or $\varepsilon>\varepsilon_y$), the equilibrium reduces to the following first order differential equation

$$\frac{d\sigma_f'}{dz} = -\frac{4\sin\phi'}{3(1+\sin\phi')}\frac{6}{\left[2+\left(\frac{z}{z_p}\right)^2\right]z}\sigma_f' \qquad (75)$$

which can be integrated in closed form. The normalized octahedral stress induced in the plastic zone is thus given by

$$\frac{\sigma_f'}{\sigma_o'} = \left[\frac{1}{3} + \frac{2}{3}\left(\frac{z_p}{z}\right)^2\right]^{\chi} \qquad (76)$$

where $\chi = \frac{2\sin\phi'}{1+\sin\phi'}$. At the tip of the simple pile, z/R=-1/2, the mean effective stress is found to be:

$$\frac{\sigma_f'(tip)}{\sigma_o'} = \left[\frac{1}{3} + \frac{8}{3}\left(\frac{z_p}{R}\right)^2\right]^{\chi} \qquad (77)$$

The point resistance factor N_σ ($=q_c'/\sigma_o'=\sigma_{zz}'(tip)/\sigma_o'$) is then obtained from the Mohr circle of stress in the plastic zone:

$$\sigma_{zz}' = \frac{3(1+\sin\phi')}{(3-\sin\phi')}\sigma_f' ; z \geq -z_p \qquad (78)$$

Combining Eq. (77) and (78), the point resistance factor is obtained:

$$N_\sigma = \frac{3(1+\sin\phi')}{(3-\sin\phi')}\left[\frac{1}{3} + \frac{8}{3}\left(\frac{z_p}{R}\right)^2\right]^{\chi} \qquad (79)$$

Eq. (79) shows that N_σ is a function of the friction angle ϕ' and the extent of the plastic zone as expressed by $\frac{z_p}{R}$. The latter is directly related, in the case of an incompressible material, to the axial yield strain ε_y of the sand:

$$\frac{z_p}{R} = \sqrt{\frac{1}{4\varepsilon_y}} \qquad (80)$$

Hence, the simple pile solution for the point resistance factor (in an incompressible material) can be written as

$$N_\sigma = \frac{3(1+\sin\phi')}{(3-\sin\phi')}\left(\frac{1}{3}+\frac{2}{3}\frac{1}{\varepsilon_y}\right)^{\chi} \qquad (81)$$

APPENDIX D
REFERENCES

Baligh, M.M. (1975). Theory of Deep Site Static Cone Penetration Resistance, Research Report R75-56, Order No. 517, Department of Civil Engineering, M.I.T.

Baligh, M.M. (1985a). Fundamentals of Deep Penetration: I. Soil Shearing and Point Resistance, Research Report R85-9, Order No. 776, Department of Civil Engineering, M.I.T.

Baligh, M.M. (1985b). Fundamentals of Deep Penetration: II. Pore Pressures, Research Report R85-10, Order No. 777, Department of Civil Engineering, M.I.T.

Casagrande, A. and Shannon, W.L. (1949). "Strength of soils under dynamic loads", Transactions, ASCE, Vol. 114, pp. 755-772.

Dayal, U. and Allen, J.H. (1975). "The effect of penetration rate on the strength of remolded clay and sand samples", Can. Geotech. J., Vol. 12, pp. 336-348.

Desai, C.S. and Siriwardane, H.J. (1984). Constitutive Laws for Engineering Materials with Emphasis on Geologic Materials, Englewood Cliffs, New Jersey: Prentice-Hall.

Drucker, D.C. and Prager, W. (1952). "Soil mechanics and plastic analysis or limit design", Quarterly of Applied Mathematics, Vol. 10, No. 2, pp. 157-165.

Einstein, H.H. and Jeng, F.S. (1988). Propellant Embedded Anchors in Jointed Rock, Department of Civil Engineering, M.I.T, Report on Second Phase of Research for Naval Construction Center, Port Hueneme, CA.

Einstein, H.H., Whittle, A.J., Young, S., Baligh, M.M., and Li, V. (1987). Propellant Embedded Anchors in Jointed Rock, Department of Civil Engineering, M.I.T, Report on Research performed for Naval Construction Center, Port Hueneme, CA.

Elghaib, M.K. (1989). Prediction and Interpretation of Piezocone Data During Drained and Partially Drained Penetration, Ph. D. thesis, Department of Civil Engineering, M.I.T.

Hill, R. (1980). "Cavitation and the influence of headshape in attack of thick targets by non-deforming projectiles", J. Mech. Phys. Solids, Vol. 28, pp. 249-263.

Lacasse, S. (1979). Effect of Load Duration on Undrained Behavior of Clay and Sand - Literature Survey, Tech. Report 40007-1, Norwegian Geotechnical Institute.

Levadoux, J.N. and Baligh, M.M. (1980). Pore Pressure During Cone Penetration in Clays, Report No. MITSG 80-12, Index No. 80-312-Cim, Sea Grant College Program, M.I.T.

Murff, J.D. and Coyle, H.M. (1973). "Low velocity penetration of kaolin clay", Journal of Soil Mechanics and Foundation Engineering, ASCE, Vol. 99, No. SM5, pp. 375-389.

Sagaseta, C. (1987). "Analysis of undrained soil deformation due to ground loss", Geotechnique, Vol. 37, No. 3, pp. 301-320.

Schimming, B.B., Haas, H.J. and Saxe, H.C. (1966). "Study of dynamic and static failure envelopes", Journal of Soil Mechanics and Foundation Engineering, ASCE, Vol. 92, No. SM2, pp. 105-124.

Seed, H.B. and Lundgren, R. (1954). "Investigation of the effect of transient loading on the strength and deformation characteristics of saturated sands", Proc., ASTM, Vol. 54, pp. 1288-1306.

Teh, C.I. (1987). An Analytical Study of the Cone Penetration Test, Ph. D. thesis, Department of Civil Engineering, Hertfort College, University of Oxford.

Tomlinson, M.J. (1957). "The adhesion of piles driven in clay soils", Proc., 4th Internatl. Conf. Soil Mechanics Found. Engrg., Vol. 2, London, pp. 66-71.

Vesic, A.S. (1972). "Expansion of cavities in infinite soil mass", Journal of Soil Mechanics and Foundation Engineering, ASCE, Vol. 98, No. SM3, pp. 265-290.

Vesic, A.S. (1977). Design of Pile Foundations, Synthesis of Highway Practice 42, Transportation Research Board, National Research Council, Washington, D.C.

Wang, W.L. (1971). "Low velocity projectile penetration", Journal of Soil Mechanics and Foundation Engineering, ASCE, Vol. 97, No. SM12, pp. 1635-1655.

Whitman, R.V. and Healy, K.A. (1962). Shearing Resistance of Sands During Rapid Loadings, Research Report R62-113, Department of Civil Engineering, M.I.T.

Whittle, A.J. (1987). A Constitutive Model for Overconsolidated Clays with Application to the Cyclic Loading of Friction Piles, Ph. D. thesis, Department of Civil Engineering, M.I.T.